LA-8377-T

Thesis

1

Measurement of the Doubly Differential Cross Section for $\pi^-p \rightarrow \pi^+\pi^-n$ Near Threshold

LOS ALAMOS SCIENTIFIC LABORATORY
Post Office Box 1663 Los Alamos, New Mexico 87545

This thesis was accepted by the University of Wyoming, Laramie, Wyoming, Department of Physics and Astronomy, in partial fulfillment of the requirements for the degree of Doctor of Philosophy in Physics. It is the independent work of the author and has not been edited by the Technical Information staff.

This work was supported by the US Department of Energy, Office of High Energy and Nuclear Physics under Contract EY-76-5-02-2197-A002.

LA-8377-T
Thesis
UC-34c
Issued: May 1980

Measurement of the Doubly Differential Cross Section for $\pi^- p \rightarrow \pi^+ \pi^- n$ Near Threshold

John B. Walter*

*Present address: EG&G Idaho, Inc., Idaho Falls, ID 83415.

TABLE OF CONTENTS

LIST OF TABLES

LIST OF FIGURES

MEASUREMENT OF THE DOUBLY DIFFERENTIAL CROSS SECTION FOR $\pi^- p \rightarrow \pi^+ \pi^- n$ NEAR THRESHOLD

by

John B. Walter

ABSTRACT

The doubly differential cross sections for the π^+ from the reaction $\pi^- p \rightarrow \pi^+ \pi^- n$ were measured at about twenty points for each of five energies between 245 MeV and 356 MeV. The experiment was carried out at the Clinton P. Anderson Meson Physics Facility, where a double focussing magnetic spectrometer detected the π^+ mesons produced in a liquid hydrogen target. The measurements were normalized by comparison with $\pi^- p$ elastic scattering measured with the same apparatus. These are the first such measurements in this energy range, and have an accuracy between 4.7% and 39%. The integrated reaction cross section was determined at each energy with an accuracy of about 5%. These agree with but are an improvement over previous measurements in this energy range. Comparison of the extrapolated threshold value of the mean square modulus of the matrix element with the soft pion calculations favors the symmetry breaking mechanism of Weinberg (ξ=0). It also demonstrates the futility of attempting to determine the symmetry breaking parameter ξ from a single measurement of the integrated reaction cross section.

CHAPTER I

INTRODUCTION

The πN and $\pi\pi$ interactions are of interest to the understanding of the strong interaction. Soft pion theory addresses itself to these interactions. A number of processes are determined with but a single parameter, the pion decay constant f_π, permitting several evaluations of f_π. The lifetime of the charged pion, the Goldberger-Treiman relation, the πN s-wave scattering lengths, the $\pi\pi$ p-wave isovector scattering length all yield values for f_π consistent to within 8%.[1] This measure of success is striking in that the hypotheses involved are strictly valid only for soft pions; i.e., pions having vanishing four momenta. With this encouragement we examine soft pion theory further.

Single pion production in the reactions $\pi N \to \pi\pi N$ involves both the πN and $\pi\pi$ interactions. Considerations of parity and the Bose statistics of the pions require the threshold matrix elements for all the possible charge states to be calculable from two matrix elements. Assuming the current algebra hypothesis and the partial conservation of the axial vector current (PCAC), soft pion calculations determine both matrix elements with a single additional parameter ξ.[2] This parameter distinguishes amongst the symmetry breaking mechanisms proposed to provide nonconservation of the axial vector current. Table 1 presents the threshold matrix elements predicted for the five charge states tractable to experiment, and the predicted threshold behavior of the cross section. Knowledge of the threshold matrix element for the first two and

Table I. Threshold matrix elements in soft pion theory.

1. $\pi^- p \to \pi^+ \pi^- n$: $M = \alpha(-1.36 + 0.60\ \xi) = -0.15\ \alpha - 3.5(2a_0 + a_2)$

2. $\pi^- p \to \pi^0 \pi^0 n$: $M = \alpha(\ 2.11 - 0.30\ \xi) = \ 0.30\ \alpha + 6.9(a_0 - a_2)$

3. $\pi^+ p \to \pi^+ \pi^+ n$: $M = \alpha(\ 1.51 + 0.60\ \xi) = \ 0.30\ \alpha - 20.8\ a_2$

4&5. $\pi^\pm p \to \pi^\pm \pi^0 p$: $M = \alpha(\ 0.53 + 0.21\ \xi) = \ 0.11\ \alpha - 7.1\ a_2$

$$\sigma_0 = (\lambda\!\!\!^{-2}/4)(G^2/4\pi)^3 (g_v/g_a)^4 (m_\pi^2/M_N^4)(Q/S) \int_0^{T''_{max}} (T'_{max} - T'_{min})\, dT''$$

$$\sigma_{production} = \varepsilon\ |M|^2\ \sigma_0$$

$$a_0 = \frac{14 - 5\xi}{64\pi} (m_\pi/f_\pi)^2$$

$$a_2 = -\frac{\xi + 2}{32\pi} (m_\pi/f_\pi)^2$$

$$\alpha = (86.9\ \text{MeV}/f_\pi)^2$$

ξ = symmetry breaking parameter

ε = 1, if charges of final pions differ
ε = ½, if charges of final pions are alike

$\lambda\!\!\!^{-}$ = Compton wavelength of charged pion ÷ 2π

$(G^2/4\pi) = 14.6$

$(g_a/g_v) = 1.253$

m_π = pion mass

M_N = nucleon mass

Q = incident momentum in the center for momentum

S = total energy in the center of momentum

T', T" = kinetic energies in the center of momentum of any two final particles

a_0, a_2 = S-wave π-π scattering lengths with isospins 0 and 2

one of the last three would critically test this application of the theory. However, measurements of the small cross sections near threshold have been of limited accuracy for the first reaction and totally lacking for the last four. Even for the first reaction, the required extrapolation of the matrix element to threshold has been less than convincing. None the less, experiment and calculation have agreed roughly for ξ between $\pm$ 1.

This work was planned as a study of the first reaction, $\pi^-p \rightarrow \pi^+\pi^-n$, with the improved precision possible with the intense pion beams available at the Clinton P. Anderson Meson Physics Facility (LAMPF). A double focusing, 180° vertical bend, magnetic spectrometer measured the doubly differential cross sections for π^+ mesons produced in a liquid hydrogen target. A ladder of nineteen surface barrier detectors spanning the focal plane covered a $\Delta p/p$ of 9.5%, providing momentum resolution by virtue of spatial discrimination. The target flask, particle trajectory in the spectrometer, and the array of detectors were in a common vacuum to minimize loss of energy and multiple scattering of low energy particles. Three plastic scintillation detectors, providing a trigger, and a threshold Cerenkov detector, providing electron discrimination, completed the detection system. The entire assembly, including the target and cryostat, could be rotated as a unit about the vertical axis of the cylindrical target to angles between 32° and 130°. The spectrometer could select charged particles with momenta up to 325 MeV/c, and detect π mesons down to 70 MeV/c. The flux of incident π mesons was measured by both an ion chamber and a scattering monitor. The complete apparatus was calibrated as a whole by detecting the π meson elastically scattered

from the hydrogen, and adjusting the overall normalization of the measurement of the πp elastic cross sections.

The study included five incident energies, 254 MeV, 279 MeV, 292 MeV, 330 MeV and 356 MeV, with the express purpose of extrapolation to the 172 MeV threshold and comparison to soft pion calculations. The doubly differential cross section, $(\frac{d^2\sigma}{d\Omega dp})_{LAB}$, of the produced π^+ meson was measured at about twenty points for each energy. In each case these measurements were distributed more or less uniformly in the center of momentum frame over the accessible portion of (T, cosθ) space. At each point the square modulus of the matrix element, averaged over the unobserved variables, was determined from the measurement. For each energy a plausible function of T and cosθ was fitted to the collection of square moduli corrected for Coulomb attraction in the final state. This function, weighted by the density of phase space, was averaged over T and cosθ to provide the corrected average square modulus of the matrix element. The function was also multiplied by the Coulomb factor and the density of phase space and integrated over T and cosθ to determine the integrated reaction cross section. The threshold value of the mean corrected square modulus was extrapolated from these five values and a more recent value[3] at 230 MeV and compared to the soft pion calculation to determine the symmetry breaking parameter ξ. The large variation with incident energy apparent in the mean corrected square modulus even at 230 MeV demonstrated the necessity of extrapolating to threshold from a series of measurements. No single measurement which validly represented the soft pion limit would be practical.

The equipment and experimental procedure are detailed in Chapter II,

while Chapter III describes the accompanying calibrations. Chapter IV delineates the interpolation of the differential cross section for πp elastic scattering from the best measurements available. Chapter V presents the analysis of the measurements for $\pi^- p \to \pi^+ \pi^- n$.

CHAPTER II

EXPERIMENTAL DESIGN AND EQUIPMENT

Introduction

This experiment measured the doubly differential cross section for the reaction $\pi^- p \rightarrow \pi^+ \pi^- n$ by detecting only the outgoing π^+ meson. The plan view of the experiment is shown in Fig. 1. A beam of π^- mesons was incident upon a liquid hydrogen target. A magnetic spectrometer passed π^+ mesons of the selected angle and momentum, focusing them onto a ladder of surface barrier detectors. The π^+ mesons continued through a trigger telescope of three plastic scintillation detectors, and a threshold Cerenkov detector. A scattering monitor downstream and an ion chamber upstream of the liquid hydrogen target measured the flux of π^- mesons in the beam. The horizontal and vertical positions of the π^- beam were monitored by a pair of multiwire proportional chambers.

The Pion Beam

The experiment was carried out at the Clinton P. Anderson Meson Physics Facility (LAMPF) on the west branch of the secondary beam channel "Pion and Particle Physics" (P^3 - west). This channel could provide positive or negative π mesons over a broad range of momenta, 190 MeV/c < p < 730 MeV/c, and a reasonable range of momentum bite, $0.0025 < \Delta p/p < 0.10$.[4] It had been designed to be both isochronous and achromatic, which means that the channel preserves the time structure of the beam and that the position and angle of a π meson arriving at the target are independent of the particle momentum. The channel was tuned to deliver

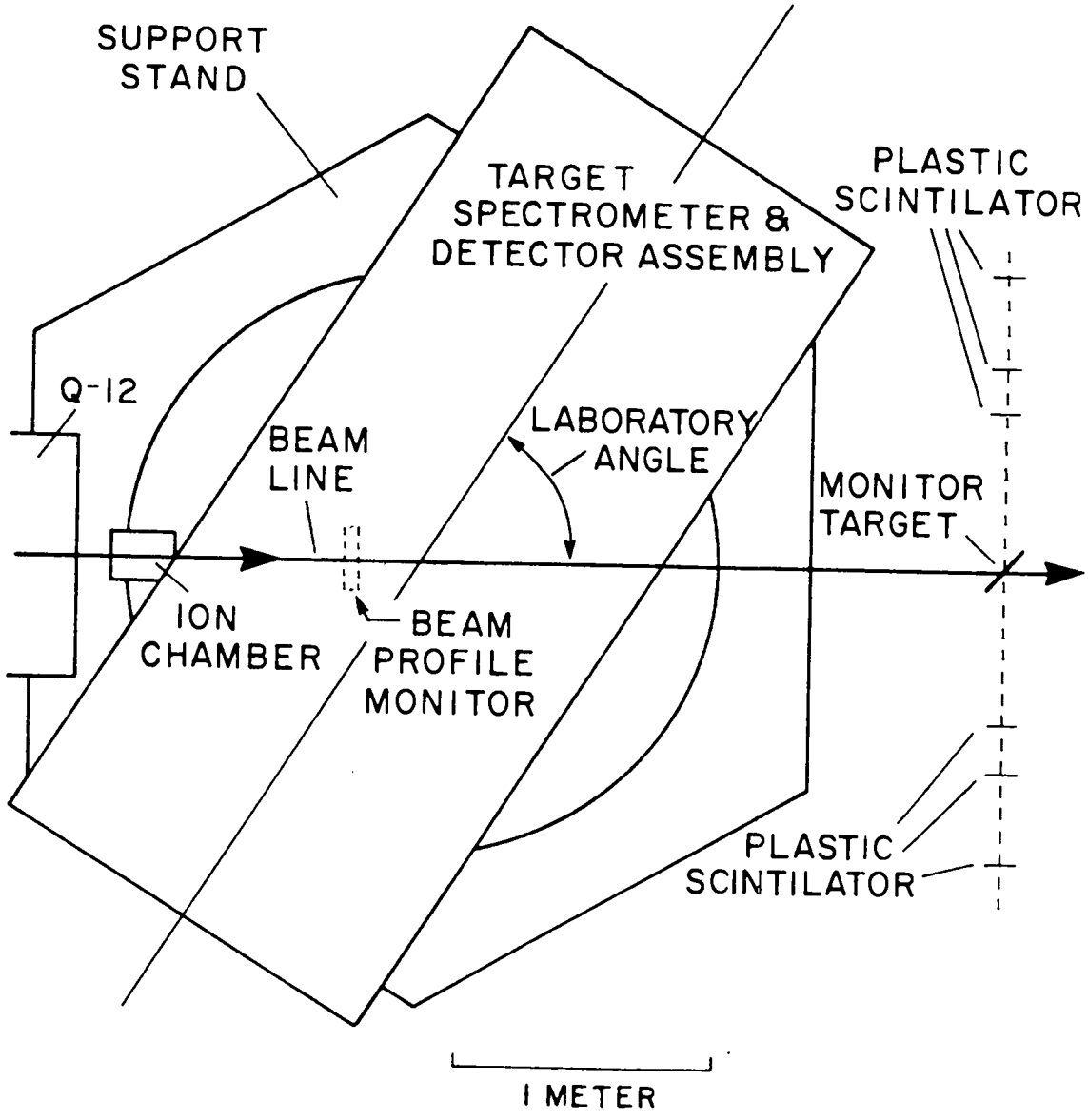

Fig. 1. Plan view of experiment. Q-12 is the last quadrapole magnet of P^3-west.

the desired beam primarily from the results of a computer simulation,[5] but some final steering adjustments were made on the basis of the pair of multiwire proportional chambers just upstream of the liquid hydrogen target, indicated as beam profile monitor in Fig. 1.

The momentum of the beam was one of the inputs to the computer simulation of the channel, and so was presumably known. The kinematics of π^-p elastic scattering reliably yielded the beam momentum, with a result about 2% lower than the expected value. This deviation and the final beam adjustments both now appear to be due to an error in the conversion from shunt voltage to magnetic field strength for the first bending magnet of P^3, which determines the momentum. When P^3 was tuned according to the simulation, the profile monitor, described below, showed the beam to be off the beam line and to have a washed out profile. The last two of the three P^3 bending magnets were alternately twiddled to optimize the profile and bring the beam back on beam line. The beam was brought to a waist at the hydrogen target with a spot size of 1.5 cm vertical by 1.2 cm horizontal, full width at half maximum (FWHM), as measured by the profile monitor.

The profile monitor was developed at LAMPF and has been described by Krausse and Gram.[6] It consisted of a pair of multiwire proportional chambers which detected the beam profile in both the horizontal and vertical directions. The two planes were separated by 1 cm, and each contained 64 wires with 0.2 cm spacing between wires. The chambers were filled with a mixture of 80% argon and 20% carbon, and were operated at about -2.4 kV. The current from each wire was converted to a voltage, the peak voltage detected and held long enough for the multiplexer to complete the scan of all 64 channels. The output from each chamber was displayed on an oscil-

loscope, providing a histogram of the voltage for each wire. The multiplexer scan and the oscilloscope were triggered by a beam gate logic pulse which indicated the temporal structure of the beam.

Liquid Hydrogen Target

The target flask, shown in Fig. 2, was a 2.54 cm diameter cylinder of 50 μm mylar. It was oriented coaxially with the vertical axis of rotation of the spectrometer.[7] The two ends of the cylinder were epoxied to stainless steel tubing which connected the flask to the Cryodyne Model 1022 refrigerator and the reservoir of liquid hydrogen located above the flask as shown in Fig. 3. The refrigerator, reservoir and flask were enclosed in the vacuum system of the spectrometer and rotated with it. The hydrogen system was insulated from radiative heat transfer by super insulation which can be seen on the refrigerator, part of the reservoir, and the target flask in Fig. 3. The gaseous hydrogen which boiled from the liquid hydrogen in the target was returned to the refrigerator through the tube at the top of the flask and a helium operated valve (in series with the tube) when the valve was open. When the valve was closed, gaseous hydrogen collected beneath the valve, forcing the liquid hydrogen from the flask into the reservoir through the tube at the bottom of the flask. The valve provided a means of emptying and filling the target. The 1 kΩ composition resistors shown in Fig. 2 at the top and bottom of the flask served as level sensors which were read remotely. The slit in the super insulation on either side of the flask in Fig. 3 permitted a visual check on the presence of liquid hydrogen in the flask.

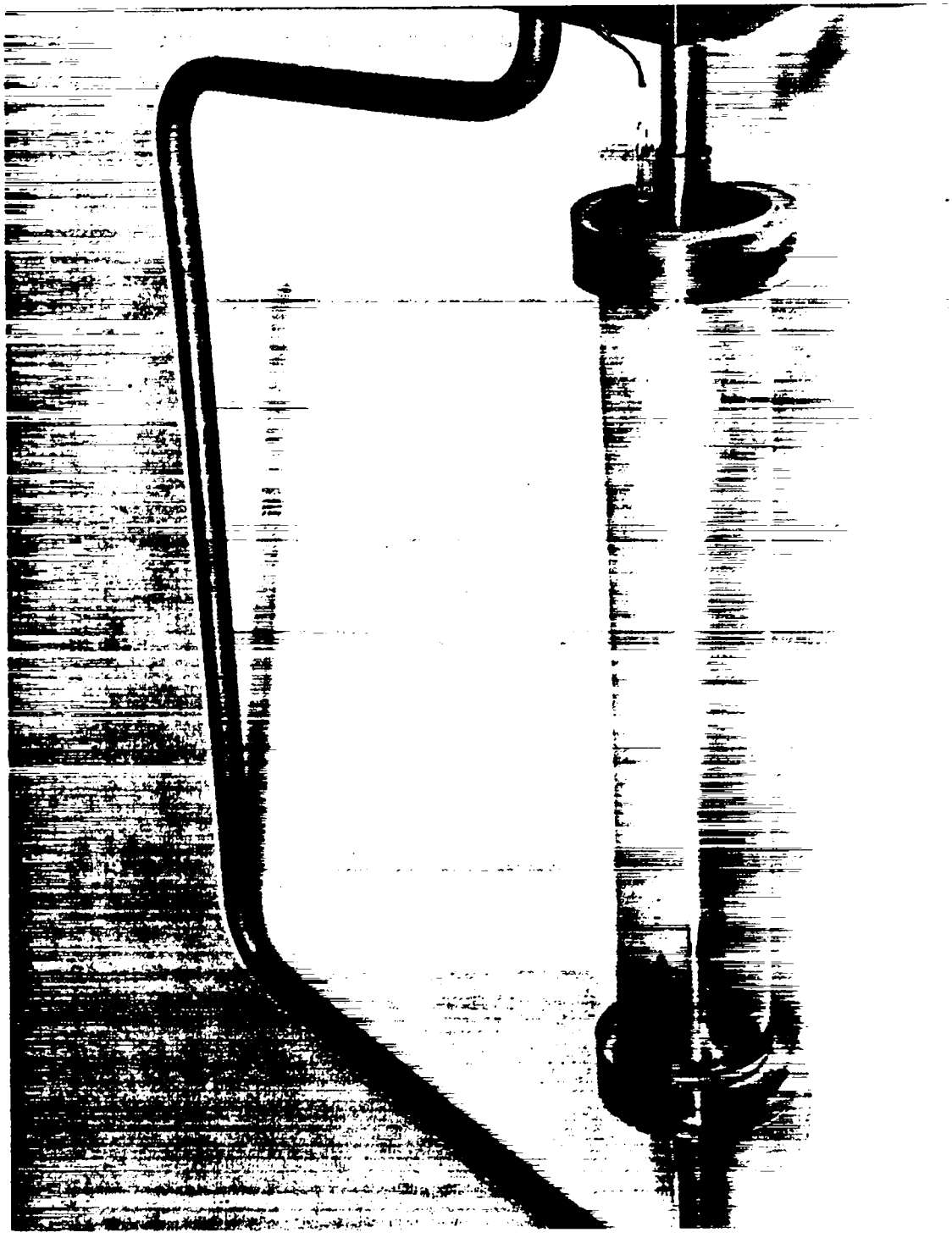

Fig. 2. Liquid hydrogen target flask.

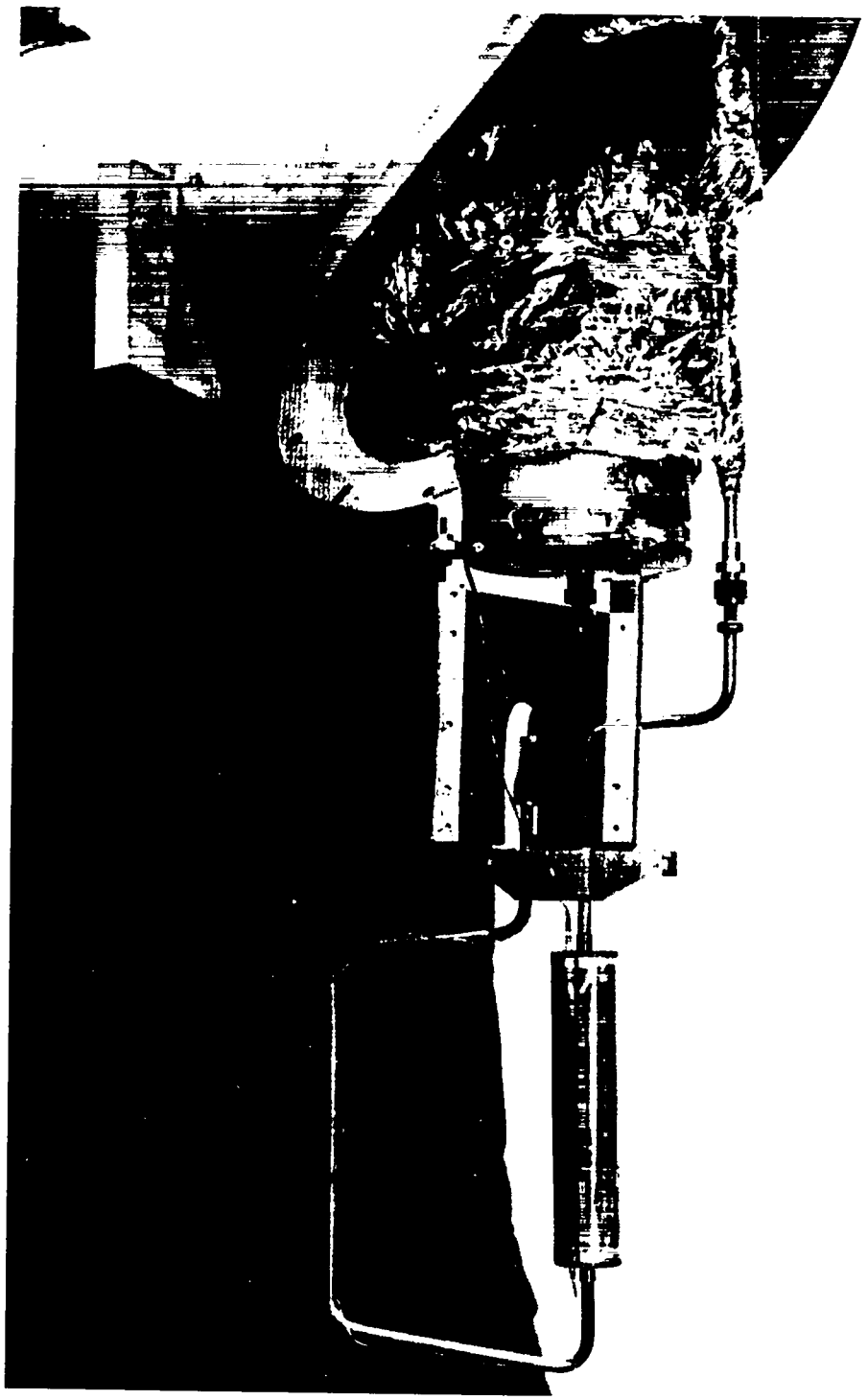

Fig. 3. Target flask with reservoir and refrigerator.

Spectrometer

The 180°, vertical bend double focusing, magnetic spectrometer and the detector system are shown in profile in Figs. 4 and 5. Properties of the spectrometer are summarized in Table II. The design and early history of the spectrometer are related by Oyer.[8] Particles which entered the spectrometer with the selected charge and momentum were bent vertically through 180° by the two 90° bending magnets, and focused onto a ladder of nineteen surface barrier detectors which covered a $\Delta p/p$ of 9.5%. The target, the path through the magnets, and the ladder of detectors were enclosed in a continuous vacuum to minimize loss of energy and multiple scattering of the particles prior to reaching the surface barrier detectors. After passing through the ladder, the particles continued outside the vacuum to three plastic scintillation detectors and a threshold Cerenkov detector.

The entire assembly of the cryostat, liquid hydrogen target, and the spectrometer was mounted on a Navy Surplus 5 inch gun mount, and was conveniently rotated about the vertical axis of the cylindrical target. The vertical configuration of the spectrometer placed the detector system and the spectrometer out of the beam, permitting the assembly to be rotated to laboratory angles between 32° and 130°. These restrictions resulted principally from the bulk of the assembly and its proximity to the final quadrapole magnet of P^3 - west, denoted by Q-12 in Fig. 1.

The momentum was determined by the uniform magnetic fields of the bending magnets. These fields were related to the shunt voltage, the voltage drop across a metal alloy resistor in series with the two mag-

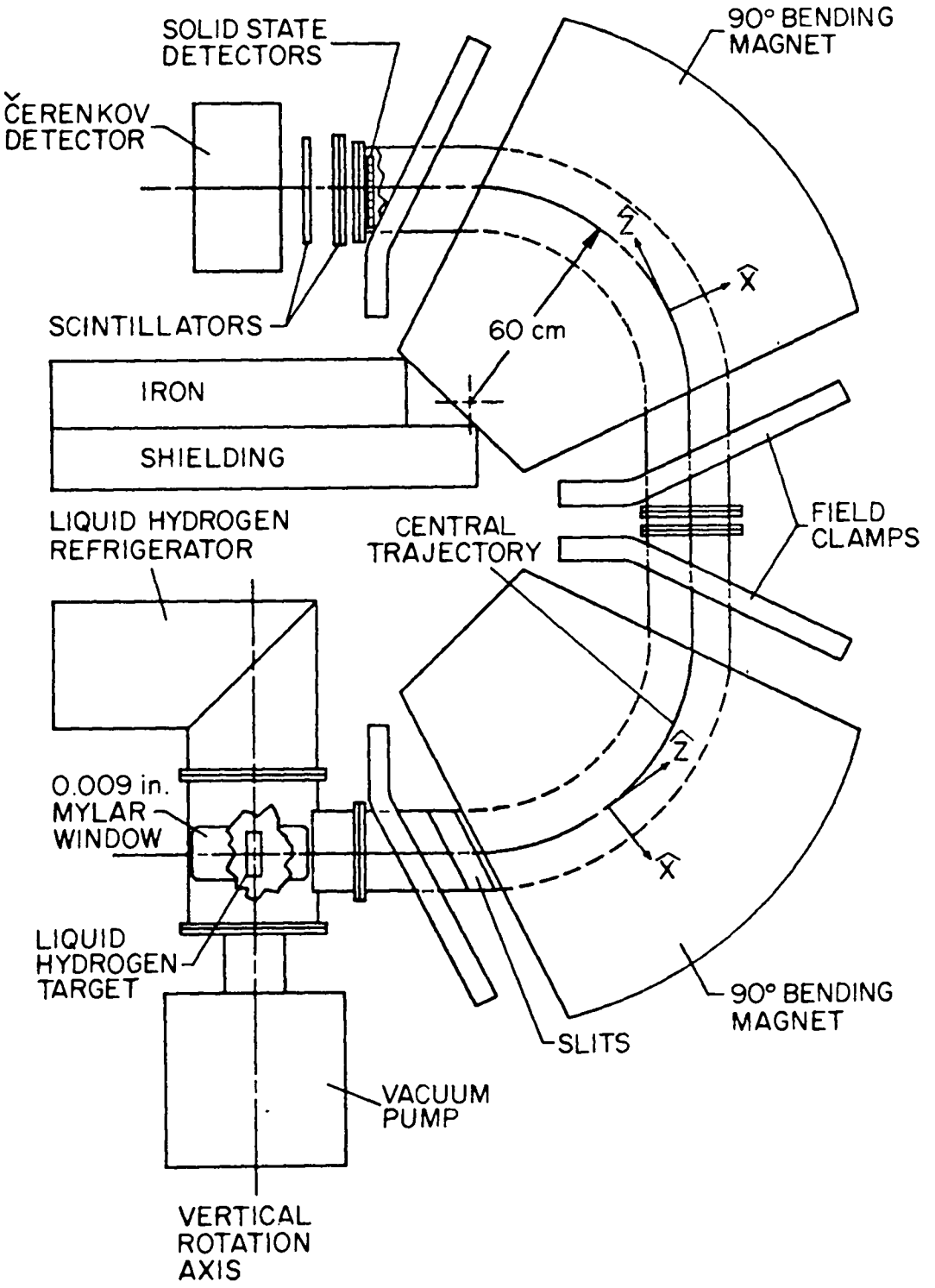

Fig. 4. Profile of spectrometer and detector system.

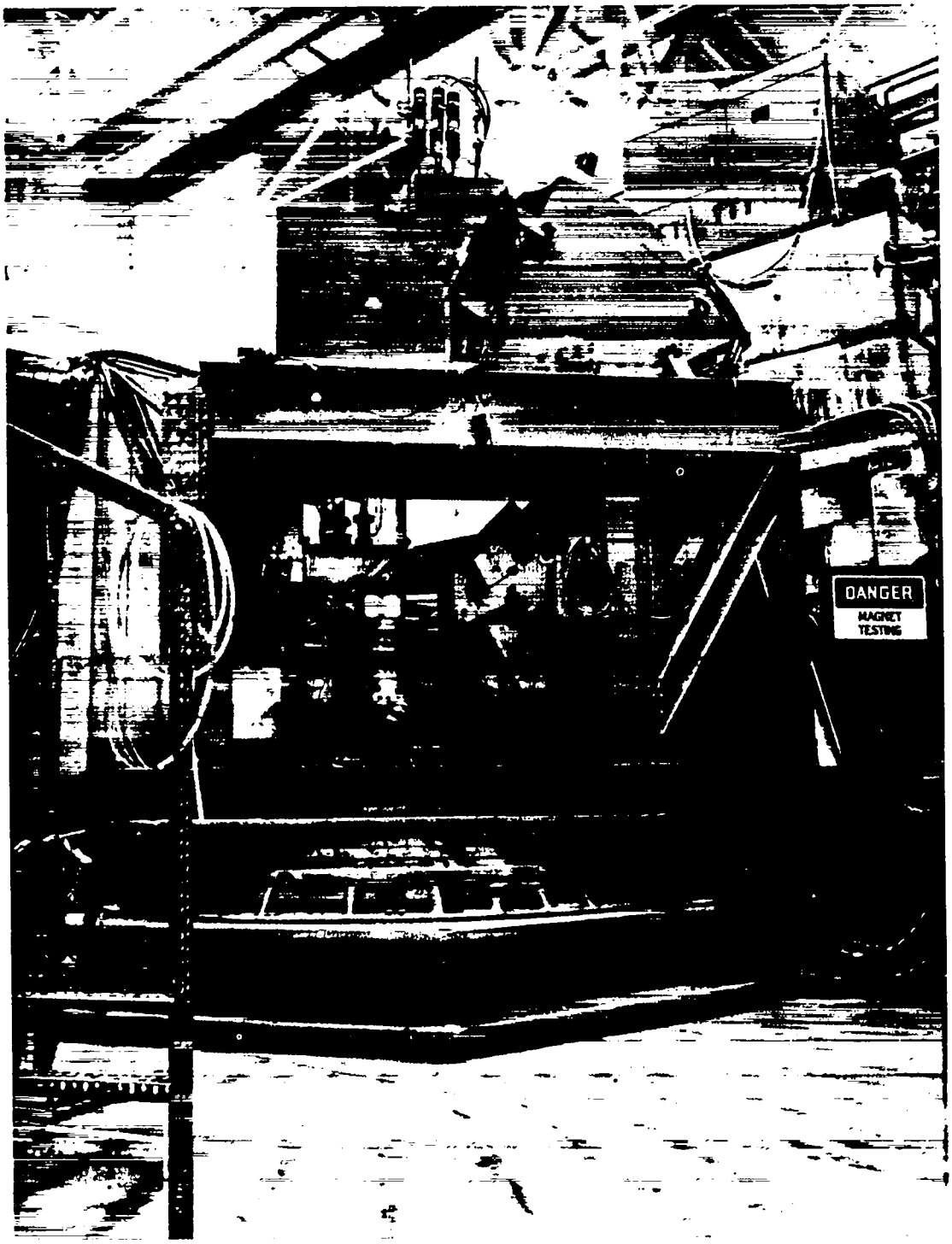

Fig. 5. Profile of spectrometer.

Table II. Spectrometer properties.

Conversion from field strength to central momentum, a = 18.119 (MeV/c)/kG	
dispersion	δ = 0.4351 ± 0.0004 %/cm
	= 0.4895 ± 0.0005 %/channel
magnification	= -0.96
solid angle acceptance	= 15 msr
scattering angle acceptance	= 2.5°
upper momentum limit	= 325 MeV/c

nets, and were found to be well represented by functions of the form[8]

$$H(x) = A + B\sigma(1 + \exp(-\mu/\sigma)) \ln\{(1 + \exp(\mu/\sigma))/(1 + \exp((\mu-x)/\sigma))\}$$

where x is the shunt voltage. Table III displays the parameter values used for each magnet. The slope of this function, dH/dx, is a Fermi function with the shunt voltage analogous to the energy, the parameter μ analogous to the chemical potential, and the parameter σ analogous to kT. The field is thus represented as nearly linear for small shunt voltage and rolling off to a constant saturation level for large shunt voltage. The nominal spectrometer momentum was

$$p = \tfrac{1}{2}\{H_1(x) + H_2(x)\} \, a \, q$$

where H_1 and H_2 were the fields in the two magnets, x the shunt voltage, a was a conversion factor determined experimentally as described in Chapter III, and q was the particle charge in units of the electron charge. A particle entering the spectrometer from the center of the target, having the nominal spectrometer momentum and the selected charge sign, followed a trajectory which passed through the center of the focal plane. A particle with a momentum differing by Δp followed a trajectory which was displaced at the focal plane by a distance equal to the product of $\Delta p/p$ with δ the dispersion of the spectrometer. This displacement was measured by the ladder of surface barrier detectors. Each of these detectors in coincidence with the three scintillation detectors defined a detection channel. Thus there were nineteen detection channels, each corresponding to a different range of displacement from the center of the focal plane.

The solid angle acceptance for a detection channel was in each case

Table III. Parameter values for spectrometer excitation function.

	A (Gauss)	B (Gauss/mV)	μ (mV)	σ (mV)
Magnet 1	12.55 ± 8.98	278.9 ± 0.42	74.02 ± 1.13	7.436 ± 0.54
Magnet 2	19.65 ± 3.45	277.8 ± 0.15	72.34 ± 0.39	6.484 ± 0.19

limited by the walls of the vacuum chamber and thus varied from channel to channel. The particle transport model of the spectrometer predicted that the solid angle acceptance for the extreme channels would be 40% less than that for the central channel. This calculation could not include an unknown variation in the sensitive areas of the surface barrier detectors and other possible effects, and it was thus essential to measure the variation in the solid angle acceptance, referred to as efficiency. This determination, described in Chapter III, provided the results in Table IV after the efficiencies were normalized to 1.0 for the tenth or central detector. The efficiencies are also shown in Fig. 6, where the statistical uncertainties are about the size of the symbol.

Detectors and Detection System

The detectors used in this experiment (see Fig. 4) consisted of surface barrier detectors, scintillation detectors and a Cerenkov detector. The nineteen surface barrier detectors were distributed across the focal plane, providing momentum resolution. They also aided in particle identification for momenta below 90 MeV/c through dE/dx information. A coincidence among the three scintillation detectors and at least one of the surface barrier detectors signaled the computer which then processed the event. The Cerenkov detector identified e^+ which had been transported by the spectrometer. This section describes these devices and their accompanying electronics.

The surface barrier detectors were of the silicon variety, each nominally 1 cm x 3 cm x 400 μm. A previous study showed the system to have a large depth of focus.[8] Hence the detectors were staggered,

Table IV. Detection channel efficiencies.

Channel	η	$\Delta\eta$ (%)
1	0.5786	0.78
2	0.6701	0.75
3	0.7626	0.73
4	0.8607	0.70
5	0.9039	1.00
6	0.9631	0.69
7	1.0103	0.69
8	0.9787	0.71
9	0.9923	0.70
10	1.0000	0.70
11	0.9509	0.72
12	0.9573	0.72
13	0.9618	1.04
14	0.9494	0.71
15	0.8633	0.74
16	0.8031	0.76
17	0.7379	0.79
18	0.6730	0.84
19	0.5900	1.00

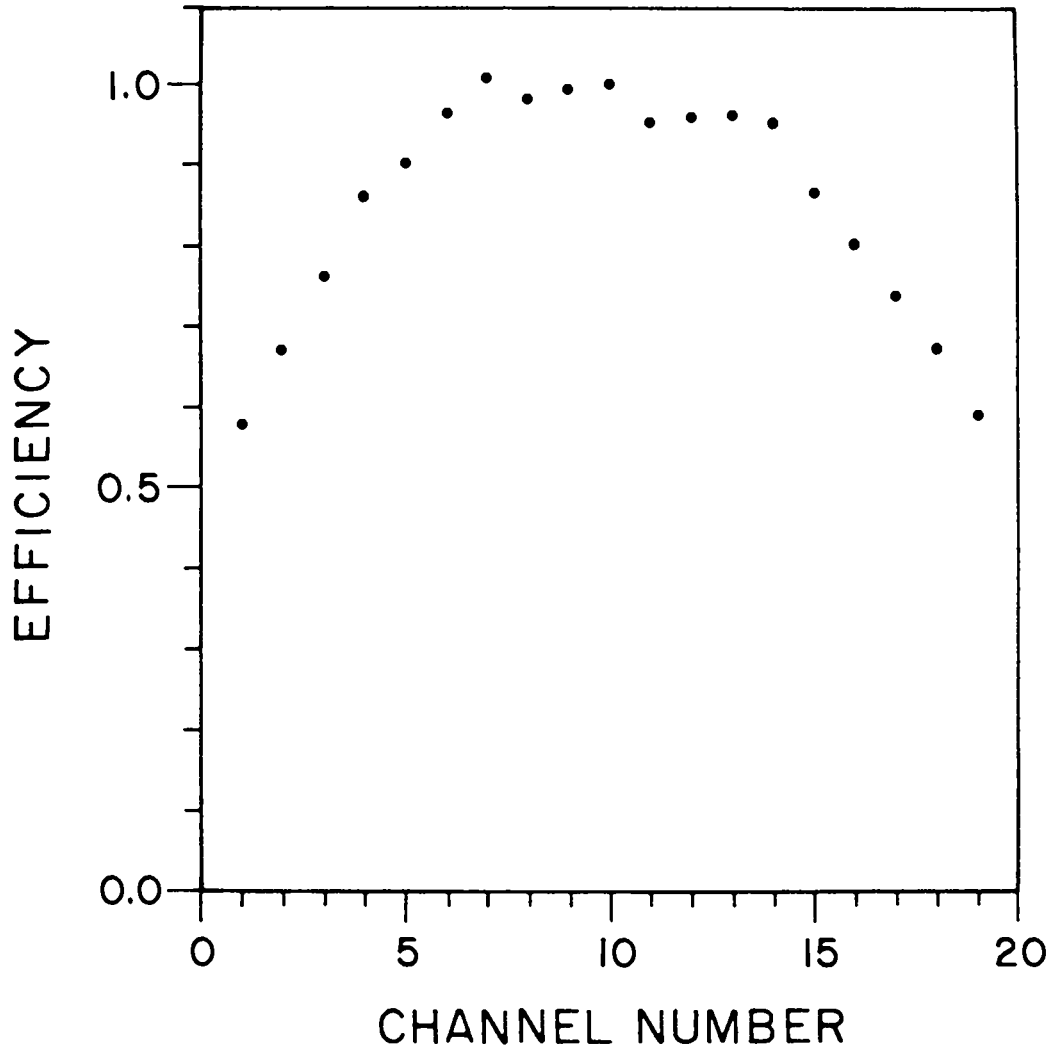

Fig. 6. Detection channel efficiencies. The errors are about the size of the dots.

positioned alternately 0.2 cm on either side of the focal plane, to allow them to be located on 1.125 cm centers as shown in Fig. 7. The devices were distributed along the dispersion direction and thus provided momentum resolution.

Each of the silicon detectors was reverse biased with sufficient voltage to extend the depletion layer to the full thickness of the device. Thus the entire volume of the detector was sensitive to charged particles, providing an optimum electrical efficiency. The signal from the detector was a current pulse with a total charge proportional to the energy deposited by the particle which had crossed the detector. A solid state preamplifier, located near the detector to minimize the capacitance of the connecting cable, integrated the current and produced an exponentially decaying voltage pulse with a time constant of 7 μs and an amplitude proportional to the total charge of the initial pulse. The output drove a shaping amplifier which amplified, integrated again to further reduce the presence of the high frequency noise inherent in solid state detectors, and differentiated twice, all with a 250 ns time constant. The resulting bipolar pulse, with an amplitude proportional to the original energy deposition, was finally processed by a single channel analyzer which produced a 20 ns negative logic pulse provided the amplitude was between an upper and lower limit. The lower limit was set to accept the level of minimum ionizing particles except for momenta below 90 MeV/c, for which the Pb absorber just before the third scintillation detector had to be removed to detect the π^+ mesons. In these cases the lower limit was raised to eliminate a portion of the soft $e^{\pm}$ background. The upper limit was set at the maximum of the de-

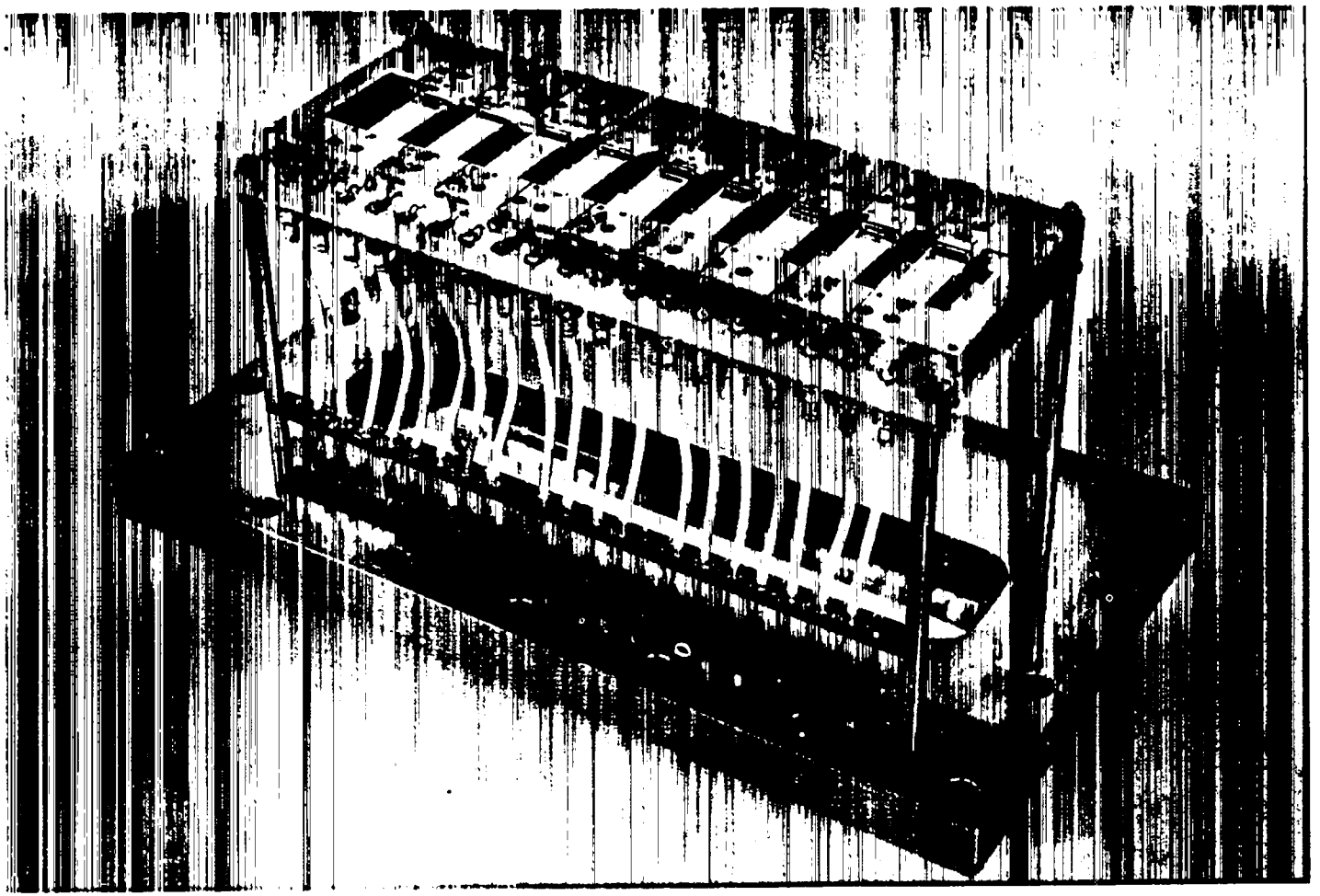

Fig. 7. Ladder of surface barrier detectors.

vice (protons transported by spectrometer had too little energy to trigger the last scintillation detector). The logic pulse was delivered to an input on one of two CAMAC registers which were read by the computer.

The plastic scintillation detectors each measured 26.7 x 5.7 x 0.35 cm and were located 13, 14 and 23 cm behind the focal plane. A triple coincidence among these detectors gated the surface barrier detectors and the Cerenkov detector. A portion of the background events which were not associated with the spectrometer was thus elminated. A 0.8 mm Pb absorber was placed just before the third detector for momenta above 90 MeV/c to further reduce the soft $e^{\pm}$ background.

Each plastic scintillation detector was viewed by an EMI 9815B photomultiplier tube through a Lucite light pipe. The tubes were biased by LAMPF standard bases, and equipped with the accompanying MUMETAL and iron magnetic shields. Each detector drove a discriminator which produced a 20 ns logic pulse whenever the detector pulse height exceeded a minimum level. These logic pulses were futher processed by the trigger and dead time system.

The Cerenkov detector measured radiation from FC-88 a liquid fluorocarbon marketed by Minnesota Mining and Manufacturing Company. The fluid was contained in a 30 cm high, 12.7 cm diameter, 1.6 mm wall aluminum cylinder which was lined with a 0.4 mm sheet of ALZAK to provide high reflectivity. It was viewed by two Amperex 58 DVP photomultiplier tubes, one on either end of the cylinder. The signals from the photomultiplers were summed in a passive circuit and fed to a discriminator, which produced a logic pulse whenever the combined pulse height exceeded a minimum value. The logic pulse was delayed 110 ns to match the gate pulse and delivered to a CAMAC register.

The trigger and dead time logic is displayed in Fig. 8. A three-fold coincidence among the logic pulses from the plastic scintillation detectors S_1, S_2 and S_3 produced a gate pulse for the Cerenkov detector. This pulse was also delayed an additional 580 ns by a gate and delay generator and stretched to a width of 200 ns by a discriminator and used to gate the signals from the surface barrier detectors. The width was necessary to allow for jitter in the 700 ns processing time for the pulses from the surface barrier detectors. Pulses from the surface barrier detectors arriving at the CAMAC registers during the gate pulse were registered. These registers had a summing output which provided a current pulse with an amplitude proportional to the number of inputs which had registered a signal. This signal thus indicated the number of surface barrier detectors producing a pulse in coincidence with the plastic scintillation detectors. The computer was signaled to process the event if at least one of the inputs had received a pulse. The computer subsequently read and cleared the CAMAC registers for the surface barrier detectors and the Cerenkov detector and added the event to the appropriate histogram. The dead time pulse ensured that no further gate pulse could reach the registers while the event was being processed. The dead time pulse consisted of two parts. A 1 μs pulse τ_1 was put out by a discriminator on the falling edge of $\overline{S_1 S_2 S_3}$, which allowed sufficient time for the CAMAC registers to receive any pulses from the surface barriers detectors. A pulse from the summing output of the CAMAC registers initiated an extention pulse τ_2 from a gate generator in addition to notifying the computer. This pulse was terminated by a stop pulse from the computer once it had finished pro-

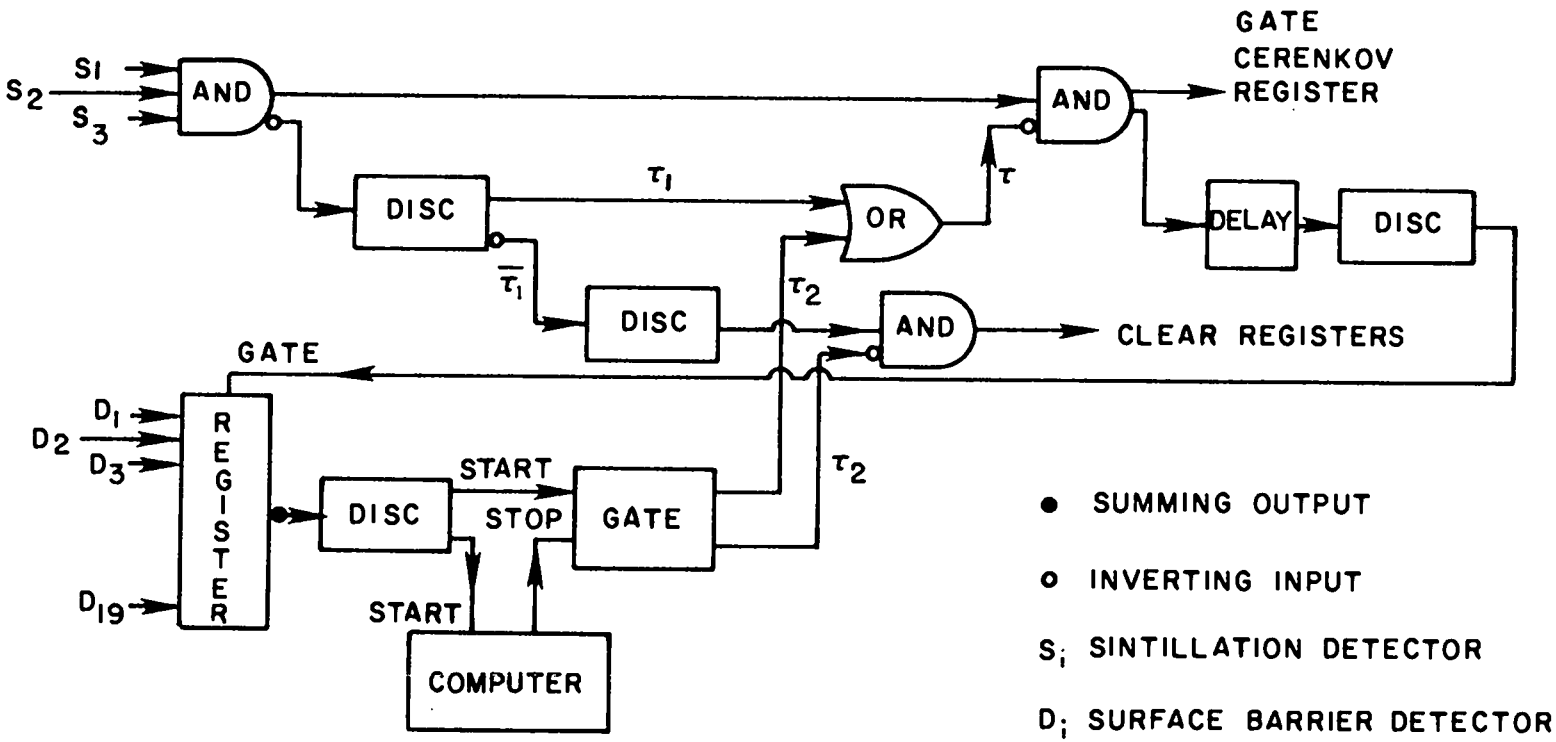

Fig. 8. Trigger and deadtime logic.

cessing the event. In the instance that no coincident pulse from the surface barrier detectors was registered, the register for the Cerenkov detector might still have received a pulse and had to be cleared. A discriminator put out a clear pulse on the falling edge of τ_1. This pulse was vetoed by τ_2 if it was present, but otherwise cleared the Cerenkov register and the registers for the surface barrier detectors as well. An estimate of the number of events lost during dead time was possible since various quantities which were scaled, such as $S_1S_2S_3$, were scaled with and without a dead time inhibit as discussed below.

Beam Flux Monitors

The incident flux of pions was monitored by a scattering monitor and an ion chamber as shown in Fig. 1. The scattering monitor, located downstream of the liquid hydrogen target, was the principal monitor since it was not subject to the vagaries of the ambient temperature and pressure as was the the ion chamber. However, the spectrometer intercepted a portion of the beam for measurements forward of about 40° in the laboratory, and the ion chamber provided the necessary connection with temporally nearby meàsurements.

The scattering monitor consisted of a polyethylene target viewed by two counter telescopes as shown in Fig. 1. The polyethylene target measured 23 x 15 x 1.3 cm and was oriented in a vertical plane which cut the beam line and the line of the two telescopes at 45° angle. Each of the six plastic scintillation detectors measured 15 x 15 x 0.3 cm and was viewed by an RCA 6199 photomultiplier tube through an adiabatic Lucite light pipe. Each telescope required a threefold coincidence

and primarily counted pions scattered from the beam by the hydrogen and carbon in the polyethylene target. The threefold coincidences were scaled in CAMAC scalers.

The ion chamber consisted of eleven sheets of 6 μm doubly aluminized mylar, stretched on aluminum rings at 2.5 cm intervals along the beam direction. There were four low voltage signal plates interleaved between five high voltage plates while the two end plates were at ground and served primarily to seal the aluminum can which housed the chamber. The high voltage plates were maintained at 900 volts by a battery power supply. The current from the signal plates was integrated by an Ortec 439 current digitizer which put out a pulse for every 10^{-10} Coulombs of charge collected. The signal from the digitizer was scaled in both a visual preset scaler and a CAMAC scaler, with the preset scaler determining the length of the run as described in the next section. Argon was flowed through the chamber at a rate of 0.1 ℓ/m (replacing the volume about once every 3 hours) and a pressure of 0.3 cm of octoil above the ambient atmospheric pressure.

Data Acquisition

The data for this experiment were collected in data runs, lasting ~1/3 hour for elastic scattering and between ~1 hour and ~3 hours for π^+ production data. For a data run, the target flask was either empty or full of liquid hydrogen as appropriate, and the spectrometer was set to detect π mesons of the desired charge, angle and momentum. The computer was intialized and events were then accumulated during a run gate, which certified that operational requirements were met. After a preset amount of current had been accumulated from the ion chamber, data acqui-

sition was halted and the data were punched on paper tape and printed on a teletype. The former was read on another computer which was used for analysis, while the latter was retained for the experiment log.

The computer kept track of four histograms. Each histogram had nineteen bins, the number of counts in a bin indicating the number of events for which the corresponding surface barrier detector had registered a pulse. Events which showed a pulse in only one of the surface barrier detectors and no pulse in the Cerenkov detector were added to the first histogram. Events with exactly one pulse in the surface barrier detectors and a pulse in the Cerenkov detector were added to the second histogram. The third histogram consisted of events with exactly two of the surface barrier detectors producing a pulse, while the fourth histogram consisted of events with at least three of the surface barrier detectors producing a pulse. These latter two histograms ignored the Cerenkov detector.

A number of quantities of interest, which are listed in Table V, were scaled in CAMAC modules. The digitized signal from the ion chamber, which has a slow response time, was gated only by an interval gate which indicated that the run had commenced and was in progress. The remaining quantities were each scaled in two scalers, one gated by the run gate described below and one gated by the run gate but inhibited by the dead time pulse described above. The computer periodically read and cleared the scalers and accordingly adjusted its internal sums. A final read and clear was made when the run was terminated.

The presence of a run gate pulse indicated that four operating requirements were satisfied. First it testified that the interval gate

Table V. Quantities scaled during a run.

$S_1S_2S_3$	Triple coincidences in the trigger telescope
$W_1W_2W_3$	Triple coincidences in the west arm of the scattering monitor
$E_1E_2E_3$	Triple coincidences in the east arm of the scattering monitor
$W_1'W_2W_3$	Coincidences in the west arm with the signal from the first scintillator delayed
$E_1'E_2E_3$	Coincidences in the east arm with the signal from the first scintillator delayed
t	Pulses from a pulse generator operating at $\sim$ 10 Mhz
q_{IC}	Pulses from the current digitizer for the ion chamber

described above was present. Second it certified the presence of the beam gate. The primary proton beam at LAMPF had a duty factor of 6%, the protons struck the target which produced π mesons for the P^3 channel in 0.5 ms clusters at 8.33 ms intervals. Thus the π mesons arrived at the liquid hydrogen target with this same structure. Third it ensured that the computer was not in the process of reading the scalers. Lastly it guaranteed that a particular electronics noise source was absent. Due to a fault in the spectrometer power supply and the electronics for the surface barrier detectors, operation of the spectrometer produced significant spikes in the signals from the surface barrier detectors. These spikes were periodic and may have occurred only during the 94% of the time that π mesons were not striking the target, but none the less this source of accidentals was explicitly avoided by inhibiting operation for a period of 8 μs centered on the spikes.

CHAPTER III

AUXILIARY EXPERIMENTS AND ANALYSES

Several features of the measurement apparatus were investigated in auxiliary experiments. The relation between the shunt voltage and the central momentum of the spectrometer was calibrated with alpha particles from the dominant decay mode of ^{241}Am. The channel efficiencies were measured by sweeping a spectrum of π^+ mesons across each of the surface barrier detectors in turn. The dispersion of the spectometer was also determined through this procedure. A survey of the angular distribution of π^+p elastic scattering at 140 MeV was examined for systematic deviations from the known differential cross section. Lastly, the overall normalization of the measurement system was determined for each π^- beam utilized in the π^+ production study by observing π^-p elastic scattering with the same apparatus. These measurements also provided the distribution of momenta of the π^- in the incident beam. This chapter presents these procedures and analyses.

Calibration of Spectrometer Momentum Curve

The magnetic field strength in the spectometer magnets had previously been measured as a function of shunt voltage, and had been expressed in the compact form presented in Chapter II.[8] The proportionality constant between the field strength and the momentum of particles focused on the central detector remained to be determined accurately. An ^{241}Am alpha source, previously prepared for the calibration of the Low Energy Pion (LEP) channel at LAMPF, was well suited to this task. The ^{241}Am

had been deposited in a 0.1 x 1.0 cm rectangle on an aluminum disk, and could be positioned vertically to simulate the distribution of a π beam or horizontally to provide contrast. The spectrum of ^{241}Am includes alpha particles at 5443 keV (13%) and 5386 keV (2%) as well as at 5485.74 ± 0.12 keV (85%).[9] The alpha particles were detected by the surface barrier detectors described in Chapter II, and the unwanted secondary lines were eliminated on the basis of pulse height. The source thus effectively provided monoenergetic alpha particles. The 1 μCi strength was adequate, providing on the order of 150 counts per second when the discriminator was adjusted to ensure that only alpha particles from the 5486 keV line were being counted.

The alpha source was mounted in place of the cryogenic target at beam elevation with the aid of a surveyor's transit. The alpha particles were detected by either of two of the nineteen surface barrier detectors at the focal plane. The pulse from the detector amplifier chain was discriminated on the basis of pulse height and counted in a scaler which was read visually. The discrimination level was selected conservatively with the aid of a multichannel analyzer. The scaler was controlled by another scaler which halted the counting once a preset amount of time had elapsed.

The spectrometer was initiallized in the normal fashion; the current was brought to saturation, lowered to zero, brought to saturation a second time and lowered to the desired value. At this setting the alpha particles were focused just off the detector on the lower momentum side. Pulses from the detector were scaled for 20 sec., and the shunt voltage, indicating the current, and the number of counts were noted in the log. The current was reduced a small, constant amount and the procedure

iterated until the alpha particles had crossed the detector and were focused on the higher momentum side.

Spectra were acquired in this fashion for both the central detector (#10) and an adjacent detector (#9) with the source extended both vertically and horizontally. The spectrum for detector #10 with the source horizontal, shown in Fig. 9, is representative. This spectrum was remeasured, as a check on reproducibility, after the current had been lowered to zero, reversed (as if to detect negative particles), brought to saturation, lowered to zero, and again reversed (to detect positive particles).

The momentum of the alpha particles was associated with the centroid of the spatial distribution at the focal plane. In this way the momentum associated with a detector corresponded to the mean momentum of the particles detected provided the momentum distribution varied slowly. Table VI presents the determination of the proportionality constant based on each of the spectra. For detector #9 the dispersion determined in the next section is assumed. The uncertainties quoted for the central momentum reflect the uncertainty in the position of both the source and detector as well as in the momentum of the alpha particles. The uncertainty in the magnetic field strength is due principally to repeatability, but also includes the uncertainty in determining the centroid of the distribution. The results for the two detectors agree to within the expected 0.1%, while the uncanny agreement for the two orientations of the source must be considered a curiosity. The difference between the last two results for detector #10 is ascribed to the reproducibility of the field strength, as neither the source nor the detector had been disturbed, and

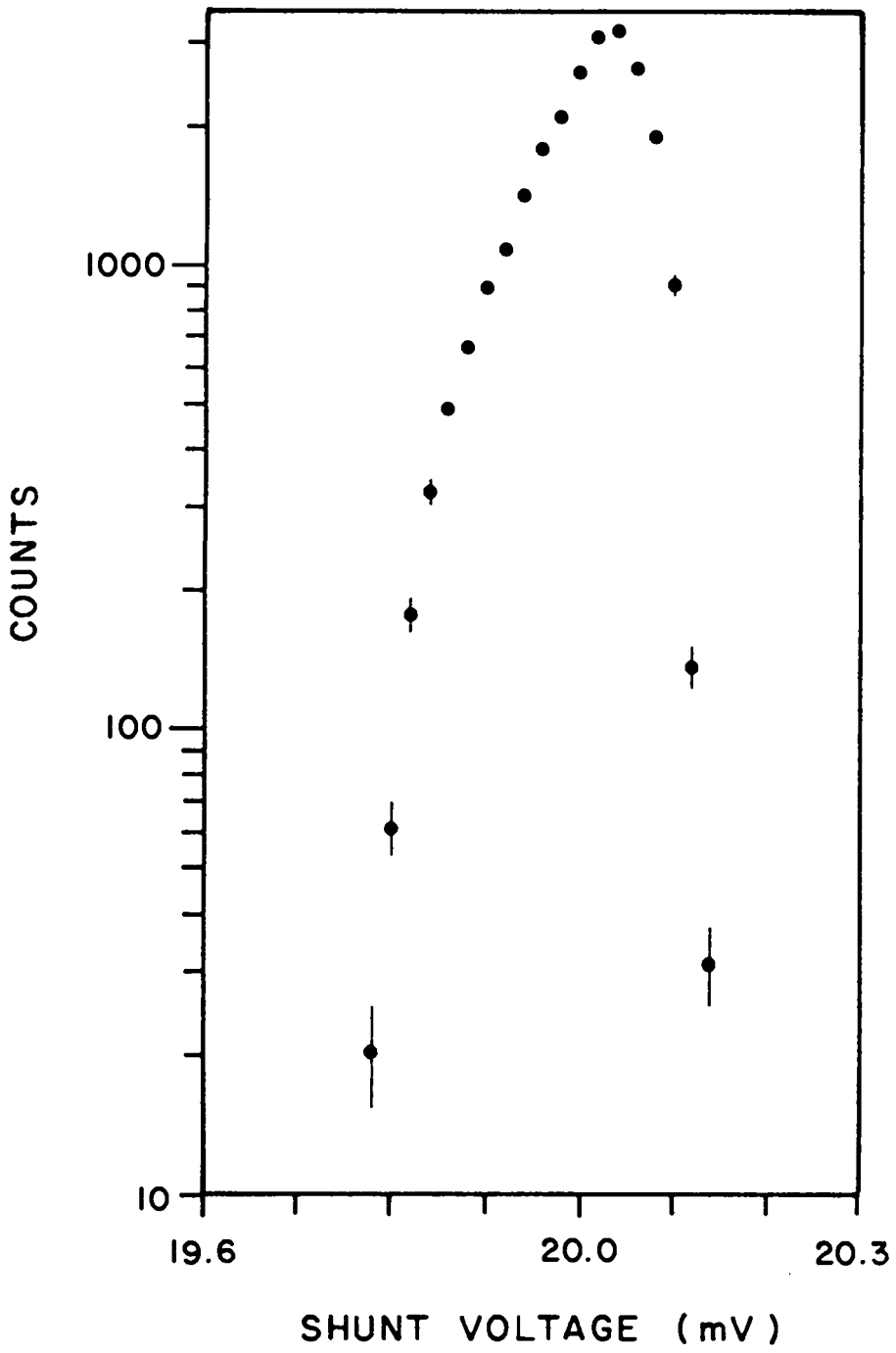

Fig. 9. Sample ^{241}Am spectrum for source extended horizontally.

Table VI. Results of ^{241}Am data. i is the detector number, V_s is the shunt voltage in mV, H is the average field strength for the two magnets in kG, P_c is the spectrometer momentum in MeV/c, and $a = P_c/H$ is in MeV/kGc.

i	V_s	H	P_c	a
		(a) Source extended vertically		
9	19.923	5.561±0.003	100.66±0.04	18.101±0.012
10	20.003	5.583±0.003	101.15±0.04	18.117±0.012
		(b) Source extended horizontally		
9	19.921	5.560±0.003	100.66±0.04	18.102±0.012
10	20.000	5.582±0.003	101.15±0.04	18.120±0.012
10	20.014	5.586±0.003	101.15±0.04	18.107±0.012

is of the order expected. The result quoted in Table II represents the average of these values.

Detection Channel Efficiencies

The measurement efficiency varied from channel to channel due primarily to geometrical differences, such as the solid angle acceptance of the channel and the fraction of the interaction region viewed by the channel, but also due to variations in the sensitive area of the surface barrier detectors. The efficiencies were therefore measured by marching a spectrum across the focal plane. In this way the spectrum was registered in each of the channels in turn, with the number of counts in a channel proportional to its efficiency. The efficiencies were determined within an unimportant overall constant. Also, the centroids of the spectra provided an accurate determination of the dispersion of the spectrometer.

The efficiencies were measured using a 140 MeV π^+ beam with $\Delta p/p$ of 3.8% (FWHM). The spectrometer was set to detect positive particles scattered from the liquid hydrogen target at a laboratory angle of 50^o. For the initial shunt voltage nearly all of the π^+ mesons elastically scattered from the hydrogen had insufficient momentum to be passed by the spectrometer. Events were accumulated until a preset amount of charge had been collected from the ion chamber, at which time the computer output the data. The shunt voltage was decreased a small amount and the procedure repeated until the elastic peak had passed across each of the channels in turn and once again only a small fraction of the elastically scattered π^+ mesons were able to pass through the spectrometer.

The raw data was thus divided into 48 runs, one for each value of the shunt voltage. The data for each run consisted of the usual four

histograms and the accompanying scaler totals. The histogram of the events for which only one of the channels detected a particle, and the number of counts in the scattering monitor during live time for the computer were of interest. The number of counts in each bin was divided by the number of live time counts in the scattering monitor and also by the central momentum (calculated from the shunt voltage). The former normalized each run to the same number of π^+ mesons incident on the target during live time, while the latter accounted for the variation in momentum acceptance with central momentum. Finally the bin values were rescaled by a convenient number and resorted according to channel number providing a spectrum for each of the channels.

Each spectrum was fitted to a skewed Gaussian peak plus a constant and an error function term

$$f(x) = \zeta_1 \zeta_2^{-1} (2\pi)^{-\frac{1}{2}} \exp(-z^2/2) \{1-\zeta_4 z(1-z^2/3)/2\} + \zeta_5 + \zeta_6 (2\pi)^{-\frac{1}{2}} \int_z^\infty \exp(-y^2/2)\, dy,$$

with $z = (x-\zeta_3)/\zeta_2$.

The parameters ζ_i were optimized by the nonlinear least squares algorithm described in Appendix A. Some sample spectra with the fitted curves are shown in Fig. 10. This form was justified by a degree of success. The spectra for the three channels which detect particles of the highest momenta contained too few points on the low momentum side of the peak. Consequentially ζ_6 could not be determined by the least squares algorithm, and necessarily was assigned a value. The results of the analysis were relatively insensitive to the particular value assigned.

The efficiencies were proportional to the areas under the peak,

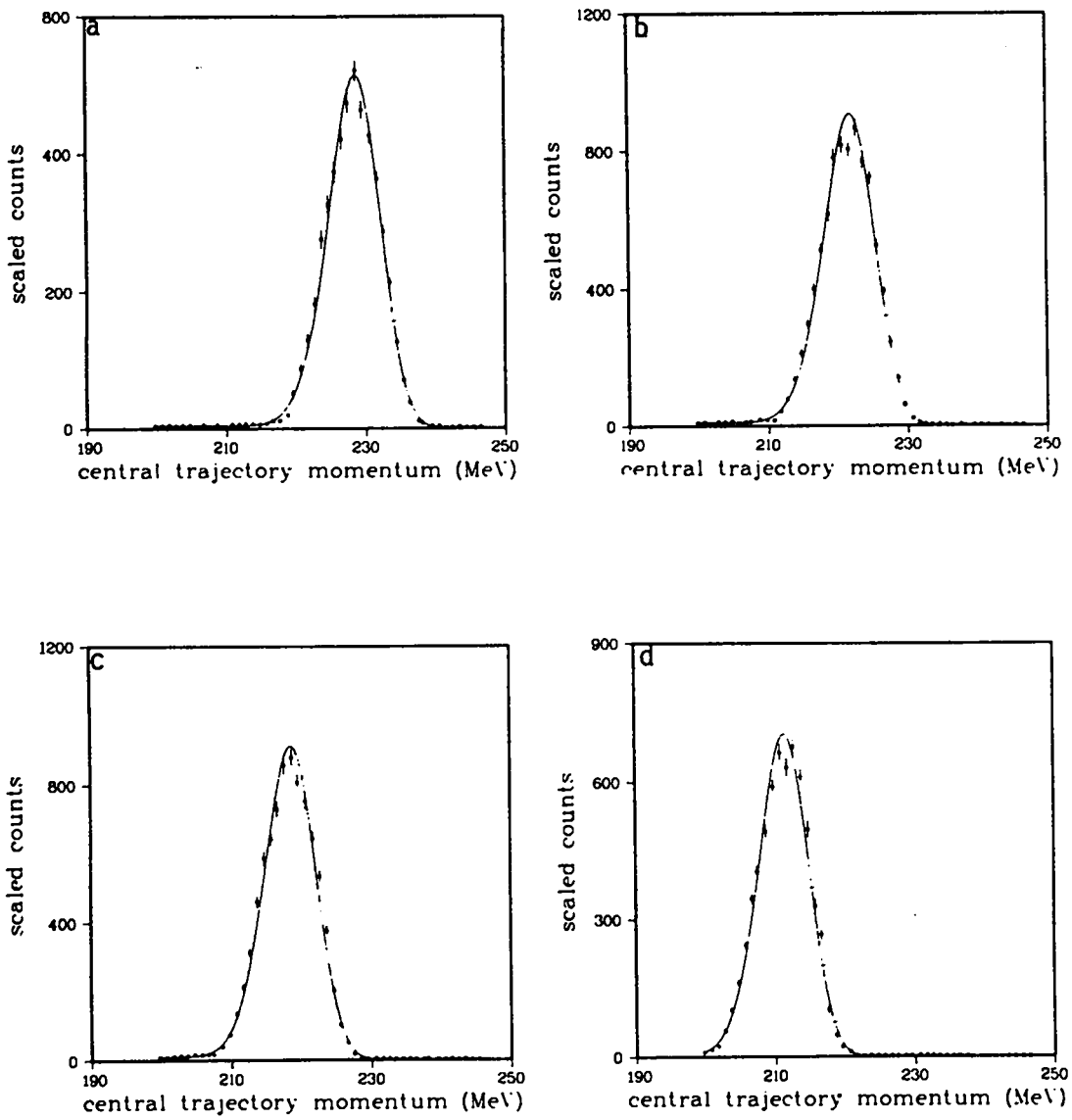

Fig. 10. Sample spectra for channel efficiencies. The curve was determined by the least squares fitting procedure.

hence the values of ζ_1. The relative efficiencies were defined as

$$\eta_i = \zeta_{1,i}/\zeta_{1,10}$$

with uncertainties

$$\Delta\eta = (\Delta\zeta_{1,i})/\zeta_{1,10}$$

where i indicates the channel number and $\Delta\zeta_{1,i}$ are the uncertainties in $\zeta_{1,i}$ provided by the algorithm. This set of data provided a relative efficiency for each of the detectors, with a statistical uncertainty of about 1%. Although this determination appeared to be completely adequate, the study was repeated as a test of reproducibility. The second study was the same in every respect except that the momentum width of the beam was narrower, $\Delta p/p = 2.1\%$, and hence so was the spectrum of scattered π^+ mesons. This resulted in a set η_1 of seventeen relative efficiencies since two of the surface barrier detectors were malfunctioning. The two sets were compared by defining a χ^2,

$$\chi^2 = \sum_i \{ (\frac{\eta_i - \overline{\eta_i}}{\Delta\eta_i})^2 + (\frac{a\eta_i' - \overline{\eta_i}}{a\Delta\eta_i'})^2 \}$$

where the sum is over the operative channels, and minimizing with respect to a and the $\overline{\eta_i}$. The scale factor allows for the unknown difference in normalization for the two sets of relative efficiencies. The $\overline{\eta_i}$ are then

$$\overline{\eta_i} = \{ \frac{\eta_i}{(\Delta\eta_i)^2} + \frac{a\eta_i'}{(a\Delta\eta_i')^2} \} / \{ \frac{1}{(\Delta\eta_i)^2} + \frac{1}{(a\Delta\eta_i')^2} \}.$$

The uncertainties were obtained in the same manner as discussed in Appendix A. These $\overline{\eta_i}$ and their relative, statistical uncertainties were renormalized to obtain $\overline{\eta_{10}} = 1$, and are presented in Table IV. The

minimum chi-square was 38 with 16 degrees of freedom, indicating that the two sets of relative efficiencies possessed different shapes. The difficulty was associated with the three channels for which ζ_6 was necessarily fixed in both studies. As there were no apparent grounds for preferring either determination over the other, the merged values were taken as the best estimates. Aside from these three channels, the two studies were in good agreement showing that the measurements were stable and reproducible.

The spectrometer dispersion was also determined from these data. The centroids ζ_3 of the peak in the spectra represent the values of the central momentum for which the elastic peak was successively centered on each of the surface barrier detectors. In the lowest order approximation, wherein the dispersion δ is taken to be constant, the spectrum centroids are related to the channel number i and the centroid of the detected momentum distribution P by

$$y_i = P/\{1 + (i-10)\delta\}.$$

The $\zeta_{3,i}$ with their uncertainties $\Delta\zeta_{3,i}$, from the analyses of the spectra, were fitted to this form treating both P and δ as free parameters. The fitted curve and the points for the first study are shown Fig. 11. The constant dispersion approximation does remarkably well. The χ^2/ν was 2.9, in part due to a 0.5 mm uncertainty in the positions of the detectors (which was ignored). The dispersion was determined to be 0.4893 ± 0.0008 % per channel from the first study and 0.4896 ± 0.0006 % per channel from the second study. The dispersion was assigned the mean value of 0.4895 % per channel or 0.4351 % per cm with a statistical uncertainty of one part in 10^3.

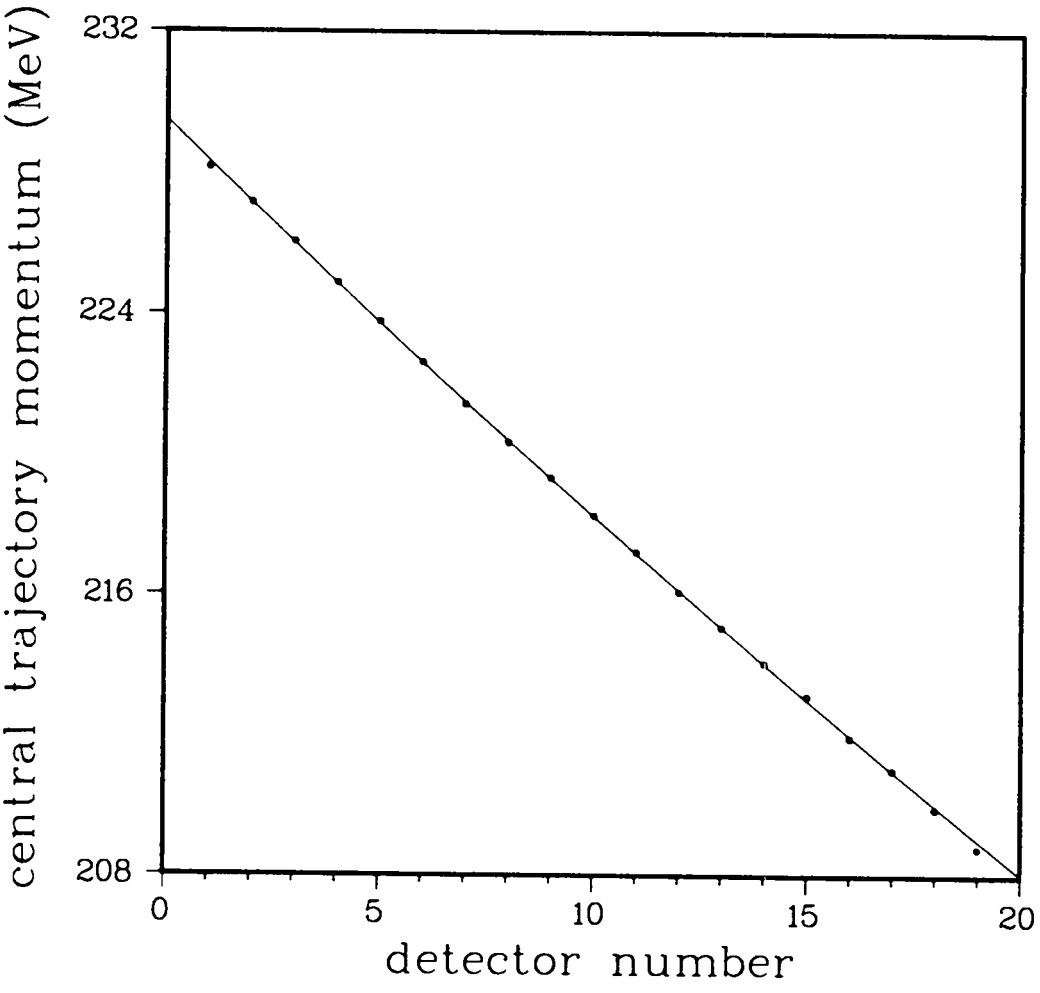

Fig. 11. Data for spectrometer dispersion. The curve was determined by the least squares fitting procedure.

Angular Survey of π^+p Elastic Scattering

The solid angle acceptance of the spectrometer was expected to vary slightly with laboratory angle because the interaction region was not cylindrically symmetric. Therefore, a study of π^+p elastic scattering at 140 MeV was carried out, and the resulting angular distribution was examined for systematic deviation from the prediction of SCATPI,[10] a subroutine based on a phase shift analysis (described in Chapter IV). The predictions are quite successful in this region, allowing a comparison on the 1% level. Furthermore, the momenta of the scattered π^+ mesons were low enough to allow measurement as far forward as 35^o in the laboratory. The analysis of the elastic spectra also provided the momentum distribution of the incident π^+ beam. Thus this study additionally provides a basis for evaluating the consistency of these results.

The investigation was made with a beam of 140 MeV π^+ mesons having a $\Delta p/p$ of 2.1% (FWHM). The π^+ mesons elastically scattered from protons were detected by the spectrometer for each of twelve angles from 35^o to 130^o in the laboratory. The data for an angle were converted into a spectrum, and the spectrum analyzed to determine the area under the elastic peak. The areas were corrected for π^+ decay and renormalized to agree on the average with the predicted π^+p differential cross section. The remaining discrepancies were scrutinized for a systematic pattern. The analysis of the spectrum revealed the momentum distribution of the beam through the two body kinematics. The results for the twelve spectra were examined for consistency.

The data for an angle consisted of the histogram of events for which only one of the channels had detected a particle, the sums of the

scaler events, the laboratory angle, and the spectrometer shunt voltage. The shunt voltage determined the central momentum P_C and hence the momenta p_i of the particles detected in each of the channels

$$p_i = P_C \{ 1 + (i-10)\delta \},$$

with i the channel number and δ the spectrometer dispersion in percent per channel. The number of counts n_i in each channel was corrected for the channel efficiency η_i and the momentum acceptance $P_C\delta$, and normalized by the number of counts M_ℓ in the scattering monitor during live time,

$$y_i = n_i/(M_\ell \eta_i P_C \delta).$$

The spectrometer blocked a portion of the beam from reaching the scattering monitor for laboratory angles forward of about 40^o, hence for the measurement at 35^o M_ℓ above was replaced with M_ℓ', the corrected sum of the live time counts in the monitor

$$M_\ell' = \langle M_T/q_{IC} \rangle \, q_{IC} \, M_\ell/M_T.$$

Here M_T was the number of counts in the scattering monitor ignoring the dead time inhibit, q_{IC} was the charge collected from the ion chamber, and the average was over the values from the other eleven angles. The uncertainty in y_i was

$$\Delta y_i = y_i \{ (\Delta n_i/n_i)^2 + (n_i+1)/n_i^2 \}^{\frac{1}{2}}$$

where, since M_ℓ, P_C and δ were the same for each channel, their uncertainties were not included.

The y_i were fitted to much the same function as was employed in

the previous section

$$f(p_i) = \zeta_1\zeta_2^{-1}\ (2\pi)^{-\frac{1}{2}} \exp(-z^2/2)\{\ 1-\zeta_4\ z(1-z^2/3)/2\}$$
$$+\ \zeta_5 + \zeta_6\ (2\pi)^{-\frac{1}{2}} \int_z^{\infty} \exp(-x^2/2)\ dx,$$

with

$$z = (p_i-\mu)/\sigma.$$

Here, however, the centroid μ and the width σ of the detected momentum distribution were parameterized in terms of the momentum distribution of the incident π^+ beam. The centroid was computed as

$$\mu = p - p_{loss} - p_{ang}$$

where p is the momenum of the scattered π meson calculated from kinematics from ζ_3, the mean momentum of the incident beam, p_{loss} is a correction for momentum lost to atomic electrons in the target and p_{ang} is a correction due to the difference between the mean scattering angle and the nominal scattering angle resulting from the finite angular acceptance of the spectrometer and emittance of the pion channel. p_{loss} and p_{ang} depend on ζ_3, and are presented in Appendix B. The width was calculated as

$$\sigma = \{\ (\frac{dp}{d\zeta_3}\ \zeta_2)^2 + \sigma^2_{spot} + \sigma^2_{ang} + \sigma^2_{loss} + \sigma^2_{coul} + \sigma^2_{strag}\}^{\frac{1}{2}}$$

The first term represents the contribution from the momentum spread of the incident beam, while σ^2_{spot} represents the contribution arising from the extended image of the interaction region at the focal plane. σ_{spot} is easily calculated from the vertical extent of the beam, the magnification of the spectrometer, and the dispersion of the spectrometer. Briefly, σ^2_{ang} is the contribution from the mean square variation in the cosine of the scattering angle due to the finite angular emittance of

the channel and acceptance of the spectrometer, σ^2_{loss} is due to the mean square variation in the momentum lost in the target through variation in the path length in the target, σ^2_{coul} is due to the mean square variation in the scattering angle which results from the small angle Coulomb scattering, and σ^2_{strag} is due to the mean square variation in the momentum lost to atomic electrons through the stochastic nature of collisions. These four contributions all depend on the beam momentum ζ_3 and each is presented in Appendix B. The quadrature summation of these terms is justified only by a degree of success.

Thus the least squares analysis at each angle determined the area under the skewed Guassian peak, and also the centroid ζ_3 and width ζ_2 of the momentum distribution of the incident beam. Some examples of the spectra and fitted curves are shown in Fig. 12. Each area was converted to a center of momentum cross section

$$\frac{d\sigma}{d\Omega} = \zeta_1 \; E \; J \; T$$

with an uncertainty determined in the same way from the uncertainty in the area (provided by the least squares analysis). Here E is a correction for pion decay, J is the Jacobian of the transformation, and T is an overall factor (which depends on the target thickness, the solid angle acceptance of the spectrometer, and the efficiency of the scattering monitor) determined such that the cross sections agree on the average with the predictions. The decay correction was

$$E = \exp\{\Lambda m_\pi/(\tau p)\}$$

in which Λ is the mean path length between the target and the focal plane, m_π and τ respectively are the rest mass and lifetime of the charged pion, and p is still the mean momentum of the pions scattered

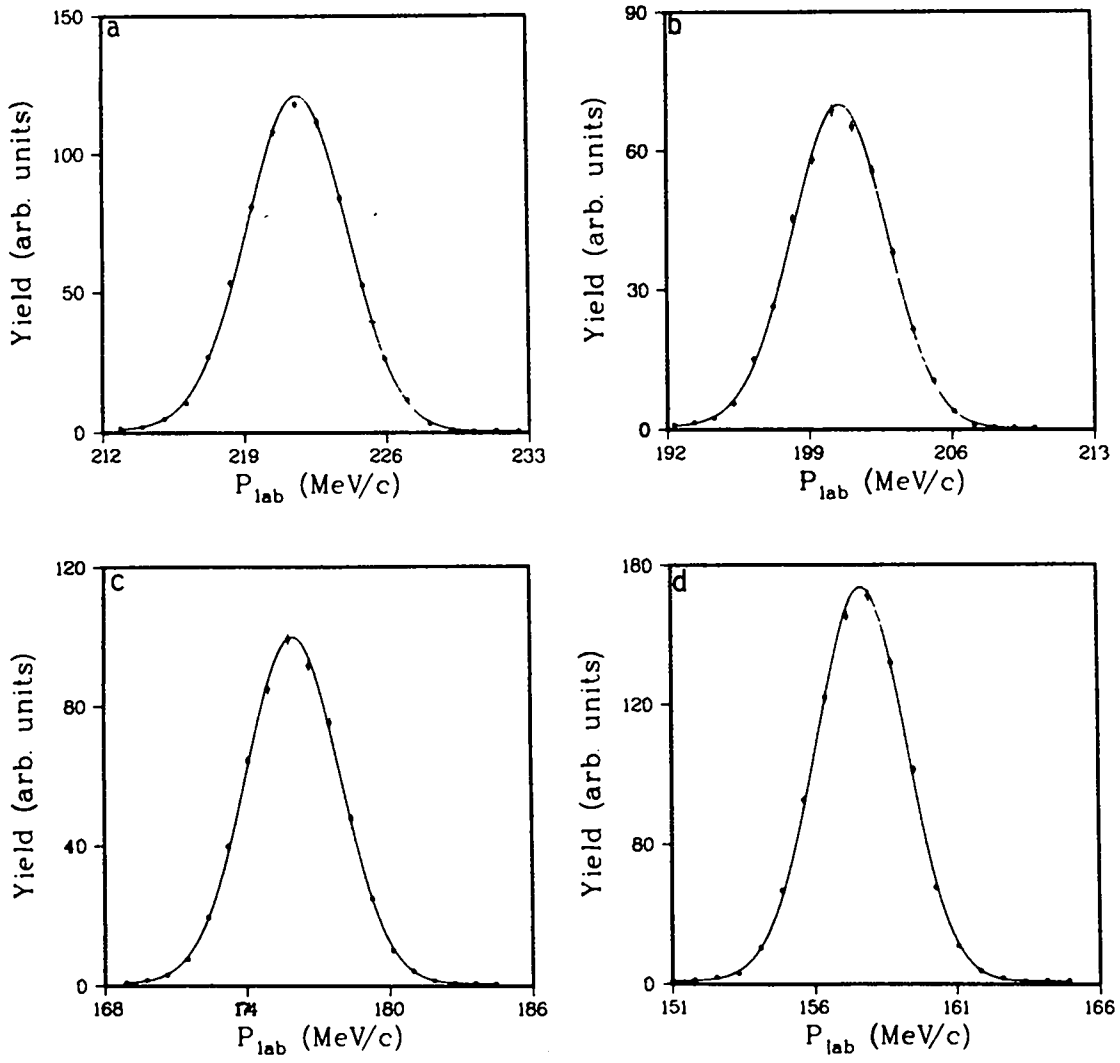

Fig. 12. Sample spectra for $\pi^+p \rightarrow \pi^+p$. Spectra are for channels a) 1, b) 7, c) 10 and d) 17. The curve was determined by the least squares fitting procedure.

at the angle. The Jacobian was

$$J = \left|\frac{d \cos \theta_{LAB}}{d \cos \theta}\right| = \left|p \left(T_{LAB} T - \gamma m_\pi^2\right) / m_\pi^3\right|$$

where T is the kinetic energy of the scattered pion and the subscript LAB denotes in the laboratory frame. The overall factor T was chosen to minimize the χ^2,

$$\chi^2 = \sum_i \{ y_i - f_i \}^2 / \{ (\Delta y_i)^2 + (\Delta f_i)^2 \}$$

where y_i represents the measured cross section and f_i is the value predicted by SCATPI using the beam momentum corrected for loss of energy entering the target, and the sum is over all angles. The beam momentum was the weighted average of the ζ_3

$$P_{Beam} = \{ \sum_i \zeta_{3,i} (\Delta\zeta_{3,i})^{-2} \} / \{ \sum_j (\Delta\zeta_{3,j})^{-2} \}$$

where $\Delta\zeta_{3,i}$ is the uncertainty in $\zeta_{3,i}$ provided by the least squares algorithm. The root mean square momentum variation ΔP was calculated in the same way from the $\zeta_{2,i}$ and $\Delta\zeta_{2,i}$.

The results of this analysis are presented in Table VII and the angular distribution is compared with the predicted cross section in Fig. 13. The figure reveals a 1.5% variation from forward to backward angles, which is not understood. Neither is an apparent systematic trend in the individual values of the beam momentum; however, the root mean square variation of the values is 0.13 MeV/c, which may be a better estimate of the uncertainty in each measurement than the standard deviation provided by the fitting algoithm (which assumes that the form of the function $f(p_i)$ is correct). The estimates of the beam width are consistent within the uncertainties provided by the fitting algorithm. The results of the second angular survey, presented in Table VIII and Fig. 14,

Table VII. Angular survey of $\pi^+ p \rightarrow \pi^+ p$ at 140 MeV. P_{beam} and ΔP are the mean and root mean square variation of the incident momenta. θ_{lab} is in degrees, $d\sigma/d\Omega$ is in mb/sr, and P_{beam} and ΔP are in MeV/c.

θ_{lab}	cos θ	$\frac{d\sigma}{d\Omega}$	P_{beam}	ΔP	χ^2/ν
35	0.719	12.19 ± 0.08	242.22 ± 0.02	2.18 ± 0.02	4.36
40	0.643	10.73 ± 0.07	242.30 ± 0.02	2.16 ± 0.02	3.37
45	0.561	9.72 ± 0.07	242.29 ± 0.02	2.21 ± 0.02	2.28
50	0.474	8.69 ± 0.06	242.19 ± 0.02	2.21 ± 0.02	2.60
60	0.293	7.16 ± 0.06	242.15 ± 0.03	2.29 ± 0.03	1.11
70	0.107	6.59 ± 0.06	242.08 ± 0.03	2.18 ± 0.04	2.50
80	-0.075	7.12 ± 0.06	242.01 ± 0.03	2.21 ± 0.04	2.79
90	-0.247	8.68 ± 0.07	242.18 ± 0.03	2.21 ± 0.04	1.89
100	-0.404	10.75 ± 0.09	241.95 ± 0.03	2.18 ± 0.04	1.17
110	-0.545	13.32 ± 0.10	241.99 ± 0.03	2.17 ± 0.03	2.61
120	-0.667	16.11 ± 0.12	241.91 ± 0.03	2.18 ± 0.03	1.19
130	-0.770	19.16 ± 0.14	242.03 ± 0.02	2.19 ± 0.03	2.57

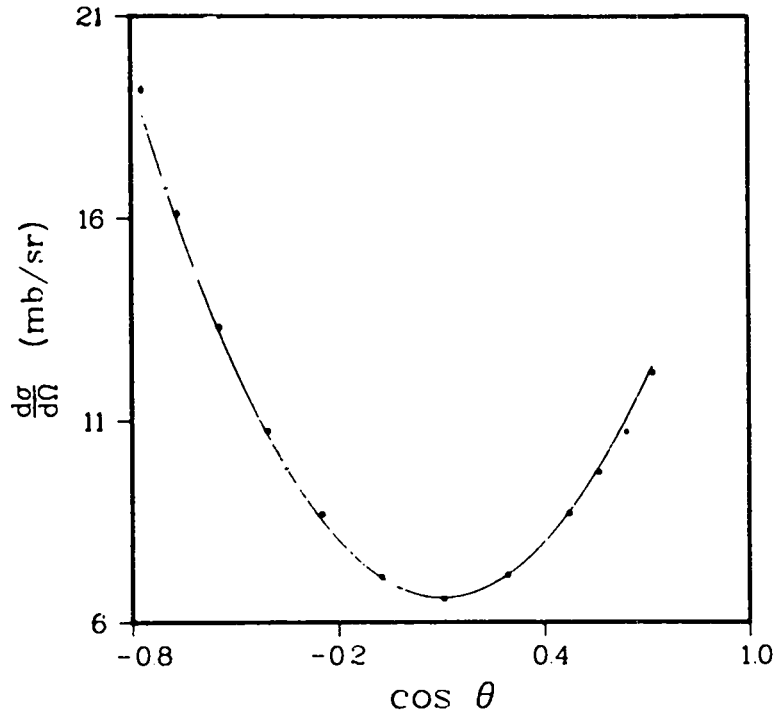

Fig. 13. Angular distribution of $\pi^+p \rightarrow \pi^+p$ at 140 MeV. The points have been normalized to agree as well as possible with the curve. The curve represents the interpolation of SCATPI.

Table VIII. Repeat angular survey of $\pi^+p \rightarrow \pi^+p$ at 140 MeV.

Entries are the same as in Table VII.

θ_{LAB}	cos θ	$\frac{d\sigma}{d\Omega}$	P_{Beam}	ΔP	χ^2/ν
40	0.643	11.26 ± 0.11	242.76 ± 0.03	2.15 ± 0.03	4.04
70	0.107	6.63 ± 0.06	242.59 ± 0.04	2.25 ± 0.04	1.61
90	-0.247	8.52 ± 0.08	242.79 ± 0.04	2.21 ± 0.04	1.06
110	-0.545	13.15 ± 0.12	242.45 ± 0.04	2.15 ± 0.04	5.09
130	-0.770	18.78 ± 0.17	242.24 ± 0.03	2.13 ± 0.04	2.96

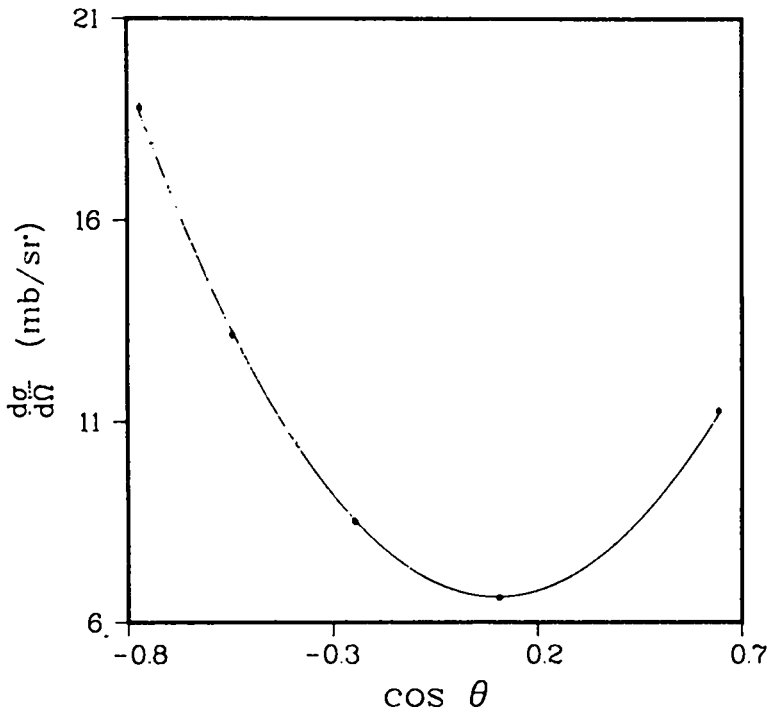

Fig. 14. Repeat of angular distribution of $\pi^+p \rightarrow \pi^+p$ at 140 MeV. The points have been normalized to agree as well as possible with the curve. The curve represents the interpolation of SCATPI.

show neither of the trends evident in the first study. Only five angles were included the second time; however, it is noteworthy that the measurements reproduce the predicted angular distribution. The target flask had been repositioned during a two week interruption, but it is not clear that this is the only or the complete explanation. The root mean square variation in the estimates of the beam momentum is 0.23 MeV/c, again hinting that the statistical uncertainty is too small. The beam momentum was determined to be 242.11 MeV/c and 242.57 MeV/c for the two studies, suggesting that it is reproducible to about 0.2%.

π^-p Elastic Scattering

Elastic scattering of the π^- meson from protons was measured for each π^- beam employed in the π^+ production study. These data were analyzed very much the same as the π^+p data in the preceding section. The effective target thickness, the spectrometer solid angle acceptance to lowest order and the efficiency of the scattering monitor were thus determined together, avoiding the chore of evaluating each separately. This analysis also provided the momentum distribution for each of the incident π^- beams, which are used in the analysis of the reaction measurements.

Measurements for π^-p elastic scattering were made beginning as far forward as permitted by the upper momentum limit of the spectrometer and proceding to 130^0 in 10^0 increments in the laboratory. These data were analyzed in the same manner as described in the previous section except that, in the function fitted to the spectra, the error function term was excluded. Due to the $\Delta p/p$ of 4% for the π^- beams, the background levels above and below the elastic peak were inadequately defined to include the

error function term while allowing the peak to be skewed. Also, as described in Chapter IV, the cross section predictions used to determine T for the two highest energy beams were not provided by SCATPI, but rather by a graphical method.

Some example spectra are presented for each energy in Fig. 15 through 20. The results of the analyses of the spectra are displayed in Table IX and Fig. 21 for 229 MeV, Table X and Fig. 22 for 254 MeV, Table XI and Fig. 23 for 279 MeV, Table XII and Fig. 24 for 292 MeV, Tables XIII and XIV for 330 MeV and Tables XV and XVI for 356 MeV. Table XVII is a distillation of these results, presenting the values of T, P_{Beam}, ΔP and their root mean square variations for each beam. The variations in T for the lowest four energies are consistent with the 1 to 1½% accuracy of the cross section measurements. For the two higher energies the agreement is lesser, presumably reflecting the consistency of the graphical interpolation of the cross sections. The variations in P_{Beam}, the beam momentum, are about 0.07%, more than twice the statistically expected 0.03%. This may indicate the level of adequacy of the form fitted to the spectra, the computation of ζ_3 from the mean momentum of the scattered π mesons, or other factors. The values of ΔP are consistent to within their statistical uncertainties. The values of the beam momentum and root mean square variation corrected for loss of energy in the target are listed in Table XVIII. Along with T from Table XVII, these were used in analyzing the reaction data.

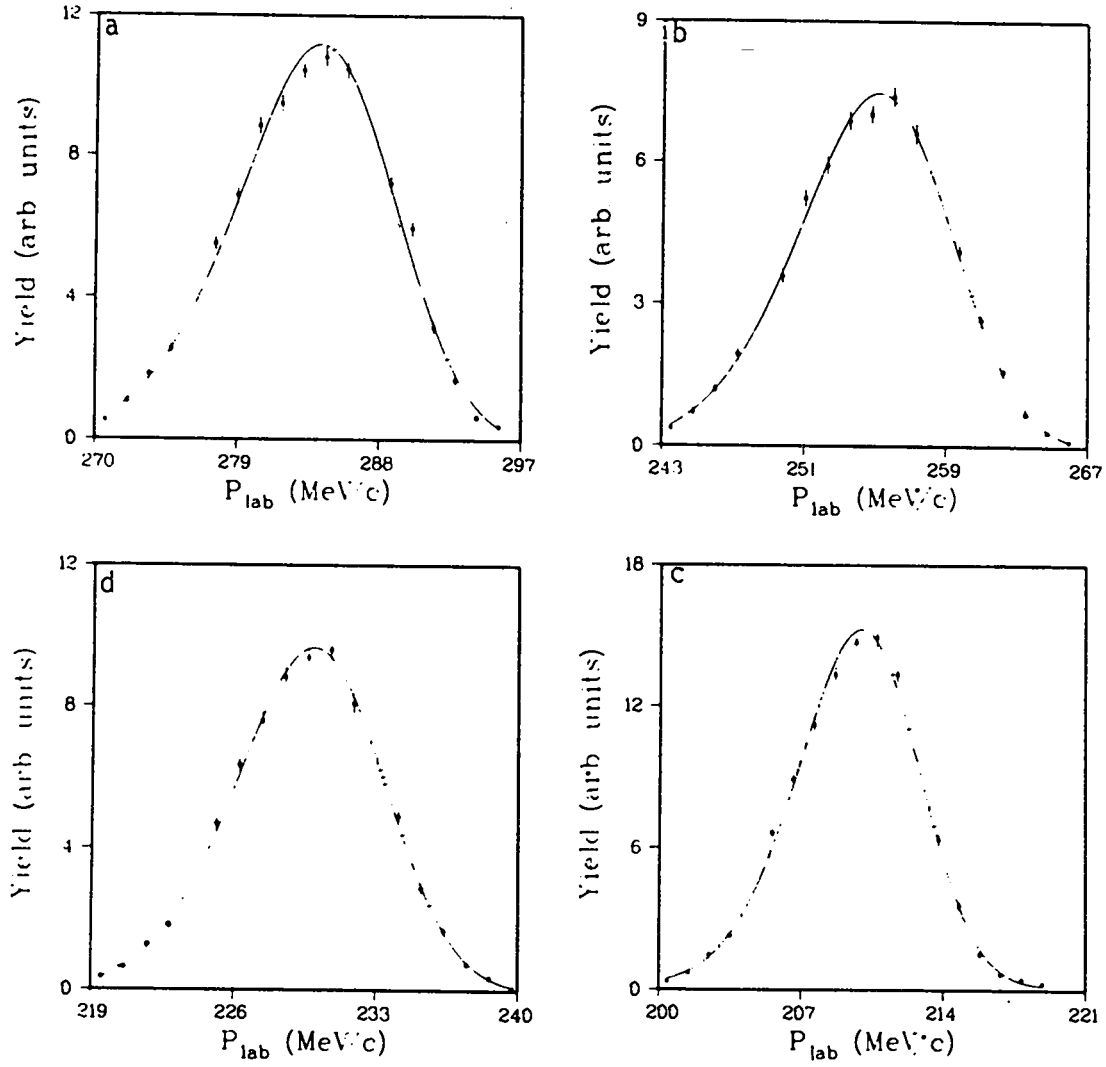

Fig. 15. Sample spectra for $\pi^-p \to \pi^-p$ at 229 MeV. Spectra are for the laboratory angles a) 60°, b) 80°, c) 100° and d) 120°. The curve was determined by the least squares fitting procedure.

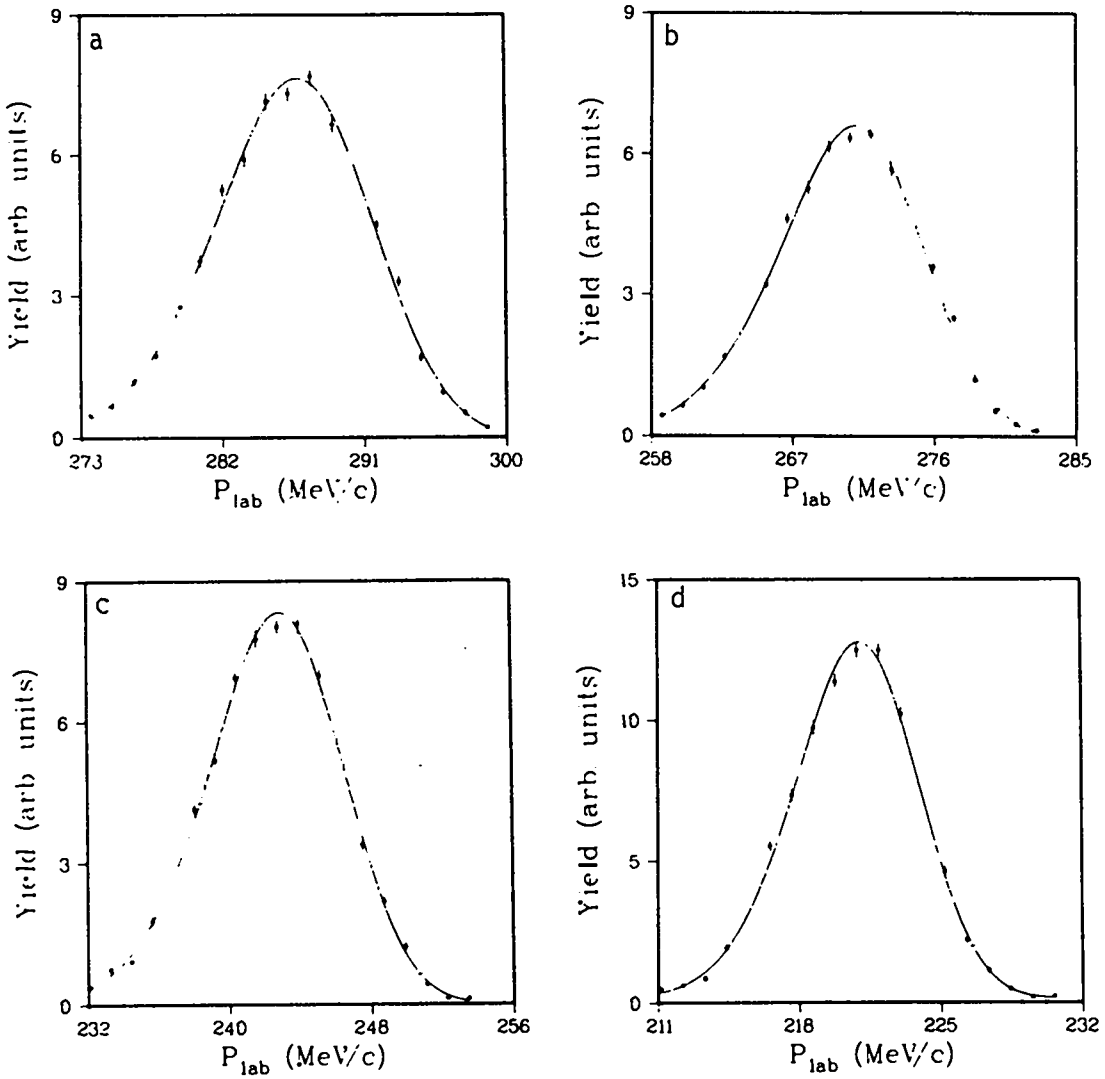

Fig. 16. Sample spectra for $\pi^-p \to \pi^-p$ at 254 MeV. Spectra are for the laboratory angles a) 70°, b) 80°, c) 100° and d) 120°. The curve was determined by the least squares fitting procedure.

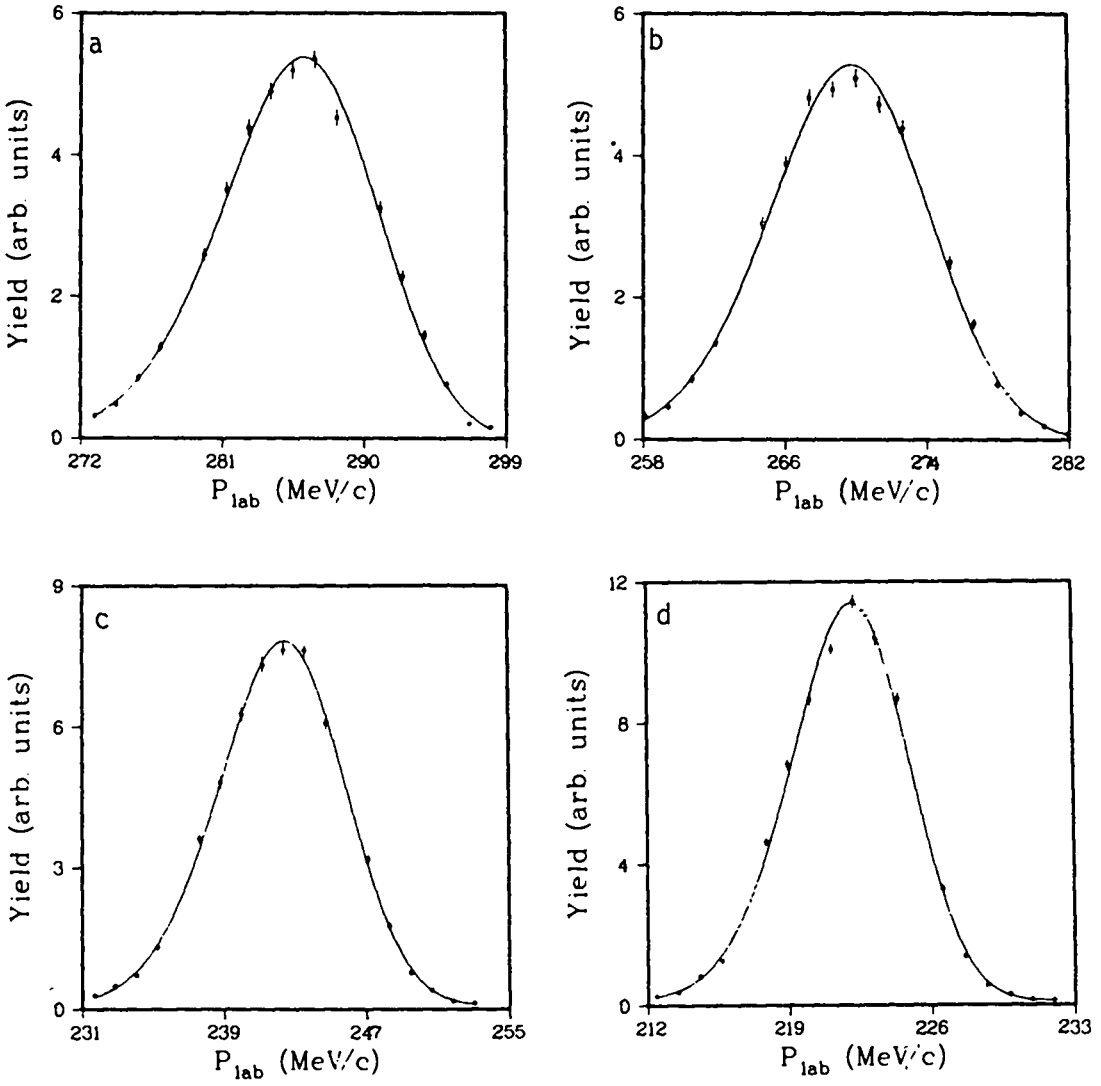

Fig. 17. Sample spectra for $\pi^- p \rightarrow \pi^- p$ at 279 MeV. Spectra are for the laboratory angles a) 80°, b) 90°, c) 110° and d) 130°. The curve was determined by the least squares fitting procedure.

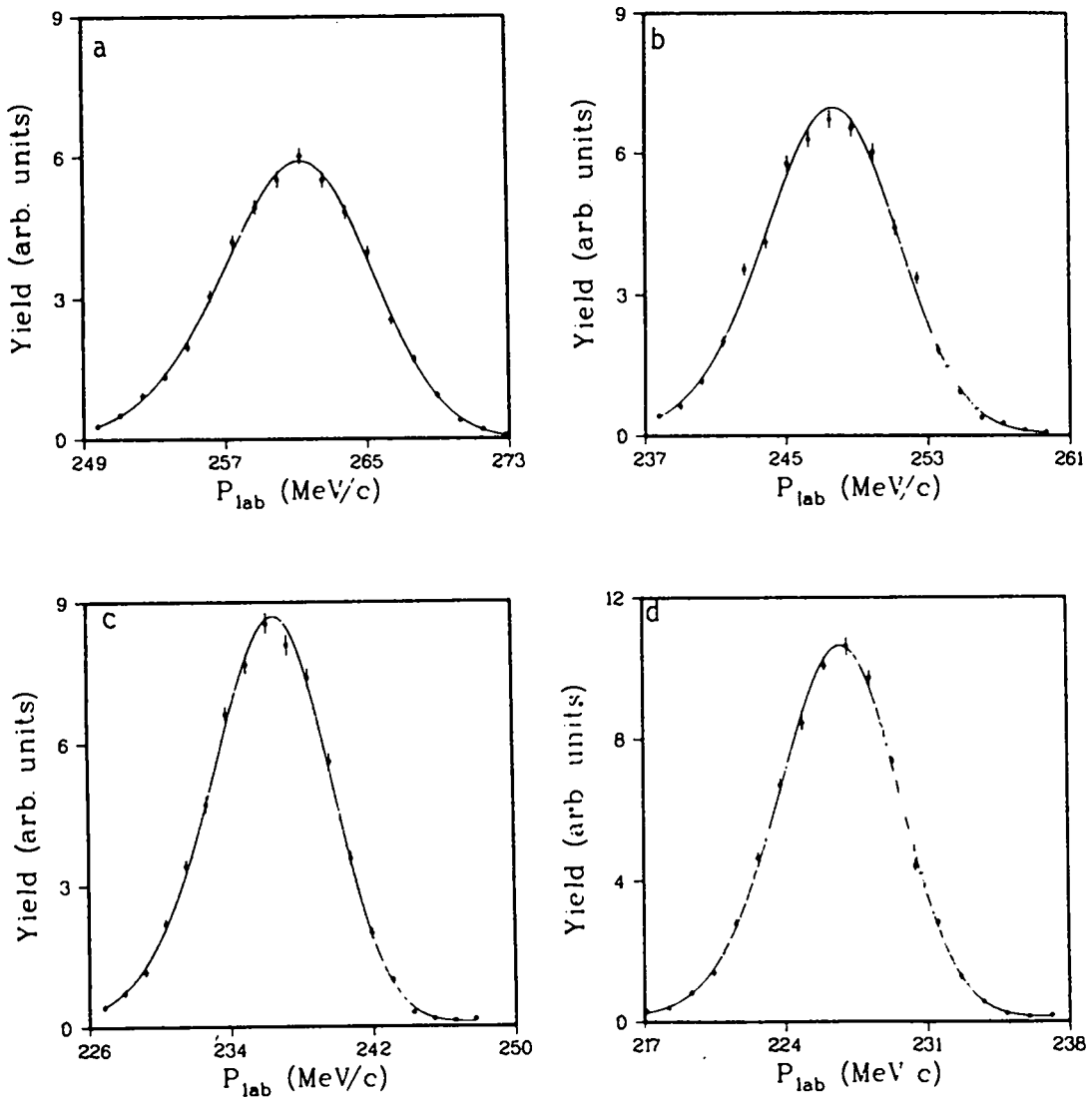

Fig. 18. Sample spectra for $\pi^-p \to \pi^-p$ at 292 MeV. Spectra are for the laboratory angles a) 100°, b) 110°, c) 120° and d) 130°. The curve was determined by the least squares fitting procedure.

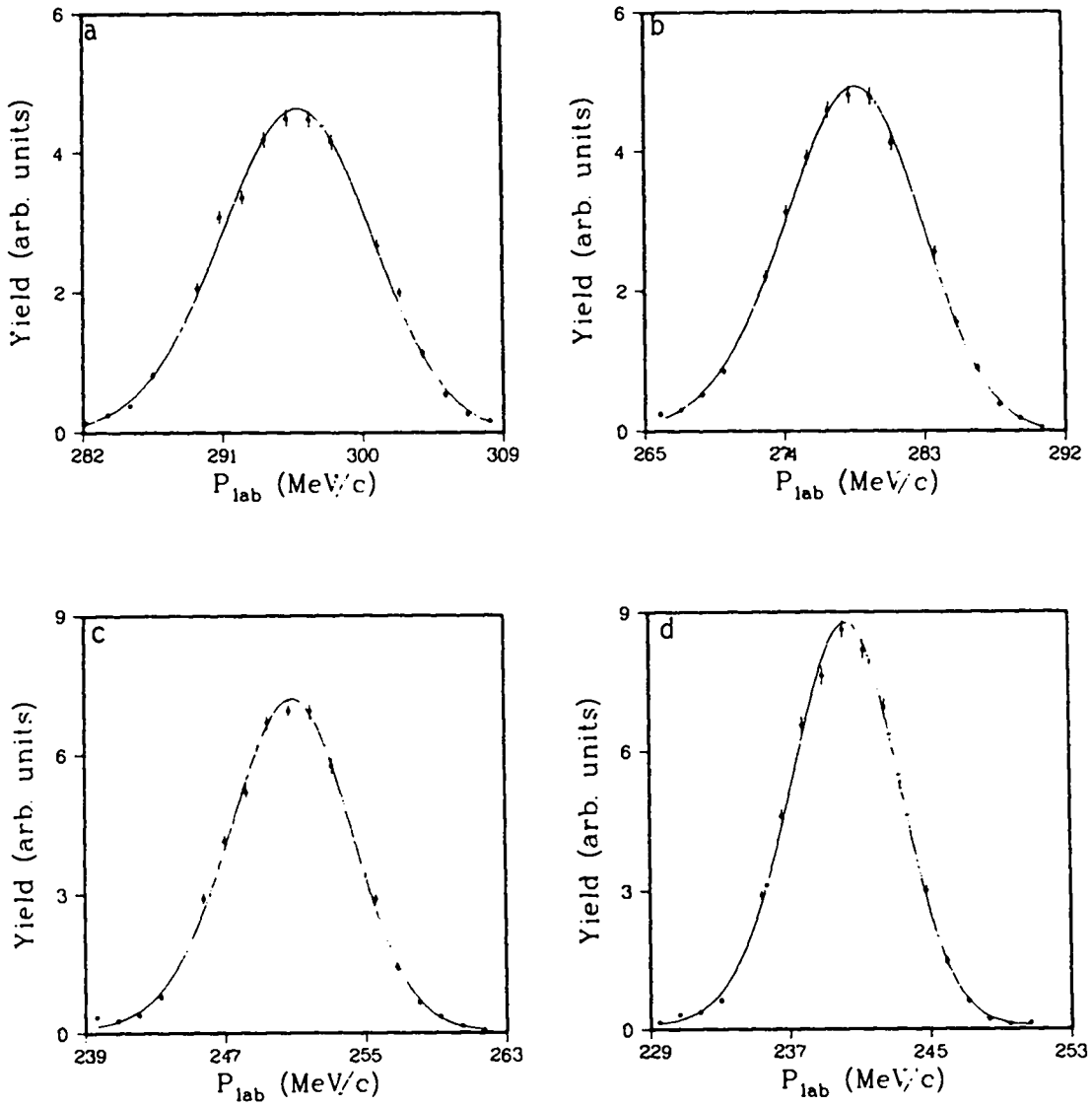

Fig. 19. Sample spectra for $\pi^- p \rightarrow \pi^- p$ at 330 MeV. Spectra are for the laboratory angles a) 90°, b) 100°, c) 120° and d) 130°. The curve was determined by the least squares fitting procedure.

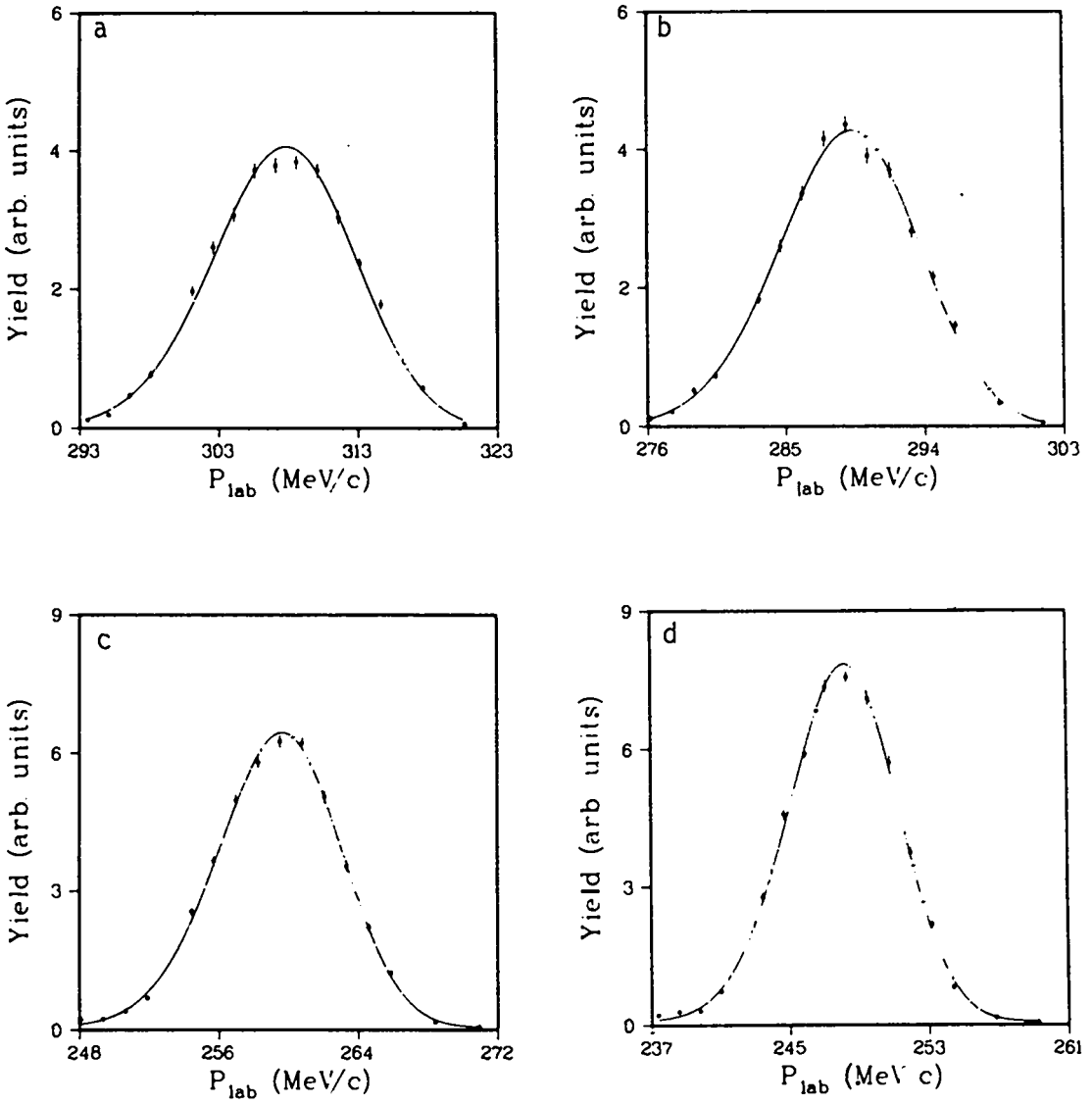

Fig. 20. Sample spectra for $\pi^- p \to \pi^- p$ at 356 MeV. Spectra are for the laboratory angles a) 90°, b) 100°, c) 120° and d) 130°. The curve was determined by the least squares fitting procedure.

Table IX. Results from $\pi^- p \rightarrow \pi^- p$ at 229 MeV. Entries are the same as in Table VII.

θ_{LAB}	cos θ	$\frac{d\sigma}{d\Omega}$	P_{Beam}	ΔP	χ^2/ν
60	0.241	0.878 ± 0.020	341.20 ± 0.09	5.98 ± 0.17	2.75
70	0.052	0.696 ± 0.014	340.81 ± 0.10	5.96 ± 0.15	1.82
80	-0.129	0.641 ± 0.013	340.62 ± 0.10	6.00 ± 0.16	0.92
90	-0.298	0.716 ± 0.014	341.18 ± 0.10	5.91 ± 0.16	0.92
100	-0.450	0.894 ± 0.014	340.94 ± 0.10	6.05 ± 0.13	0.80
110	-0.583	1.129 ± 0.017	340.99 ± 0.09	6.10 ± 0.12	1.55
120	-0.697	1.412 ± 0.019	341.18 ± 0.09	5.87 ± 0.10	2.17
130	-0.791	1.666 ± 0.020	340.96 ± 0.08	5.49 ± 0.09	2.95

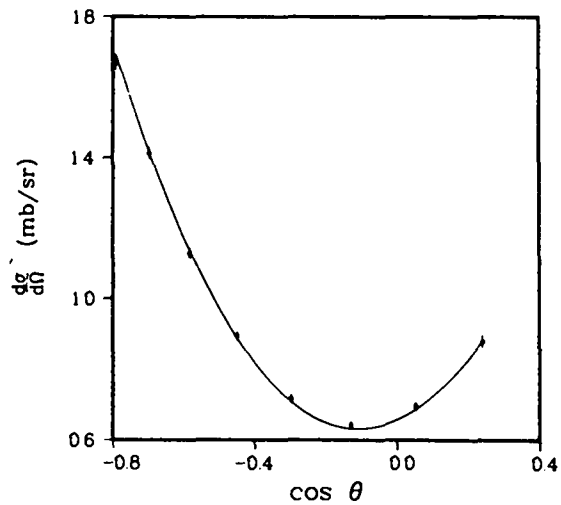

Fig. 21. Angular distribution of $\pi^- p \rightarrow \pi^- p$ at 229 MeV. The points have been normalized to agree as well as possible with the curve. The curve represents the interpolation of SCATPI.

Table X. Results from $\pi^- p \rightarrow \pi^- p$ at 254 MeV. Entries are the same as in Table VII.

θ_{LAB}	cos θ	$\frac{d\sigma}{d\Omega}$	P_{Beam}	ΔP	χ^2/ν
70	0.037	0.605 ± 0.012	368.14 ± 0.09	6.35 ± 0.16	1.75
80	-0.144	0.543 ± 0.009	367.68 ± 0.10	6.40 ± 0.15	2.15
90	-0.311	0.592 ± 0.010	367.91 ± 0.09	6.40 ± 0.15	1.87
100	-0.461	0.720 ± 0.010	367.72 ± 0.04	6.27 ± 0.13	1.93
110	-0.592	0.922 ± 0.12	367.88 ± 0.09	6.26 ± 0.12	2.29
120	-0.704	1.104 ± 0.014	368.14 ± 0.09	6.07 ± 0.11	2.11
130	-0.797	1.379 ± 0.016	367.92 ± 0.09	6.00 ± 0.09	2.48

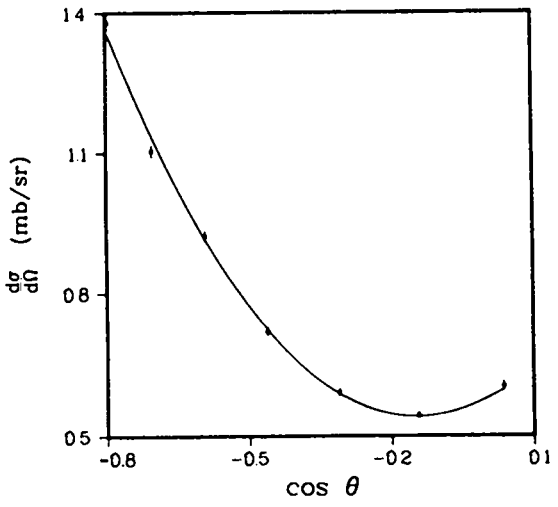

Fig. 22. Angular distribution of $\pi^- p \rightarrow \pi^- p$ at 254 MeV. The points have been normalized to agree as well as possible with the curve. The curve represents the interpolation of SCATPI.

Table XI. Results from $\pi^- p \to \pi^- p$ at 279 MeV. Entries are the same as in Table VII.

θ_{LAB}	cos θ	$\frac{d\sigma}{d\Omega}$	P_{Beam}	ΔP	χ^2/ν
80	-0.158	0.501 ± 0.010	394.75 ± 0.10	7.13 ± 0.19	2.82
90	-0.324	0.509 ± 0.008	394.81 ± 0.10	7.05 ± 0.15	2.10
100	-0.472	0.608 ± 0.008	394.74 ± 0.10	6.76 ± 0.14	2.24
110	-0.601	0.747 ± 0.009	394.76 ± 0.09	6.62 ± 0.12	1.85
120	-0.711	0.914 ± 0.010	394.86 ± 0.09	6.68 ± 0.10	1.10
130	-0.802	1.084 ± 0.011	394.87 ± 0.08	6.56 ± 0.09	3.14
90	-0.324	0.513 ± 0.012	394.75 ± 0.15	7.18 ± 0.24	0.82
110	-0.601	0.769 ± 0.013	394.77 ± 0.13	6.88 ± 0.17	2.13
130	-0.802	1.059 ± 0.015	394.82 ± 0.11	6.47 ± 0.12	3.11

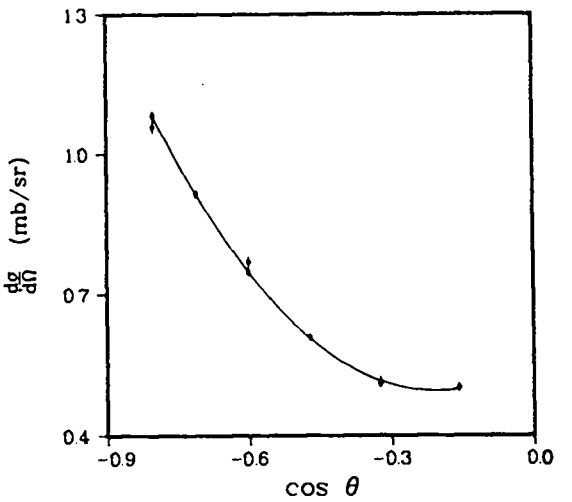

Fig. 23. Angular distribution of $\pi^- p \to \pi^- p$ at 279 MeV. The points have been normalized to agree as well as possible with the curve. The curve represents the interpolation of SCATPI.

Table XII. Results from $\pi^- p \to \pi^- p$ at 292 MeV. Entries are the same as in Table VII.

θ_{LAB}	cos θ	$\frac{d\sigma}{d\Omega}$	P_{Beam}	ΔP	χ^2/ν
		(a) First beam			
100	-0.478	0.572 ± 0.009	408.17 ± 0.13	7.52 ± 0.18	0.68
110	-0.606	0.672 ± 0.009	407.83 ± 0.12	7.89 ± 0.15	2.11
120	-0.714	0.825 ± 0.010	408.23 ± 0.11	7.19 ± 0.12	1.14
130	-0.804	0.985 ± 0.011	408.35 ± 0.10	6.90 ± 0.11	1.03
		(b) Second beam			
100	-0.478	0.568 ± 0.010	408.43 ± 0.13	7.05 ± 0.20	1.84
110	-0.606	0.679 ± 0.010	407.80 ± 0.13	6.80 ± 0.15	1.77
120	-0.714	0.813 ± 0.011	408.30 ± 0.12	6.76 ± 0.19	2.44
130	-0.804	0.998 ± 0.013	407.90 ± 0.11	6.81 ± 0.12	1.57

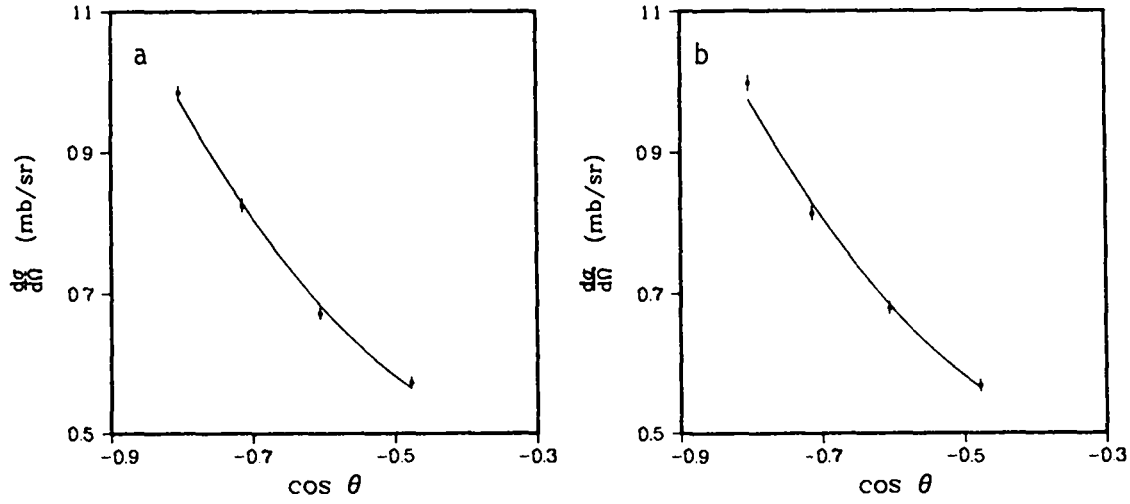

Fig. 24. Angular distribution of $\pi^- p \to \pi^- p$ at 292 MeV. a) first beam, b) second beam. The points have been normalized to agree as well as possible with the curve. The curve represents the interpolation of SCATPI.

Table XIII. Results from $\pi^- p \rightarrow \pi^- p$ spectra at 330 MeV. Entries are the same as in Table VII.

θ_{LAB}	cos θ	$\frac{d\sigma}{d\Omega}$	P_{Beam}	ΔP	χ^2/ν
90	-0.349	0.423 ± 0.008	449.72 ± 0.13	7.77 ± 0.25	2.18
100	-0.494	0.467 ± 0.007	448.98 ± 0.13	8.03 ± 0.20	1.04
110	-0.619	0.564 ± 0.008	448.33 ± 0.13	7.93 ± 0.18	0.99
120	-0.725	0.671 ± 0.009	449.18 ± 0.13	7.66 ± 0.16	2.66
130	-0.811	0.803 ± 0.010	449.38 ± 0.12	7.54 ± 0.14	2.06
90	-0.349	0.422 ± 0.011	449.44 ± 0.18	8.16 ± 0.34	2.60
110	-0.619	0.553 ± 0.008	448.54 ± 0.14	7.71 ± 0.20	1.70
130	-0.811	0.802 ± 0.010	448.73 ± 0.12	7.64 ± 0.14	2.78

Table XIV. Interpolated cross sections for $\pi^- p \rightarrow \pi^- p$ at 330 MeV. These cross sections were used to determine the normalization of the cross sections reported in Table XIII. Units are mb/sr.

cos θ	$\frac{d\sigma}{d\Omega}$
-0.348	0.436 ± 0.020
-0.494	0.471 ± 0.019
-0.619	0.557 ± 0.022
-0.725	0.679 ± 0.030
-0.812	0.775 ± 0.035

Table XV. Results from $\pi^- p \rightarrow \pi^- p$ spectra at 356 MeV. Entries are the same as in Table VII.

θ_{LAB}	cos θ	$\frac{d\sigma}{d\Omega}$	P_{Beam}	ΔP	χ^2/ν
90	-0.360	0.405 ± 0.008	476.11 ± 0.16	8.38 ± 0.32	1.19
100	-0.503	0.435 ± 0.008	475.61 ± 0.17	8.38 ± 0.28	1.26
110	-0.627	0.522 ± 0.007	475.25 ± 0.14	8.35 ± 0.20	2.49
120	-0.731	0.637 ± 0.008	474.94 ± 0.11	7.85 ± 0.13	3.41
130	-0.816	0.763 ± 0.008	475.25 ± 0.12	7.92 ± 0.16	2.31

Table XVI. Interpolated cross section for $\pi^- p \rightarrow \pi^- p$ at 356 MeV. These cross sections were used to determine the normalization of the cross sections reported in Table XV. Units are mb/sr.

cos θ	$\frac{d\sigma}{d\Omega}$
-0.360	0.400 ± 0.016
-0.503	0.443 ± 0.018
-0.627	0.527 ± 0.021
-0.731	0.642 ± 0.026
-0.816	0.740 ± 0.035

Table XVII. Results from the study of $\pi^- p \rightarrow \pi^- p$. T_{Beam} is the kinetic energy of the incident beam in MeV, T is the normalization factor in (mb/sr) (monitor counts/π), P_{Beam} is the mean momentum of the incident beam in MeV/c, and ΔP is the root mean square variation in the incident momentum in MeV/c. The quoted uncertainties in P_{Beam} and ΔP are the root mean square deviations of the individual values at each energy.

T_{Beam}		T	P_{Beam}	ΔP
229		25.59±0.29	341.00±0.20	5.85±0.19
254		23.54±0.38	367.92±0.18	6.20±0.16
279		24.68±0.33	394.80±0.05	6.70±0.26
292	a	23.10±0.31	403.18±0.23	7.16±0.43
292	b	23.82±0.42	408.09±0.30	6.82±0.13
330		21.68±1.07	449.02±0.48	7.73±0.21
356		22.45±0.51	475.33±0.45	8.04±0.27

Table XVIII. Incident momentum distributions corrected for loss of energy in the target. Units are MeV/c.

P	ΔP
340.64	5.85
367.57	6.20
394.46	6.70
407.83	7.17
407.75	6.83
448.69	7.74
474.99	8.04

CHAPTER IV

INTERPOLATON OF THE $\pi^{\pm}p$ ELASTIC DIFFERENTIAL CROSS SECTIONS

This chapter describes the interpolation of the differential cross section for πp elastic scattering. Below 300 MeV, energy independent phase shifts were fitted to plausible functions of momentum, and the interpolated phase shifts were used to calculate the differential cross section. A less elegant method of interpolation was necessitated at 330 MeV and 356 MeV by the limited accuracy and sparsity of the data above 300 MeV. A graphical method provided the cross sections at these two energies.

Interpolation Below 300 MeV

Below 300 MeV, the elastic differential cross section was interpolated in SCATPI.[10] The subroutine was derived from the phase shift analysis of Carter, Bugg and Carter[11] which in turn had been based primarily on the differential cross sections for $\pi^{\pm}p$ elastic scattering measured by Bussey, Carter, Dance, Bugg, Carter and Smith,[12] but also on total cross sections, integrated charge exchange cross sections and polarization measurements.[13-16] Their analysis provided eleven sets of phase shifts for the $\pi^{+}p$ system between 95 MeV and 310 MeV, and nine for the $\pi^{-}p$ system between 89 MeV and 292 MeV. These were fitted by least squares to plausible functions of momentum which had as few free parameters as would permit a reasonable χ^2/ν. Thus the phase shifts interpolated with these functions should be physically reasonable.

As a minimum test of its accuracy, the predictions of SCATPI have

been compared to the measurements from which it was derived and have typically differed by the following amounts:

	π^+p	π^-p
differential elastic cross section	2%	2½% below 260 MeV
	2%	4% above 260 MeV
total cross section	½%	1%
integrated charge exchange cross sections	---	1%

These differences are generally reasonable considering the uncertainties in the measurements, except for the π^-p elastic differential cross section at higher energies where the phase shift analysis seems in some difficulty. Predictions for the polarization parameter also agree reasonably with the measurements. Predictions of SCATPI have also been compared to measurements that have become available since the subroutine was completed, and have agreed with similar precision.

SCATPI is based upon a set of phase shifts that are interpolated from the analysis of Carter, Bugg and Carter, and necessarily follows the same scheme employed by those authors in relating the phase shifts to the differential cross section. The scattering amplitude in the center of momentum system is

$$F = f(\theta,k) + g(\theta,k)\ \hat{n}\cdot\vec{\sigma}.$$

Here $\vec{\sigma}$ are the usual Pauli matrices, θ is the angle between the initial and final wave vectors, $\vec{k}_i$ and $\vec{k}_f$, respectively, $k = |\vec{k}_i|$ is the initial wave number, and $\hat{n}$ is a unit vector orthogonal to both $\vec{k}_i$ and $\vec{k}_f$, $\hat{n} = \vec{k}_f \times \vec{k}_i / |\vec{k}_f \times \vec{k}_i|$. The functions $f(\theta,k)$ and $g(\theta,k)$ are commonly called the spin-nonflip and spin-flip scattering amplitudes, respectively. If the spin of the final state is not observed and the initial

state is unpolarized, the differential cross section is

$$\frac{d\sigma}{d\Omega} = |f(\theta,k)|^2 + |g(\theta,k)|^2.$$

Since the Coulomb interaction with its long range cannot be ignored when both the pion and nucleon are charged, many terms must be kept in a partial wave expansion to adequately represent the resulting scattering amplitude; however, only a few contain significant contribution from the strong interaction. This difficulty can be avoided by separating from each partial wave an amount equal to the partial wave for pure Coulomb scattering and by summing these pieces to the pseudo closed form discussed below. The scattering amplitudes are then written as

$$f(\theta,k) = f_c(\theta,k) + f_N(\theta,k)$$
$$g(\theta,k) = g_c(\theta,k) = g_N(\theta,k) ,$$

where f_c and g_c are the Coulomb amplitudes. f_N and g_N are the remainders of the scattering amplitudes, which are largely due to the strong interaction and should contain few partial waves.

The Coulomb amplitudes and phase shifts used in SCATPI are

$$f_c^{\pm} = \mp (1-t)^{-4} \frac{\alpha}{1-\cos\theta} \{ \frac{1}{k\beta} \exp \left(\mp \frac{i\alpha}{\beta} \ln \frac{1-\cos\theta}{2}\right)$$
$$+ \frac{1}{2(E_\pi+E_p)} \left(\frac{E_\pi+E_p-M_N}{E_p-M_N} + \frac{E_\pi+E_p+M_p}{E_p+M_p} \cos\theta - (\mu_p-1) \frac{E_p}{M_p} (1-\cos\theta) \right.$$
$$\left. - (\mu_p-1) \frac{E_p-M_p}{2M_p} \sin^2\theta \right) - \frac{1}{k\beta} \}$$

$$g_c^{\pm} = \pm (1-t)^{-4} \frac{\alpha \sin\theta}{2(E_\pi+E_p)(1-\cos\theta)} \left(\frac{E_\pi+E_p+M_p}{E_p+M_p} + (\mu_p-1) \frac{2E_\pi+E_p+M_p}{2M_p} \right.$$
$$\left. + (\mu_p-1) \frac{E_p+M_p}{2M_p} \cos\theta \right)$$

$$\nu_1^{\pm} = \nu_0^{\pm} \pm \frac{\alpha}{\beta}\frac{1}{3\kappa}\{1-(1+\kappa)^{-3}\}$$

$$\nu_2^{\pm} = \nu_0^{\pm} \pm \frac{3\alpha}{2\beta}\frac{1}{3\kappa^2}\{2\kappa-1+(1+\kappa)^{-2}\}$$

$$\nu_3^{\pm} = \nu_1^{\pm} \pm \frac{5\alpha}{6\beta}\frac{1}{\kappa^3}\{4-3\kappa+2\kappa^2-(4+5\kappa)(1+\kappa)^{-2}\},$$

where f_c^+, g_c^+ and ν_ℓ^+ apply for like charges while f_c^-, g_c^- and ν_ℓ^- apply for opposite charges. f_c and g_c are constructed from the exact non-relativistic solution for point charges, an additive relativistic correction to first order in α,[17] the fine structure constant, and a multiplicative form factor $(1-t)^{-4}$, which describes the charge distributions.[11] The ν_ℓ are derived from f_c and g_c after deleting the magnetic moment terms and ignoring the spin-flip amplitude, both of which are good numerical approximations.[11] Here $t = \frac{1}{2}\kappa(1-\cos\theta)$ is the square of the momentum transfer, and $\kappa = (2\lambda\!\!\!^{-}_\rho k)^2$ with $\lambda\!\!\!^{-}_\rho = 0.2563$ fm the Compton wavelength of the ρ meson. E_π and E_p are the total energies of the pion and proton, respectively, in the center of momentum system, while M_p is the proton rest energy, all in units of $\hbar c$. μ_p is the proton magnetic moment in nuclear magnetons. βc is the laboratory velocity of the incident pion.

The amplitudes f_N and g_N can be expanded in partial wave series as

$$f_N(\theta,k) = \sum_{\ell=0}^{\infty} \exp(i\varepsilon\nu_\ell)\{(\ell+1)A_{\ell+}(k) + \ell A_{\ell-}(k)\} P_\ell^0(\cos\theta),$$

$$g_N(\theta,k) = \sum_{\ell=0}^{\infty} \exp(i\varepsilon\nu_\ell)\{A_{\ell+}(k) - A_{\ell-}(k)\} P_\ell^1(\cos\theta).$$

Here $\varepsilon = 2$ for elastic scattering and $\varepsilon = 1$ for charge exchange scattering, $A_{\ell\pm}$ are the partial wave amplitudes for total angular momentum

$j = \ell \pm \frac{1}{2}$, and P_ℓ^0 and P_ℓ^1 are the associated Legendre functions. Only a few terms contribute to these sums due to the short range of the strong interaction. For energies below about 300 MeV, Carter, Bugg and Carter find that only terms with $\ell \leq 3$ are important. For $\pi^{\pm}p$ elastic scattering, SCATPI calculates the differential cross section without Coulomb scattering by using f_N and g_N as the complete scattering amplitudes, or includes Coulomb scattering by adding f_C and g_C to these to obtain the complete scattering amplitudes.

The strong interaction between pions and nucleons, which have isospin 1 and $\frac{1}{2}$, respectively, is thought to depend only on the total isospin I, and not on orientation in its space. If this were the only coupling operative, states of total isospin would be eigenstates and scattering amplitudes for the several pion-nucleon charge states would be linear combinations of those amplitudes for $I = \frac{1}{2}$ and 3/2 times the appropriate products of Clebsch-Gordon coefficients. The electromagnetic interaction, however, conserves only I_3, not I, and thus perturbs this simple description. Some of the better understood charge dependent effects are explicitly isolated when the partial wave scattering amplitudes are written in the following form, which was used by Carter, Bugg and Carter.

$$A_{\ell\pm}(\pi^+p\to\pi^+p) = \frac{1}{2ik}\{\exp(2i(\delta_{3\ell\pm} + C_{3\ell\pm})) - 1\}$$

$$A_{\ell\pm}(\pi^-p\to\pi^-p) = \frac{1}{2ik}\{\frac{2}{3}\exp(2i(\delta_{1\ell\pm} - \frac{2}{3}C_{1\ell\pm})) + \frac{1}{3}\exp(2i(\delta_{3\ell\pm} - \frac{1}{3}C_{3\ell\pm})) - 1\} - \frac{4}{9k}C_{13\ell\pm}\exp(i(\delta_{1\ell\pm} + \delta_{3\ell\pm}))$$

Subscripts 1 and 3 refer to isospin ½ and 3/2, respectively. In a potential model, joint action of the Coulomb and strong interaction potentials creates charge dependent phase shifts given by $C_{1\ell\pm}$ and $C_{3\ell\pm}$.[18] It also adds charge dependent terms scaled by $C_{13\ell\pm}$ to the scattering amplitudes with $I_3 = \frac{1}{2}$, because total isospin is no longer conserved. The remainder of the phase shift δ is caused mostly by the strong interaction; however, it may still depend on the charge states in several ways. The elasticity, $\exp(-2\mathrm{Im}(\delta))$, reflects loss to other channels, which may well depend on the charge state. For the energies considered here, elasticities with I = 3/2 differ for π^+p and π^-p initial states because a γn final state is available for the π^-p initial state. The $\mathrm{Re}(\delta)$ may also depend on the charge state through electromagnetic effects which have not been explicitly isolated. Charge dependence in the location and width of resonances in the strong interaction would be an interesting example of such effects.

The phase shifts δ used in SCATPI are interpolated from those found in the energy independent analysis of Carter, Bugg and Carter, who use the formulation described above. Plausible functions of momentum that have been fitted to the eleven sets of phase shifts for π^+p and nine sets for π^-p generate estimates of the phase shifts for all energies between 100 MeV and 300 MeV. Proper selection of functions which automatically fulfill known theoretical constraints and contain as few unknown parameters as possible is crucial for efficient use of the experimental information and for physically reliable interpolation. Nearly all contributions to δ are expected to have short range since the pure Coulomb scattering amplitude has been explicitly isolated and

removed. To good approximation, therefore, δ will have the momentum dependence[19]

$$\tan \delta_\ell = k^{2\ell+1} V(k^2).$$

The interpolation functions must have this form. For the P_{33} phase shift, the function includes a polynomial term in addition to a modified Breit-Wigner resonance

$$\delta = k^3 \sum_{m=0}^{N} a_m k^{2m} + \arctan \frac{\Gamma_{e\ell}(k)}{2(E_r - E) - i\Gamma_{in}(k)} .$$

Here E is the total center of momentum energy, E_r is the rest energy of the resonance, and $\Gamma_{e\ell}$ and Γ_{in} are the elastic and inelastic widths of the resonance. The elastic width has the form given by Jackson[20]

$$\Gamma_{e\ell} = \Gamma_r \left(\frac{2E_r}{E_r+E}\right) \left(\frac{k}{k_r}\right)^3 \frac{1+(R\,k_r)^2}{1+(Rk)^2}$$

with k_r the wave number at resonance, and Γ_r and R constants. The inelastic width is approximated as constant for $\pi^- p$ and zero for $\pi^+ p$. The a_m are also constants. We wished to model the P_{11} inelasticity as arising through the N(1470) resonance although only the tail of this resonance is in the energy range of interest. Therefore, the function for the P_{11} phase shift also has this form, but with $R = 0$ in $\Gamma_{e\ell}$. Since the inelasticity is believed to be largely in the pion production channel, the inelastic width has the form

$$\Gamma_{in} = 0 \quad , \quad E < E_t,$$
$$= b\,(E-E_t)^2, \quad E \geq E_t,$$

with E_t the threshold for pion production and b a constant. For the re-

maining phase shifts, the functions have the form

$$\delta_\ell = k^{2\ell+1} \sum_{m=0}^{N} a_m k^{2m}.$$

In these equations the constants a_m carry the same subscripts as δ, so that, for instance $a_{m,3,1-}$ are associated with $\delta_{3,1-}$, the P_{31} phase shift. Each phase shift was fit to the appropriate form for several trial values of N. SCATPI interpolates δ_i, i indicating all of the subscripts, using the parameter values obtained with the smallest value of N_i for which a reasonable χ^2/ν was achieved. Tables XIX and XX list respectively the real and imaginary parts of the a_m while the resonance parameters are listed in Table XXI. Following Carter, Bugg and Carter, the imaginary parts of the phase shifts are zero for π^+p. Similarly, the real part of the P_{33} phase shift is also charge dependent. Since only the low energy tail of the N(1470) resonance lies in the energy range of interest, the width and rest energy were taken from the "Review of Particle Properties"[21] and not treated as free parameters. E_t was assigned the value 6.157 fm^{-1}. The S_{11} phase shift at 310 MeV precluded a reasonable solution for the $a_{m,1,0+}$, and therefore was ignored.

The calculation of C_1, C_3 and C_{13} involves five numerical integrations for each value of $\ell\pm$. For convenience, they are interpolated from the values used by Carter, Bugg and Carter. These quantities depend on the strong as well as the Coulomb interaction, and are important only in the first few partial waves. The forms used for their interpolation are

$$C_{3,1+} = C_{r3} \arctan\left(\frac{E-E_2}{\Gamma_1/2}\right)/\left\{\left(\frac{E-E_1}{\Gamma_1/2}\right)^2 + \frac{E_1-M_p-m_\pi}{E-M_p-m_\pi}\right\},$$

$$C_{13,1+} = C_0 + \frac{C_{r13}\,(\Gamma/2)}{(E-E_1)^2 + (\Gamma/2)^2}$$

Table XIX. The real part of the polynomial parameters for the phase shifts. The a_i are in units of degrees times fm to the appropriate power. $\delta_{1,3+}$ and $\delta_{3,3-}$, not listed, are zero.

Initial State	Spectroscopic Notation	$2I,\ell\pm$	$Re(a_0)$	$Re(a_1)$	$Re(a_2)$
	S_{11}	1,0+	9.5464	-	-
	P_{11}	1,1-	-6.1009	2.5928	-
	P_{13}	1,1+	-2.0870	0.4606	-
	D_{13}	1,2-	0.4706	-	-
	D_{15}	1,2+	0.7268	-0.4659	0.0925
	F_{15}	1,3-	0.0704	-0.0181	-
	S_{31}	3,0+	-6.4878	-7.5756	1.9960
	P_{31}	3,1-	-4.6544	1.0636	-
π^+p	P_{33}	3,1+	1.3270	-	-
π^-p	P_{33}	3,1+	-0.2806	-	-
	D_{33}	3,2-	0.2270	-0.1247	0.0172
	D_{35}	3,2+	-0.5524	0.3484	-0.0701
	F_{37}	3,3+	0.1334	-0.0466	-

Table XX. The imaginary part of the polynomial parameters for the phase shifts. Units of a_i are fm to the appropriate power. The parameters not listed are zero.

Initial State	Spectroscopic Notation	$2I,\ell\pm$	$Im(a_0)$	$Im(a_1)$	$Im(a_2)$
π^-p	S_{11}	1,0+	0.2789	0.1092	0.0148
π^-p	S_{11}	3,0+	0.0991	-0.0523	0.0136

Table XXI. Resonance parameters for P_{11} and P_{33} phase shifts.

Initial State	Spectroscopic Notation	$2I,\ell\pm$	E_r (fm^{-1})	Γ_r (fm^{-1})	R (fm)	Γ_{in} (fm^{-1})	E_t (fm^{-1})	b (fm)
π^-p	P_{11}	1,1-	7.4487[a]	1.2669[a]	0.0	-	6.1565[a]	0.4176
π^-p	P_{33}	3,1+	6.2467	0.6109	0.9201	0.0	-	-
π^-p	P_{33}	3,1+	6.2422	0.5789	1.2290	5.69x 10^{-3}	-	-

[a]These parameters were not varied in minimizing χ^2. E_r and Γ_r were taken from "Review of Particle Properties".[21]

and for the S-wave and remaining P-wave corrections

$$C = C_0 + C_1 k,$$

while the corrections for higher partial waves were ignored. Here m_π is the rest energy of the pion, E_1, E_2, Γ_1, C_r, C_0 and C_1 are constants. The form of the elastic width in the P_{11} resonance was used for Γ here for convenience. The parameter values for each correction were determined by fitting the appropriate form to the values used for that correction by Carter, Bugg and Carter, and are listed in Table XXII.

In Fig. 25 through 28 the predictions of SCATPI are compared with the measurements of the differential cross sections by Bussey et al., a subset of the data used in the phase shift analysis of Carter, Bugg and Carter. The agreement with the π^+p data is excellent, since the deviations are consistent with the accuracy of the measurements. The deviations of the predictions from the π^-p data below 260 MeV are also consistent with the accuracy of the measurements, but above 260 MeV, at the highest two energies, the deviations grow to 3-4%, larger than the supposed uncertainties in the measurements. This trend presumably stems from the difficulty encountered by Carter, Bugg and Carter with the determination of the $I = \frac{1}{2}$ phase shifts above the $\Delta(1232)$ resonance. Their difficulty may in part be due to the inconsistencies in the data which are suggested in Fig. 28.

Interpolation at 330 MeV and 356 MeV

The differential cross sections at 330 MeV and 356 MeV were interpolated in a graphical manner. The published measurements of the π^-p elastic cross sections above 300 MeV are sparse and plagued with system-

Table XXII. Parameters for C-quantities.

Partial Wave	$\ell\pm$	$C_{3,1+}$ $C_1(°)$	$\Gamma_1(fm^{-1})$	$E_1(fm^{-1})$	$E_2(fm^{-1})$
$P_{3/2}$	1+	1.0779	0.4970	0.6238	1.0547
Partial Wave	$\ell\pm$	$C_{13,1+}$ $C_0(°)$	$C_r(°)$	$\Gamma_r(fm^{-1})$	$E_r(fm^{-1})$
$P_{3/2}$	1+	-0.0607	-0.3401	-0.6848	-0.7315

Other C-Quantities

Partial Wave	$\ell\pm$	Quantity	$C_0(°)$	$C_1(°fm)$
$S_{1/2}$	0+	$C_{1,0+}$	-0.1284	0.0863
		$C_{13,0+}$	0.0185	0.0318
		$C_{3,0+}$	0.0887	0.0569
$P_{1/2}$	1-	$C_{1,1-}$	0.1316	-0.1091
		$C_{18,1-}$	-0.0393	--
		$C_{3,1-}$	-0.0282	0.0791
$P_{3/2}$	1+	$C_{1,1+}$	-0.0168	0.0434

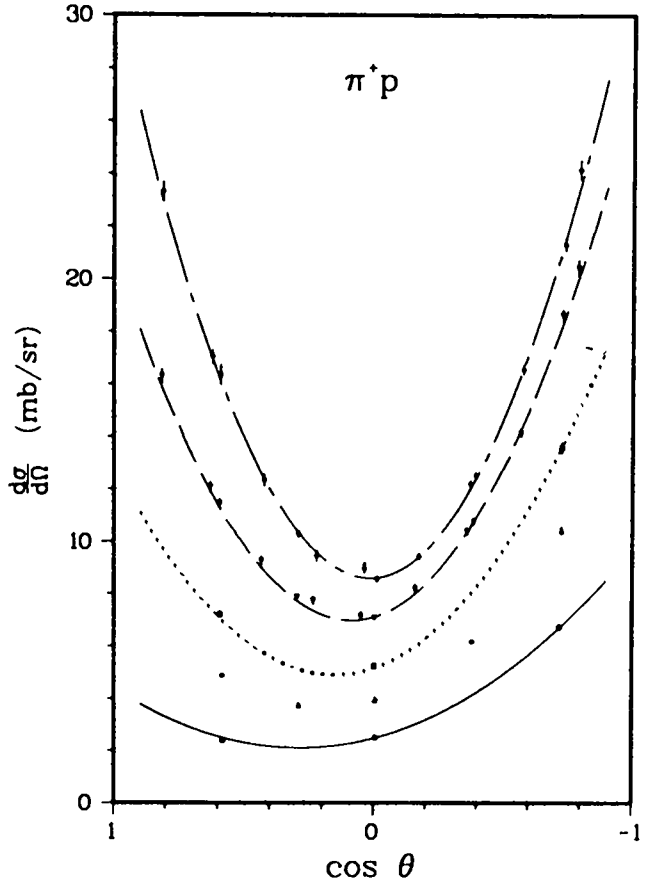

Fig. 25. Angular distributions of Bussey et al. for π^+p elastic scattering at lab. energies (0) 94.5, (Δ) 114.1, (▱) 124.8, (▽) 142.9 and (◇) 166.0 MeV. The curves show the predictions of SCATPI excluding Coulomb scattering.

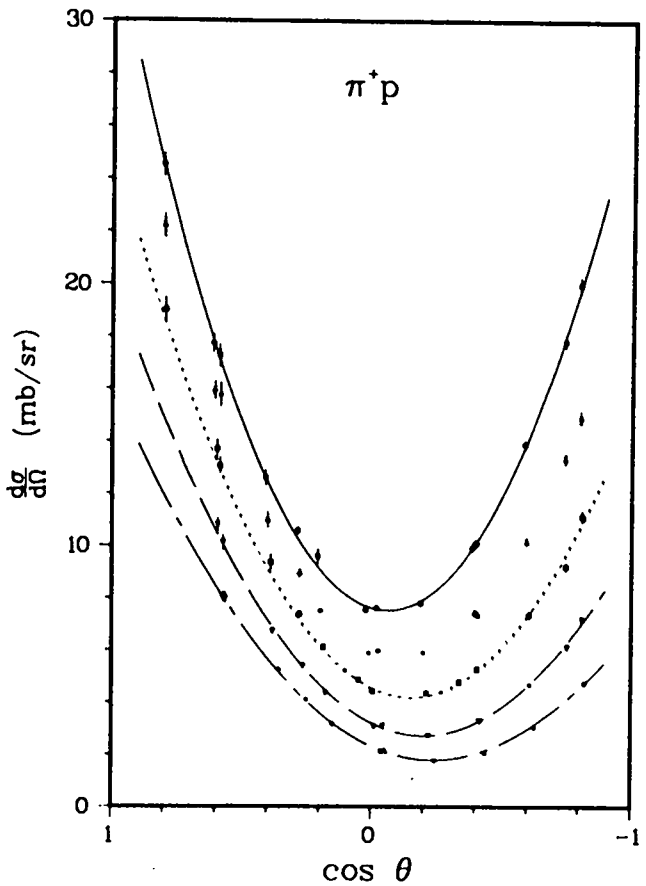

Fig. 26. Angular distributions of Bussey et al. for π^+p elastic scattering at lab. energies (0) 194.3, (Δ) 214.6, (⊔) 236.3, (▽) 263.7 and (◇) 291.4 MeV. The curves show the predictions of SCATPI excluding Coulomb scattering.

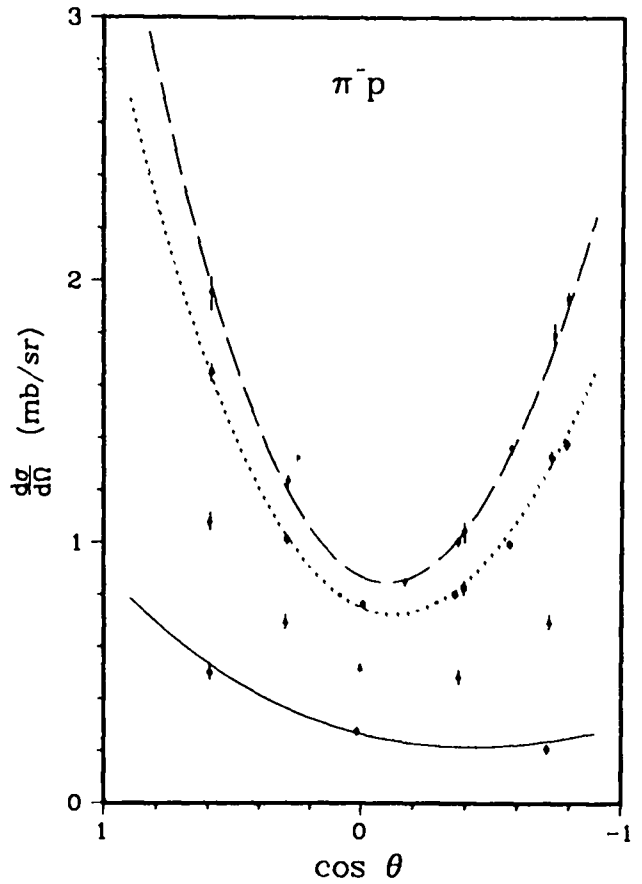

Fig. 27. Angular distributions of Bussey et al. for $\pi^- p$ elastic scattering at lab. energies (O) 88.5, (Δ) 119.3, (⊔) 144.2 and (∇) 161.9 MeV. The curves show the predictions of SCATPI excluding Coulomb scattering.

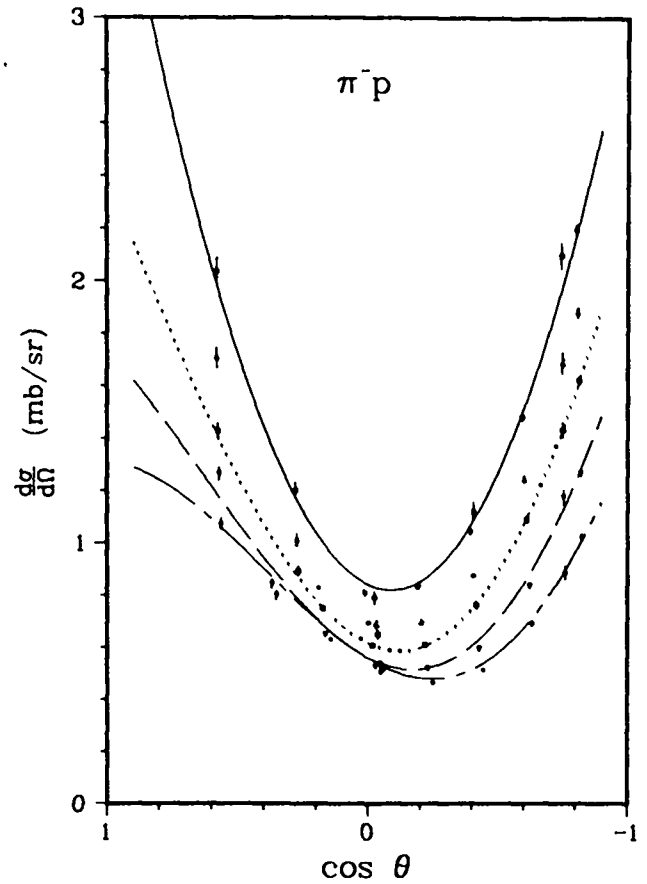

Fig. 28. Angular distributions of Bussey et al. for $\pi^- p$ elastic scattering at lab. energies (O) 191.9, (Δ) 219.6, (⊔) 237.9, (∇) 263.7 and (◇) 291.5 MeV. The curves show the predictions of SCATPI excluding Coulomb scattering.

atic errors. The most reliable appear to be those of Ogden et al.[22] at 370 MeV and 410 MeV, and Rugge and Vik[23] at 310 MeV. The cross sections at the two highest energies were interpolated from these measurements and the measurements of Bussey et al.[12] at 264 MeV and 292 MeV.

The data were plotted as a function of the cosine of the center of momentum scattering angle, $\cos\theta$, and a curve was sketched through each of the five sets of data. The cross sections and curve for 370 MeV are shown in Fig. 29 as an example. The cross sections for a particular $\cos\theta$ were interpolated at each energy using these curves. Uncertainties were assigned to the interpolated cross sections on the basis of the uncertainties of nearby measurements. The cross sections for $\cos\theta$ were plotted as a function of the incident kinetic energy. A curve was sketched through these points, bearing in mind that the form of the curve should change smoothly and systematically with $\cos\theta$. Fig. 30 shows the cross section as a function of incident kinetic energy for five values of $\cos\theta$ as an example. The required values of the differential cross section were interpolated from these curves. Rough errors were assigned on the basis of reasonable distortions in the curves.

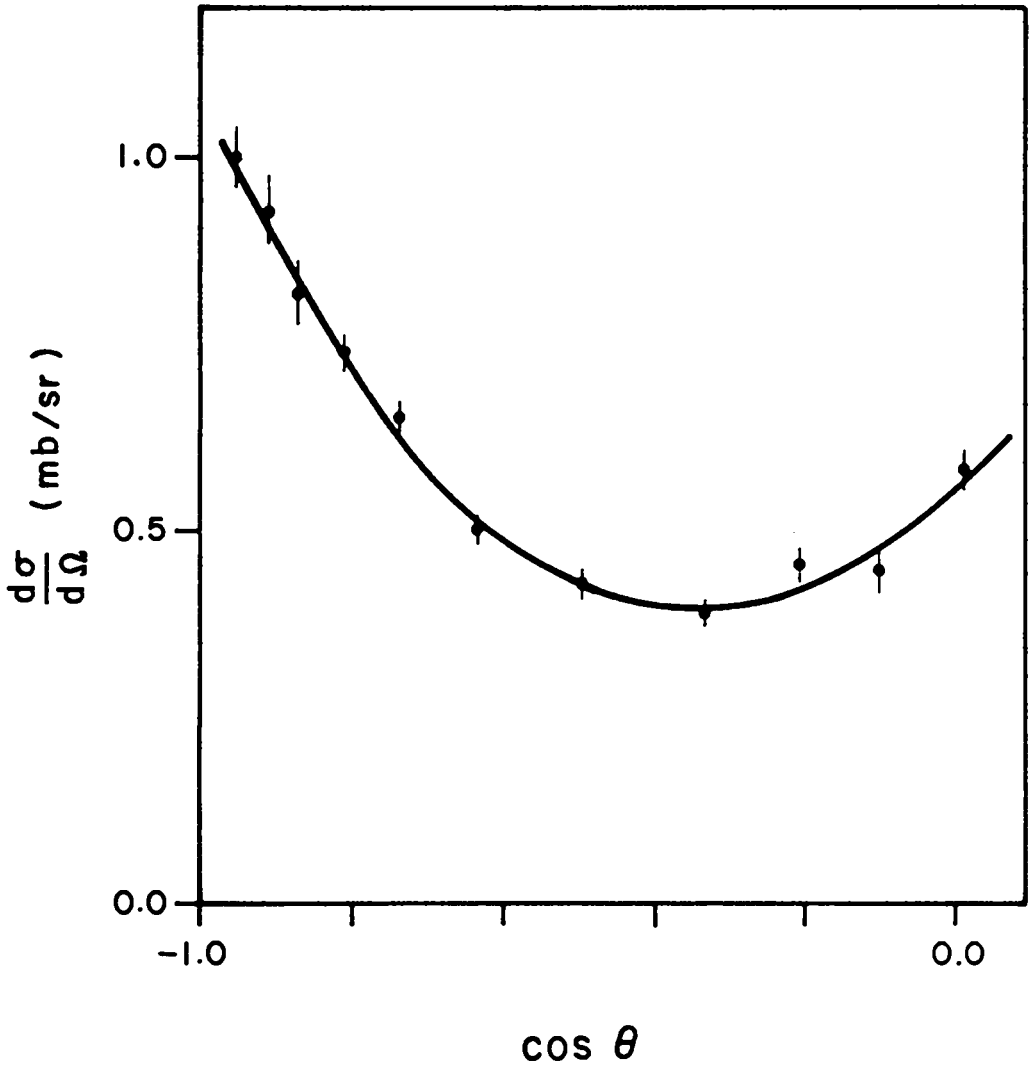

Fig. 29. Angular distribution of Ogden et al. at 370 MeV. The curve was sketched through the points to aid in interpolation.

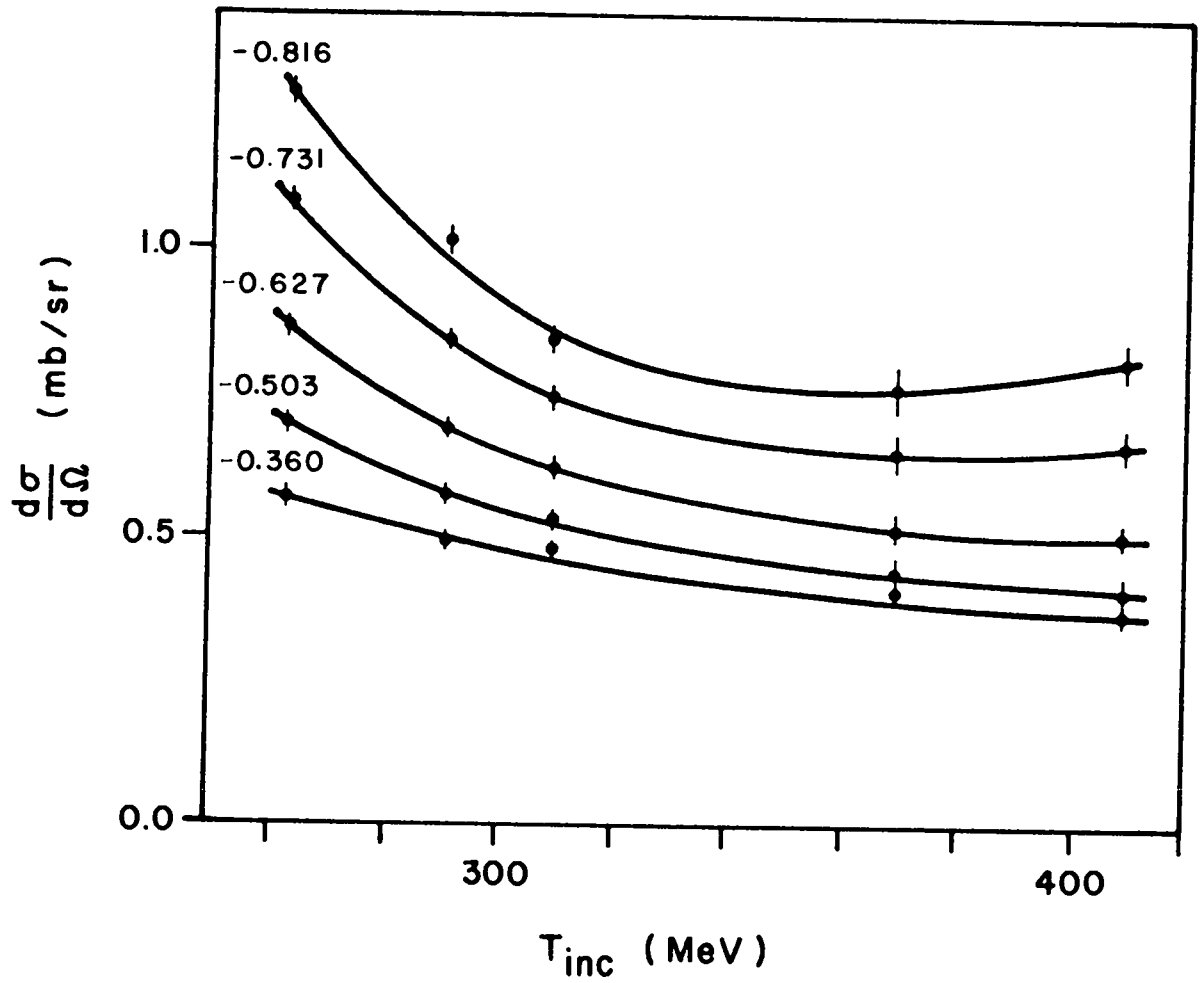

Fig. 30. Variation of the differential cross section with incident energy. The curves were sketched through the points to aid in interpolation.

CHAPTER V

ANALYSIS OF π^+ PRODUCTION

The doubly differential cross section $\frac{d^2\sigma}{d\Omega dT}$ of the π^+ meson produced in the reaction $\pi^-p \rightarrow \pi^+\pi^-n$ was measured at six incident energies between 229 MeV and 356 MeV. Plausible functions of the kinetic energy T and the cosine of the angle θ in the center of momentum frame were fitted to measurements at each energy. The functions were integrated to obtain the average square modulus of the matrix element and the net cross section for the reaction. The mean square moduli were extrapolated to the 172 MeV threshold to determine the symmetry breaking parameter of soft pion theory.

Doubly Differential Cross Sections

Event rate. Each measurement of $\frac{d^2\sigma}{d\Omega dT}$ consisted of two sets of data, one for the target flask filled with liquid hydrogen and one for the flask emptied. The doubly differential cross section was calculated from the difference in rates for the two sets. This procedure does not correct for the e^+ background which results from the sequence of single charge exchange in the target and flask, π^0 decay and pair production in the spectrometer. Since this rate also depends on the status of the target, it must be eliminated in another fashion. The detected e^+ are transported most of the way by the spectrometer, and hence are energetic and can be identified by a Cerenkov detector. The efficiency ε for identifying these e^+ is critical, particularly at 229 MeV where the charge exchange cross section is ~30 mb while the

π^+ production cross section is only ~60 μb. A recent measurement[3] of the π^+ production cross section at 230 MeV leaves no doubt that ε was significantly less than unity. Appendix C describes the evaluation of ε for most of the data from the measurements at 229 MeV and 230 MeV, with the result $\varepsilon = 0.828 \pm 0.038$. Also described is the determination of ε_e, the Cerenkov efficiency for the early data at 292 MeV, with the result $\varepsilon_e = 0.653 \pm 0.28$.

After correcting for the Cerenkov efficiency, the number of events in a channel was

$$N_i = n_{1i} - \frac{1-\varepsilon}{\varepsilon} n_{2i}$$

where n_{1i} is the number of events for which only channel i detected a particle and there was no coincident Cerenkov pulse, n_{2i} is the same except there was a coincident Cerenkov pulse. The n_{ji} possessed Poisson distributions since the events occurred randomly in time. The statistical uncertainty in the number of events was

$$\Delta N_i = \{ (n_{1i} + 1) + (\frac{1-\varepsilon}{\varepsilon})^2 (n_{2i} + 1)\}^{\frac{1}{2}}.$$

The net rate for π^+ events was

$$R_i = (N_i/M_\ell)_{full} - (N_i/M_\ell)_{empty}$$

with statistical uncertainty $\Delta R_i = \{(\Delta N_i/M_\ell)^2_{full} + (\Delta N_i/M_\ell)^2_{empty}\}^{\frac{1}{2}}$, where the subscripts full and empty refer to the target status. Here, as before, M_ℓ is either the number of counts in the scattering monitor during live time, or, for angles forwards of 40^o in the laboratory, the number of counts corrected for the reduction in the effectiveness of the scattering monitor due to the π^- beam intercepting the spectrometer structure. M_ℓ was sufficiently large ($>10^4$) that its uncertainty con-

tributed negligibly to ΔR_i.

Matrix element. Due to conservation of energy there was a maximum momentum with which the π^+(or π^- or n) could exit the target. Near this maximum the rate falls rapidly, going to zero at the maximum momentum. Here averaging the laboratory rates R_i becomes less meaningful. The question was further complicated by the 4% width of the incident momentum distribution, since the maximum outgoing momentum depends on the total energy of the system.

This problem was resolved by considering the center of momentum cross section $\frac{d^2\sigma}{d\Omega dT}$ in terms of the squared modulus of a matrix element M weighted by the density of phase space and averaged over the unobserved kinematic variables

$$\frac{d^2\sigma}{d\Omega dT} = \langle |M|^2 \rangle \frac{d^2\sigma_0}{d\Omega dT}$$

with

$$\frac{d^2\sigma_0}{d\Omega dT} = \frac{1}{4\pi} \frac{\lambda\!\!\!^{-2}}{4} \left(\frac{G^2}{4\pi}\right)^3 \left(\frac{g_v}{g_a}\right)^4 \frac{m_\pi^2}{M_N^4} \frac{Q}{S} (T_{2max} - T_{2min}).$$

Here $2\pi\lambda\!\!\!^{-}$ is the Compton wavelength of the charged pion, G is the pion-nucleon strong coupling constant, g_v and g_a are the vector and axial vector coupling constants, and M_N is the nucleon mass. Q is the incident momentum in the center of momentum system, S is the root of the invariant mass squared, and T_2 is the kinetic energy of either of the undetected particles in the center of momentum. The last factor was calculated as

$$T_{2max} - T_{2min} = \frac{2p \{ S (T_{max}-T) [2m_2m_3 + S (T_{max}-T)] \}^{\frac{1}{2}}}{(m_2+m_3)^2 + 2S (T_{max}-T)}$$

where p and T are the momentum and kinetic energy in the center of mo-

mentum, T_{max} is the maximum value of T, and m_2 and m_3 are the masses of the two undetected particles. σ_0 has been referred to as Q^2 × phase space because it includes a factor of Q^2 from the square modulus of the matrix element which is introduced by the P-wave nature of the initial state. σ_0 also includes flux factors and some constants to facilitate comparison with soft pion theory.

Both the mean square modulus and Q^2 × phase space depended on the total energy. Hence, the observed rate was an integral over $w(Q_{LAB})$, the distribution of momenta in the beam,

$$R_i = \frac{\eta_i P_C \delta}{E_i T} \int J_i \, \langle |M|^2 \rangle \, \frac{d^2\sigma_0}{d\Omega dT} \, w(Q_{LAB}) \, dQ_{LAB} \, .$$

Here η_i is the channel efficiency, $P_C\delta$ is the momentum acceptance of a channel, and T is the normalization factor. E_i is the decay correction

$$E_i = \exp\{\Lambda m_\pi/(\tau p_i)\}$$

with Λ the mean path length to the focal plane, m_π and τ the rest mass and lifetime, respectively, of the charged pion, and p_i the momenta of particles detected in the i^{th} channel. J_i is the Jacobian of the transformation

$$J_i = \frac{\partial(T, \cos\theta)}{\partial(P_{LAB}, \cos\theta_{LAB})} = (p_i^2+m_\pi^2)^{-\frac{1}{2}} \, p_i/p$$

with p the momentum p_i transformed to the center of momentum frame. The distribution w was approximated as Gaussian, and the integration was carried out from two standard deviations below the mean to two standard deviations above the mean. w was normalized such that

$$\int w(x) \, dx = 1$$

for the same limits of integration. The square modulus of the matrix element weighted and averaged over the unobserved kinematic variables

and the distribution of the incident momenta was determined from the rate

$$(<|M|^2>_{BEAM})_i = \frac{TE_iR_i}{\eta_i P_c \delta}\{ \int J_i \frac{d^2\sigma_0}{d\Omega dT} w(Q_{LAB})\, dQ_{LAB} \}^{-1},$$

with $\Delta M_i = (<|M|^2>_{BEAM})_i\ (\Delta R_i/R_i)$ the statistical uncertainty. Here, as above, $\frac{d^2\sigma_0}{d\Omega dT}$ depends on i as well as Q_{LAB} through the variables T and cosθ. The mean square modulus is more slowly varying than the cross section near threshold. The estimates from the different channels are averaged to obtain a single estimate for the measurement

$$<|M|^2> = \sum_i \Delta_{Mi}^{-2}\ (<|M|^2>_{BEAM})_i\ /\ \{ \sum_j \Delta_{Mj}^{-2} \}$$

with

$$\Delta_M = \{ \sum_j \Delta_{Mj}^{-2} \}^{-\frac{1}{2}}$$

the statistical uncertainty.

Doubly differential cross section. The incident and detected pion momenta associated with the measurement were the mean values of the pions contributing to the measurement. In the approximation that $<|M|^2>$ is slowly varying as a function of the incident and detected momenta, this implies

$$<Q_{LAB}> = \sum_i \eta_i\ E_i^{-1} \int Q_{LAB}\ J_i \frac{d^2\sigma_0}{d\Omega dT} w(Q_{LAB})\, dQ_{LAB} \times \{ \sum_j \eta_j\ E_j^{-1} \int J_j \frac{d^2\sigma_0}{d\Omega dT} w(Q_{LAB})\, dQ_{LAB} \}^{-1}$$

and

$$<P_{LAB}> = \sum_i \eta_i\ E_i^{-1}\ p_i \int J_i \frac{d^2\sigma_0}{d\Omega dT} w(Q_{LAB})\, dQ_{LAB} \times \{ \sum_j \eta_j\ E_j^{-1} \int J_j \frac{d^2\sigma_0}{d\Omega dT} w(Q_{LAB})\, dQ_{LAB} \}^{-1}$$

where $<|M|^2>$ has been factored from each of the integrals, and $<Q_{LAB}>$ and $<P_{LAB}>$ are the mean incident and detected momentum, respectively. The cross section in the center of momentum frame was calculated from

$< |M|^2 >$ with $\frac{d^2\sigma_0}{d\Omega dT}$ evaluated for the mean momenta.

Tables XXIII through XXVII present T, cosθ, $\frac{d^2\sigma_0}{d\Omega dT}$, $< |M|^2 >$ and the percent uncertainties in $< |M|^2 >$ for the measurements at the higher five incident energies. These percent uncertainties apply to the doubly differential cross section as well. The uncertainties $\Delta_{M\varepsilon}$ are the deviations in $< |M|^2 >$ produced by the substitution of $\varepsilon \pm \Delta\varepsilon$ for ε. Presumably, these are highly correlated from measurement to measurement and from energy to energy. The values for $< |M|^2 >$ and their statistical uncertainties are also shown in Fig. 31 through 35. The solid and dashed lines represent respectively the laboratory momentum of 70 MeV/c and the laboratory angle of 32^0. The coverage of (T, cosθ) space varied from about 65% at 254 MeV to 85% at 356 MeV.

Integrated Cross Sections

At each energy the values of $< |M|^2 >$ were fitted to the function

$$f(T,\cos\theta) = C(T) \{ \zeta_1 + \zeta_2\cos\theta + \zeta_3(T_{max}-T)\cos\theta + \zeta_4 T^2 \}^2$$

with ζ_i the adjustable parameters. C(T) is a correction for enhancement of the cross section from Coulomb attraction between the two pions in the final state averaged over the unobserved kinematic variables. It was calculated by a Monte Carlo computer program as

$$C(T) = \langle \exp(\frac{\pi\alpha}{\beta}) \rangle,$$

where βc is the relative velocity of the two pions and α is the fine-structure constant. The exponential was averaged over β for T in sixteen bins between 0 and T_{max}. These values were slowly varying between 1.03 and 1.05. C(T) was obtained by linear interpolation. The parameters ζ_i were varied to minimize χ^2

Table XXIII. Doubly differential cross sections at 254 MeV. T and θ are the kinetic energy and angle of the produced π^+. Δ_1 is the percent statistical uncertainty and $\Delta_2 = \{\frac{d}{d\varepsilon} \langle|M|^2\rangle\} \delta\varepsilon/|M|^2$ is the sensitivity to the Cerenkov efficiency ε. T is in MeV, $(d^2\sigma/d\Omega dT)$ is in $\mu b/(sr\text{-}MeV)$, and both Δ_1 and Δ_2 are in %.

T	cosθ	$\frac{d^2\sigma}{d\Omega dT}$	$\langle\|M\|^2\rangle$	Δ_1	Δ_2
36.0	-0.751	0.303	8.19	30.1	0.9
46.2	-0.751	0.148	5.23	38.6	11.1
25.8	-0.351	0.344	8.86	18.7	8.4
36.0	-0.352	0.332	8.98	13.3	5.8
44.5	-0.354	0.195	6.44	18.9	5.8
15.3	-0.198	0.227	6.56	32.6	2.7
24.2	-0.007	0.361	9.37	11.8	8.0
34.3	-0.005	0.371	9.84	9.9	5.8
43.8	-0.009	0.189	6.08	15.4	8.2
15.4	0.149	0.333	9.59	14.9	16.2
23.7	0.294	0.296	7.68	14.2	14.4
34.3	0.294	0.355	9.41	11.3	7.0
43.5	0.291	0.324	10.28	8.7	6.3
8.6	0.349	0.357	12.87	15.1	2.1
15.4	0.549	0.283	8.17	14.3	22.3
23.6	0.644	0.353	9.16	10.9	11.6
33.6	0.644	0.356	9.36	9.0	9.4
42.5	0.648	0.269	8.25	10.1	10.9

Table XXIV. Doubly differential cross sections at 279 MeV. Entries are the same as in Table XXIII.

T	cosθ	$\frac{d^2\sigma}{d\Omega dT}$	$\langle\|M\|^2\rangle$	Δ_1	Δ_2
47.0	-0.850	0.391	7.71	22.9	4.1
60.3	-0.851	0.292	7.77	21.7	3.6
33.6	-0.790	0.476	8.91	29.0	0.3
34.3	-0.502	0.618	11.55	11.1	1.6
45.9	-0.527	0.589	11.48	10.8	0.8
57.7	-0.526	0.362	8.79	13.5	1.4
20.2	-0.451	0.395	8.30	30.6	0.7
15.8	-0.102	0.415	9.51	16.5	0.8
29.0	-0.096	0.534	10.20	11.6	2.0
42.7	-0.106	0.545	10.36	9.5	1.2
55.8	-0.108	0.473	10.86	9.9	0.8
15.7	0.248	0.425	9.76	14.0	5.6
29.1	0.291	0.655	12.49	10.1	1.9
42.2	0.299	0.651	12.34	8.1	1.2
55.4	0.296	0.481	10.90	8.5	1.5
6.7	0.349	0.218	7.17	27.5	2.9
15.6	0.548	0.410	9.42	16.3	6.7
29.0	0.649	0.553	10.55	8.4	3.4
41.8	0.649	0.661	12.50	6.8	1.8
52.7	0.688	0.508	10.85	7.3	2.1

Table XXV. Doubly differential cross sections at 292 MeV. Entries are the same as in Table XXIII.

T	cosθ	$\frac{d^2\sigma}{d\Omega dT}$	$\langle\|M\|^2\rangle$	Δ_1	Δ_2
40.5	-0.847	0.562	9.16	24.5	5.7[a]
56.7	-0.848	0.605	10.99	14.6	18.1[a]
67.9	-0.851	0.289	6.98	25.2	24.0[a]
40.7	-0.543	0.783	12.78	11.4	3.0[a]
57.0	-0.544	0.601	10.95	10.0	9.0[a]
65.2	-0.556	0.423	9.24	11.6	13.5[a]
24.4	-0.439	0.657	11.77	14.5	13.7[a]
24.6	-0.138	0.609	10.90	12.3	22.8[a]
40.9	-0.138	0.764	12.47	9.2	10.0[a]
57.5	-0.146	0.477	8.75	11.0	9.6[a]
67.5	-0.153	0.403	9.48	9.3	9.6[a]
25.0	0.256	0.817	14.55	8.6	20.7[a]
41.1	0.264	0.813	13.26	7.4	11.0[a]
57.7	0.254	0.562	10.33	6.6	12.4[a]
67.5	0.244	0.366	8.91	7.9	1.6
8.4	0.369	0.394	10.84	19.8	45.0[a]
25.1	0.559	0.737	13.10	8.2	2.1
41.1	0.654	0.685	11.18	7.9	1.5
58.0	0.655	0.558	10.34	8.7	1.7
67.2	0.649	0.352	8.19	9.5	2.2

[a]Represents the sensitivity to ε_e rather than ε. The sensitivity to ε is smaller by a factor of 10.

Table XXVI. Doubly differential cross sections at 330 MeV. Entries are the same as in Table XXIII.

T	cosθ	$\frac{d^2\sigma}{d\Omega dT}$	$\langle\|M\|^2\rangle$	Δ_1	Δ_2
48.7	-0.851	0.995	11.57	10.1	0.2
68.2	-0.851	1.013	12.30	14.0	0.5
87.4	-0.851	0.713	11.89	14.2	0.5
25.5	-0.496	0.848	11.71	11.1	0.1
45.5	-0.506	1.205	14.10	12.3	0.4
67.7	-0.501	1.053	12.52	10.4	0.3
84.4	-0.535	0.701	10.74	11.8	0.1
27.5	-0.121	1.265	16.98	9.9	0.7
46.6	-0.120	1.174	13.68	9.5	0.4
65.8	-0.120	1.258	15.03	7.4	0.3
83.1	-0.122	0.739	10.97	9.3	0.2
9.7	-0.054	0.573	11.98	12.7	0.5
27.2	0.245	1.320	17.79	7.3	0.7
46.6	0.270	1.437	16.75	6.2	0.4
65.3	0.276	1.215	14.48	5.6	0.4
82.7	0.276	0.695	10.21	7.5	0.4
9.7	0.347	0.870	18.17	10.9	0.2
25.7	0.553	1.257	17.29	7.6	1.3
45.0	0.647	1.318	15.45	5.4	0.8
64.3	0.650	1.144	13.56	6.6	0.8
82.7	0.653	0.685	10.06	6.3	0.7

Table XXVII. Doubly differential cross sections at 356 MeV. Entries are the same as in Table XXIII.

T	cos θ	$\frac{d^2\sigma}{d\Omega dT}$	$\langle\|M\|^2\rangle$	Δ_1	Δ_2
56.0	-0.851	1.389	13.43	11.2	0.0
78.1	-0.851	1.425	14.38	10.2	0.3
100.1	-0.851	0.807	11.23	12.2	0.1
33.6	-0.552	1.277	14.03	11.5	0.1
55.8	-0.552	1.691	16.36	8.5	0.3
76.5	-0.532	1.353	13.53	7.7	0.1
97.6	-0.523	0.857	11.18	8.6	0.1
11.2	-0.152	0.853	14.93	14.7	0.2
32.3	-0.153	1.654	18.41	7.5	0.4
52.4	-0.143	1.628	15.87	6.9	0.3
74.3	-0.134	1.531	15.14	5.9	0.1
94.0	-0.109	0.991	11.97	6.8	0.2
11.2	0.247	1.266	22.19	11.3	0.2
31.9	0.252	1.840	20.59	6.4	0.4
52.5	0.234	1.764	17.19	5.1	0.3
73.0	0.270	1.652	16.24	4.4	0.2
93.6	0.291	0.970	11.62	5.7	0.2
29.5	0.588	2.228	25.64	4.6	0.5
51.0	0.636	1.969	19.28	4.7	0.5
72.3	0.656	1.616	15.84	4.6	0.3
93.2	0.668	0.956	11.37	5.2	0.7

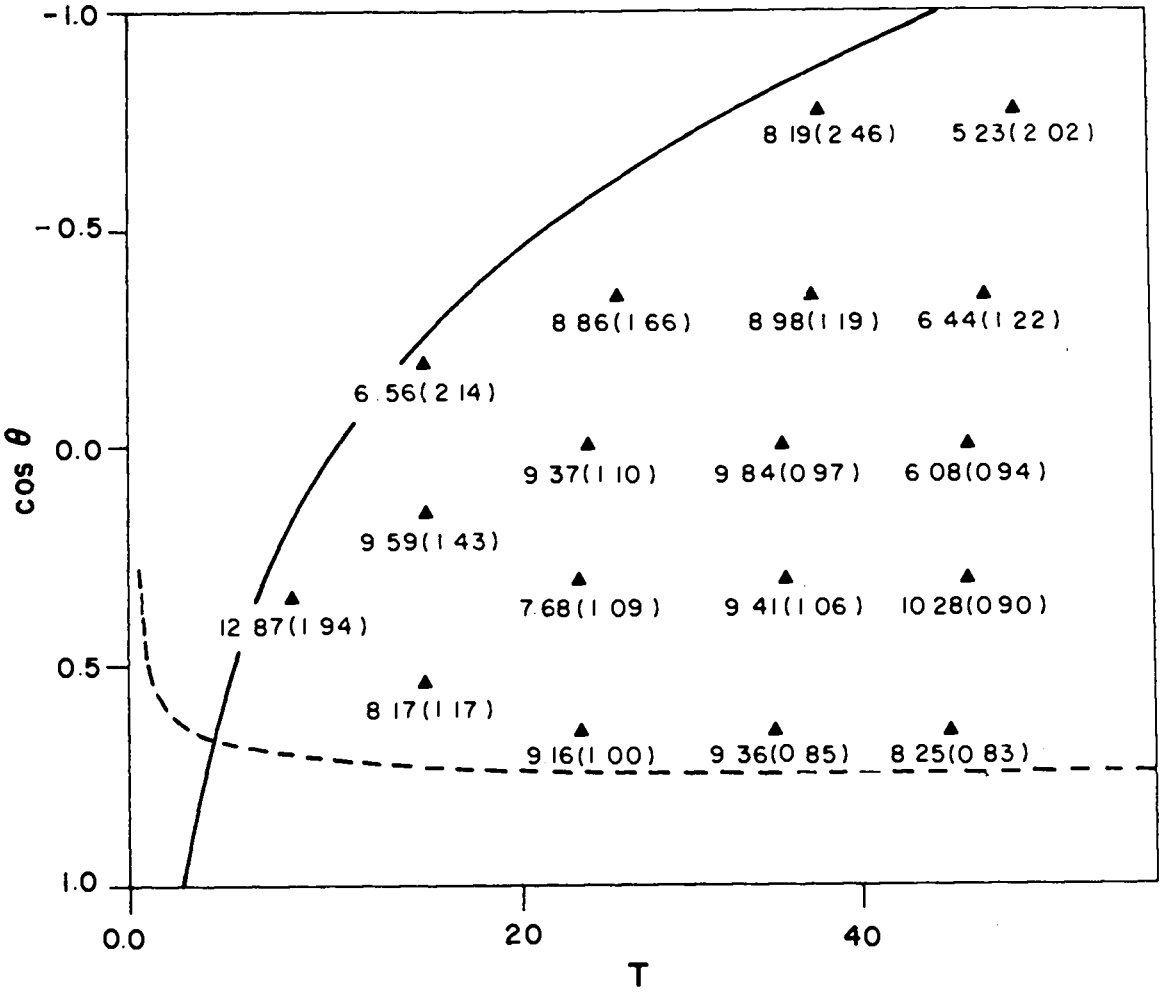

Fig. 31. Values of $\langle|M|^2\rangle$ at 254 MeV. The uncertainties are statistical.

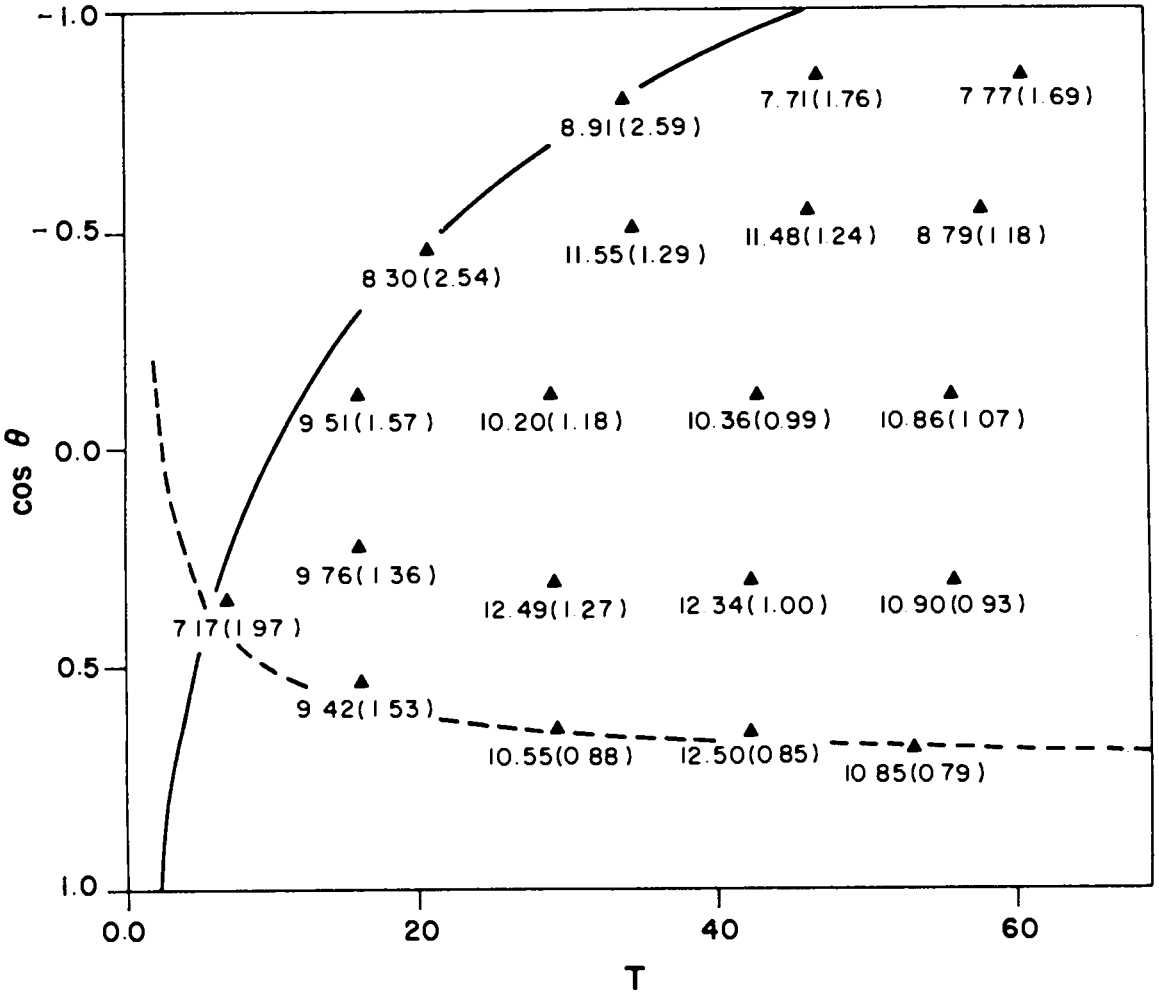

Fig. 32. Values of $\langle|M|^2\rangle$ at 279 MeV. The uncertainties are statistical.

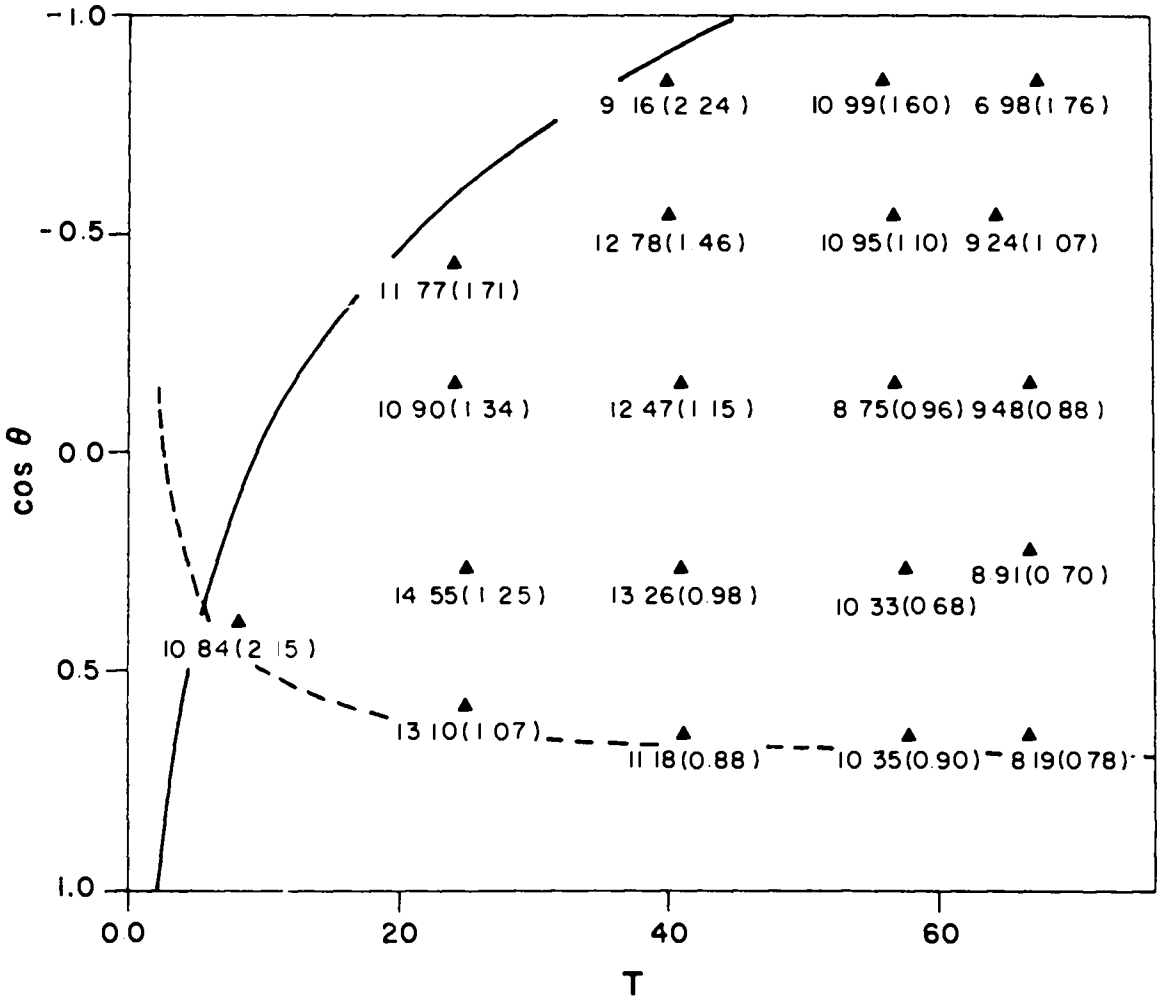

Fig. 33. Values of $\langle|M|^2\rangle$ at 292 MeV. The uncertainties are statistical.

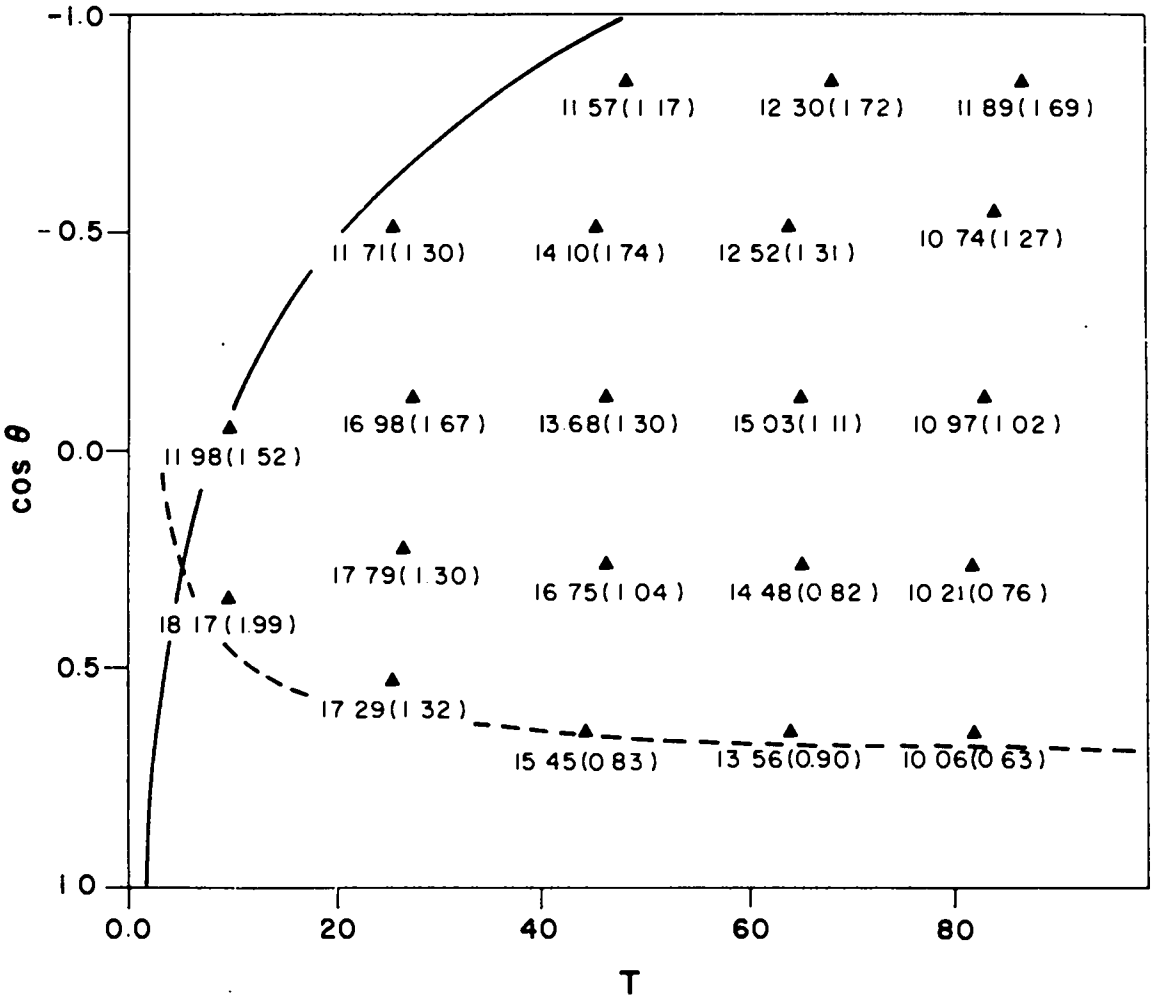

Fig. 34. Values of $\langle|M|^2\rangle$ at 330 MeV. The uncertainties are statistical.

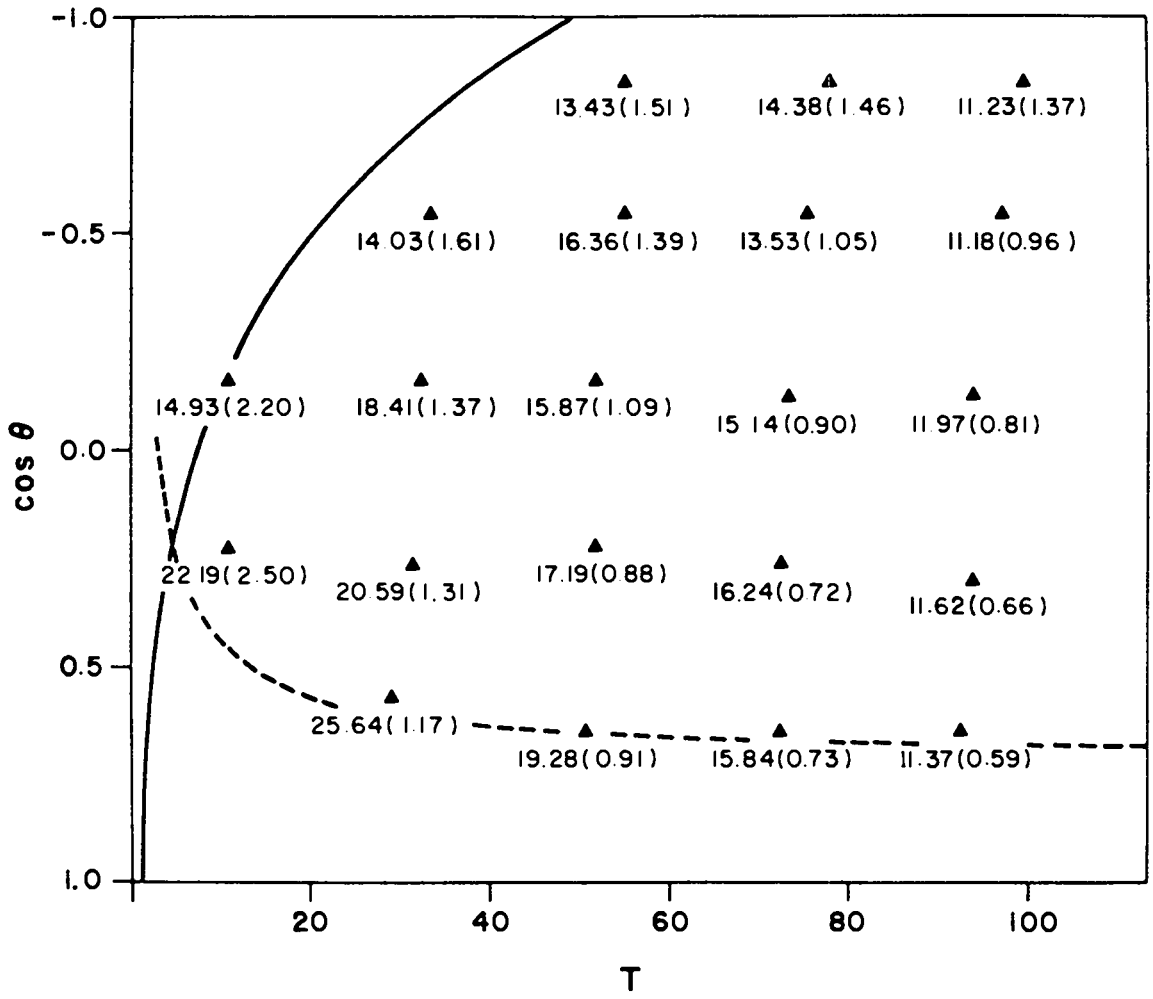

Fig. 35. Values of $\langle|M|^2\rangle$ at 356 MeV. The uncertainties are statistical.

$$\chi^2 = \sum_j \left(\langle |M|^2 \rangle_j - f(T_j, \cos\theta_j) \right)^2 \Delta_{Mj}^{-2}$$

using the algorithm described in Appendix A. Table XXVIII presents the resulting parameter values and the χ^2/ν obtained for the five energies. ζ_3 was required only for the two highest energies, and ζ_4 for the three highest.

The integrated cross sections were calculated as

$$\sigma_R = \int_0^{T_{max}} \int_{-1}^{1} \int_0^{2\pi} f(T,\cos\theta) \frac{d^2\sigma_0}{d\Omega dT} \, d\phi \, d\cos\theta \, dT \, ,$$

where the integrals over ϕ and $\cos\theta$ were carried out analytically while the integral over T was computed numerically. The statistical uncertainty in σ_R was calculated from the error matrix provided by the least squares algorithm. The uncertainty due to the uncertainty in ε was again taken to be the deviation produced by the substitution of $\varepsilon \pm \Delta\varepsilon$ for ε. These results are presented in Table XXIX and in Fig. 36 along with a selection of previous data.[24-30] The errors in the figure include in quadrature the statistical uncertainty, the sensitivity to ε, and a normalization uncertainty of 3% at the lowest three energies and 4% at the higher two. The integrated cross sections are in reasonable agreement with previous results.

The integrated cross section corrected to exclude Coulomb enhancement was also calculated,

$$\sigma_R' = \int_0^{T_{max}} \int_{-1}^{1} \int_0^{2\pi} C^{-1}(T) \, f(T,\cos\theta) \frac{d^2\sigma_0}{d\Omega dT} \, d\phi \, d\cos\theta \, dT \, .$$

The ratio $\overline{|M|^2} = \sigma_R'/\sigma_0$ represents the square modulus of the matrix element corrected for Coulomb enhancement and averaged over phase space. It is $\overline{|M|^2}$ which is to be extrapolated to the 172 MeV threshold, and

Table XXVIII. Parameter values for $\langle|M|^2\rangle$ at each energy. Uncertainties include only statistics.

T	ζ_1	ζ_2	ζ_3 $(GeV)^{-1}$	ζ_4 $(GeV)^{-2}$	χ^2/ν
254	2.85 ± 0.06	0.21 ± 0.13	-	-	1.43
279	3.18 ± 0.04	0.20 ± 0.09	-	-	1.02
292	3.63 ± 0.08	0.01 ± 0.08	-	-152. ± 25.	0.91
330	3.93 ± 0.07	-0.42 ± 0.16	14.7 ± 3.6	-92. ± 15.	1.28
356	4.39 ± 0.06	-0.43 ± 0.13	15.7 ± 2.8	-113. ± 10.	0.78

Table XXIX. Integrated cross sections for $\pi^- p \rightarrow \pi^+ \pi^- n$. Δ_1 is the statistical uncertainty, while Δ_2 is the overall uncertainty including allowances for normalization and Cerenkov efficiency uncertainties in quadrature. Units are MeV and μb/sr.

T	σ_R	Δ_1	Δ_2
254.3	173.2	6.6	11.1
279.3	380.3	10.5	17.1
292.0	535.9	17.2	24.5
330.8	1159.	27.	54.
355.9	1863.	37.	84.

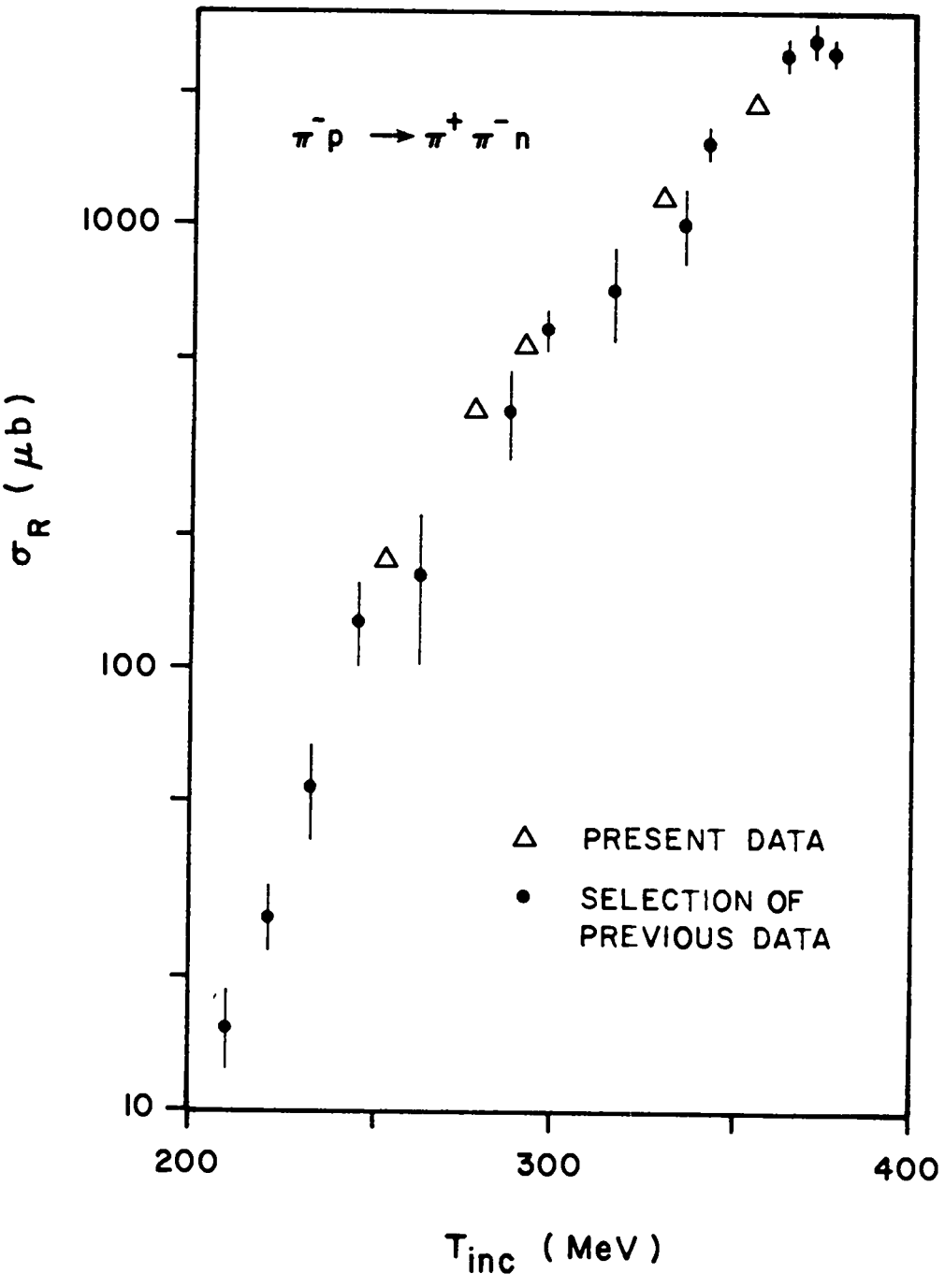

Fig. 36. Integrated cross sections for $\pi^- p \rightarrow \pi^+ \pi^- n$ from present experiment and a selection of previous measurements.[24-30]

its root compared to the soft pion result in Table I.

Comparison To Soft Pion Theory

$\overline{|M|^2}$ was extrapolated to threshold from the five values from this experiment and a more recent value at 230 MeV.[3] The $\overline{|M|^2}$ were fitted to

$$f(T_{tot}) = S_1 + S_2 T_{tot},$$

where T_{tot} is the total kinetic energy in the center of momentum frame and S_i are adjustable parameters. The points and curve are shown in Fig. 37. Fitting to higher order polynominals does not appear to be warranted. The results when ε was changed by $\pm\Delta\varepsilon$ are presented in Fig. 38, illustrating the sensitivity of the results to the efficiency for identifying the energetic positron background. The extrapolated thesh-old value of $\overline{|M|^2}$ is fairly insensitive to ε. This is due to the in-clusion of the value of $\overline{|M|^2}$ at the higher energies.

The results of the extrapolation to threshold and the comparison to soft pion theory are given in Table XXX. The symmetry breaking parameter ξ, obtained from the equation in Table I, is clearly sensitive to the choice of sign for the threshold matrix element. Consequently, the implied predictions for the threshold matrix element for $\pi^+p\to\pi^+\pi^+n$ and $\pi^-p\to\pi^0\pi^0n$ (See Table I) are similarly sensitive to the choice of sign. The meager supply of data in these two reactions strongly favors the first choice[2] in Table XXX, $M_{threshold} = -1.317$. ξ is also sensi-tive to f_π. The three values of f_π in the table correspond to the Goldberger-Treiman value and the extremes from the other soft pion calculations. These suggest the possible variation between f_π at the physical threshold and at the nonphysical soft pion limit. In any case

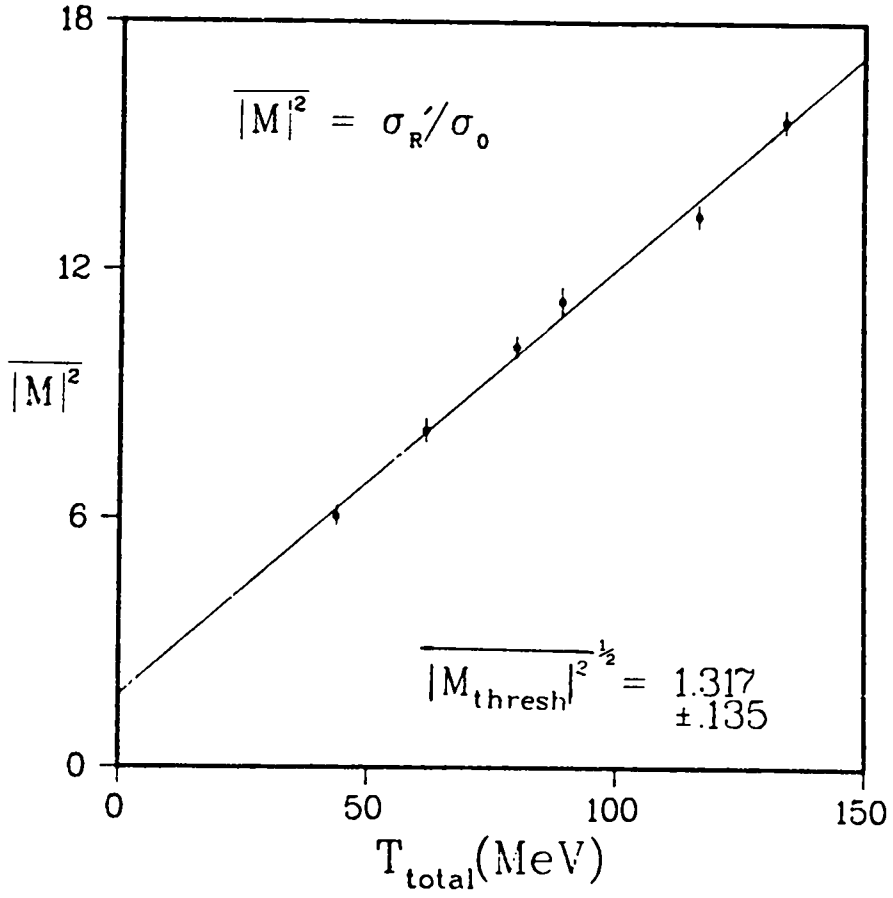

Fig. 37. Extrapolation of $|M|^2$ to threshold. The uncertainties are statistical.

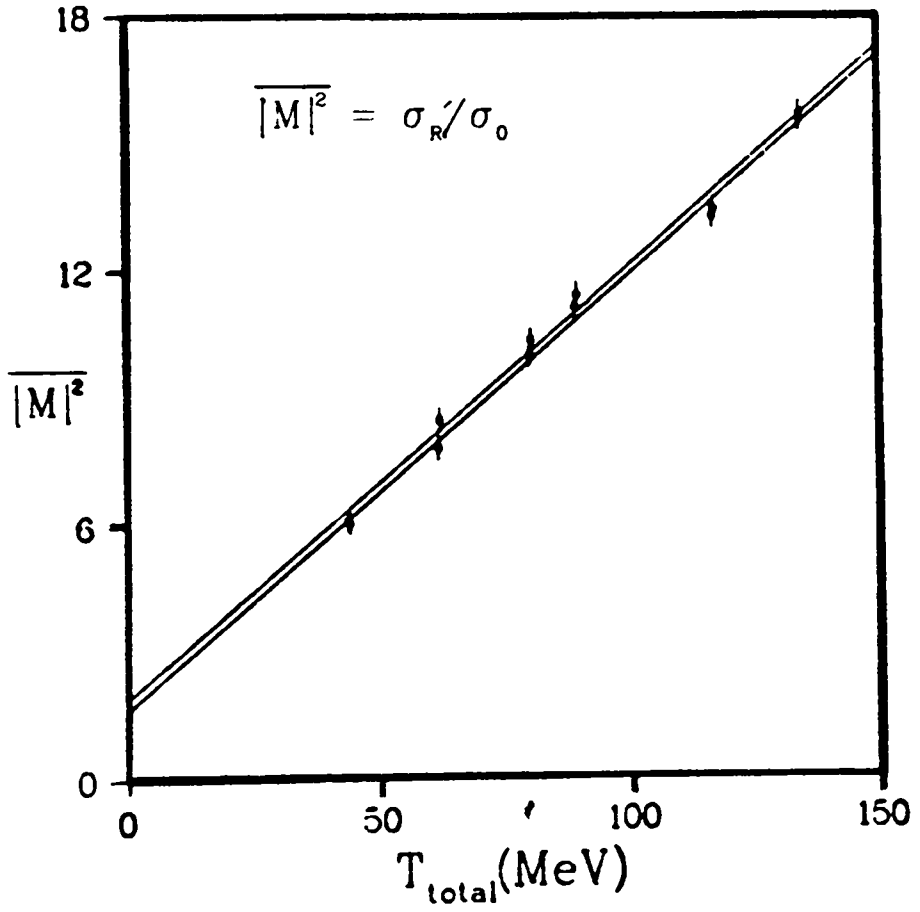

Fig. 38. Effect of the uncertainty in ε. The points and curve correspond to ε replaced by $\varepsilon \pm \Delta\varepsilon$.

Table XXX. Comparison to soft pion theory.

	M_{thresh}	f_π (MeV)	ξ	a_0 (m_π^{-1})	a_2 (m_π^{-1})
Value	-1.268	86.9	0.15	0.170	-0.055
Error	0.202		0.34	0.022	0.009
ε sensitivity	0.046		0.08	0.005	0.002
Value		81.8	0.39	0.175	-0.069
Error			0.30	0.022	0.009
ε sensitivity			0.08	0.005	0.002
Value		94.0	-0.21	0.165	-0.039
Error			0.39	0.022	0.009
ε sensitivity			0.10	0.005	0.002
Value	1.268	86.9	4.38	-0.101	-0.164
Error	0.202		0.34	0.022	0.009
ε sensitivity	0.046		0.08	0.005	0.002
Value		81.8	4.13	-0.097	-0.178
Error			0.30	0.022	0.009
ε sensitivity			0.08	0.005	0.002
Value		94.0	4.73	-0.106	-0.148
Error			0.39	0.022	0.009
ε sensitivity			0.10	0.005	0.002

ξ is consistent with zero. Presuming for the moment the validity of soft pion calculations, the π-π s-wave scattering lengths can be calculated and are presented in the table for each value of ξ. The determination of a_0 from K_{e4} decay ($K^+ \to \pi^+\pi^-e^+\nu_e$) is[31] $a_0 = 0.26 \pm 0.05\ m_\pi^{-1}$. This clearly favors the choice $M_{threshold} < 0$, but is somewhat larger than any of the results in the table. This is not a test of the soft pion calculation, since the K_{e4} measurement is difficult and its result is model dependent.

CHAPTER VI

SUMMARY AND CONCLUSIONS

We have presented a systematic study of the reaction $\pi^- p \to \pi^+ \pi^- n$ in the region near threshold. The doubly differential cross section $\frac{d^2\sigma}{d\Omega dT}$ for the produced π^+ was measured at about twenty points for each of five energies from 254 MeV to 356 MeV. The accuracy of the measurements ranged between 9% and 39% at 254 MeV and between 4.7% and 14.7% at 356 MeV. These are the first meaningful measurements of the doubly differential cross section in this energy range. At each energy the integrated cross section was derived from the measurements with an uncertainty of about 5%. As seen in Fig. 36, this represents a significant improvement. The mean square modulus of the matrix element was also determined at each energy. The value at the 172 MeV threshold was extrapolated from the set of these five values and a more recent value at 230 MeV.[3] Finally, the symmetry breaking parameter ξ of soft pion theory was determined.

The energy dependence of the mean square modulus evident from this work demonstrates the futility of extracting ξ from any single measurement of the cross section. Indeed, as can be seen in Fig. 37, only 1/3 of the cross section at 230 MeV arises from soft pion contributions. The hard pion contribution to the reaction evidently comprises 2/3 of the cross section. The determination of ξ favors the symmetry breaking mechanism proposed by Weinberg ($\xi=0$) over those suggested by Schwinger ($\xi=1$ and $\xi=2$).[2]

ACKNOWLEDGEMENTS

I would like to thank the Department of Physics and Astronomy, the University of Wyoming and the Los Alamos Scientific Laboratory for the facilities and services they have provided over the course of my graduate education. I would also like to thank the personnel and staff of the Clinton P. Anderson Meson Physics Facility for their hospitality during my residence in Los Alamos.

I wish to acknowledge the support of the Department of Energy, Division of High Energy and Nuclear Physics, under contract EY-76-5-02-2197. A002, which made this work and my stay in Los Alamos possible.

The advice, guidance and encouragement of Prof. Glen A. Rebka, Jr. has been invaluable.

Thanks are due Peter Gram, Charles Bordner, Alden Oyer, Mark Manley and Chris Bjork for valuable and interesting discussions. I thank Maggie Eutsler, Judy Powers, Alden Oyer and my wife, Mary Jean for their assistance in typing and preparing various drafts of this dissertation. The latter two are due special thanks as they provided help and encouragement which only the truest friends could have offered.

Finally, I dedicate this work to Daniel, my son, and Joseph, my father. To life.

APPENDIX A

NONLINEAR LEAST SQUARES FITTING ALGORITHM

The fitting algorithm minimizes the quantity

$$\chi^2 = \sum_i \sigma_i^{-2} \{ y_i - f(x_i,\vec{\zeta}) \}^2$$

where (x_i,y_i) is the i^{th} data point, σ_i is the uncertainty in y_i and $\vec{\zeta}$ represents the collection of adjustable parameters. The function f can be any function which exists and has a derivative with respect to each of the ζ_i at each of the data points, and is in general nonlinear in the parameters ζ. Based upon the Gauss or Taylor series method, the algorithm seeks a root to

$$\nabla_\zeta \chi^2 = 0,$$

where ∇_ζ is the gradient with respect to the parameters. The method makes the linearizing assumption

$$\nabla_\zeta \chi^2 = \overline{\overline{A}}_{\vec{\zeta}} \quad (\vec{\zeta}-\vec{\zeta}^*),$$

where $\vec{\zeta}^*$ is the collection of the optimum parameter values and

$$\overline{\overline{A}}_{\vec{\zeta}} = 2 \sum_i \{ \nabla_\zeta f(x_i,\vec{\zeta}) \} \sigma_i^{-2} \{ \nabla_\zeta f(x_i,\vec{\zeta}) \}.$$

This expression for $\nabla_\zeta \chi^2$ would be the first term of the Taylor expansion about $\vec{\zeta}^*$ if the gradients in $\overline{\overline{A}}$ could be evaluated at $\vec{\zeta}^*$. Not knowing $\vec{\zeta}^*$, the above expression for $\nabla_\zeta \chi^2$ is used.

The solution is then sought in an iterative fashion. An initial guess $\vec{\zeta}$ is made for $\vec{\zeta}^*$, $\nabla\chi^2$ and $\overline{\overline{A}}$ are calculated for this $\vec{\zeta}$, and the set of equations relating $\nabla\chi^2$ to $\overline{\overline{A}}$ are solved to obtain a new guess for $\vec{\zeta}^*$. This procedure is repeated until the resultant change in each of

the parameters is less than some standard, in our case one part in 10^8. This method can be used to find the roots of any nonlinear equation and is always plagued with the same difficulties. In particular if the initial guess is too far from the desired solution, the algorithm may converge to an undesired root which may actually correspond to a relative maximum in χ^2, or it may fail to converge entirely. For the applications in this work, the method converged in fifteen iterations or less when the initial guess was reasonable. Erroneous solutions were obvious.

The algorithm also provides an error matrix. The matrix A is the inverse of the error matrix when $f(x,\vec{\zeta})$ is linear in each of the ζ_i and the y_i possess Gaussian statistics. That is, if the parameter ζ_j is displaced from ζ_j^* by $\pm\{(A^{-1})_{jj}\}^{\frac{1}{2}}$ and the remaining ζ_i are varied to minimize χ^2 under that constraint, the resulting minimum value will be larger than the unconstrained minimum by 1. For a nonlinear function $f(x,\vec{\zeta})$, the error matrix provided by the algorithm is the linear approximation.

APPENDIX B

MOMENTUM CORRECTIONS

Several corrections were included in the determination of the momentum distribution of the pions in each of the incident beams. Two corrections were made to the centroid of the distribution and four corrections to the width of the distribution.

The first correction p_{loss} to the momentum of the scattered pions accounted for loss of energy to atomic electrons

$$-p_{loss} = \frac{d\,p_{out}}{d\,p_{in}} \frac{d\,p_{in}}{d\,x} \overline{S_{in}} + \frac{d\,p_{out}}{d\,x} \overline{S_{out}} \,.$$

Here p_{in} is the incident momentum, p_{out} is the scattered momentum calculated from two body kinematics, and $\overline{S_{in}}$ and $\overline{S_{out}}$ are the mean path lengths entering and leaving the target. The momentum loss $\frac{dp}{dx}$ was based upon the Bethe-Block formula

$$-\frac{1}{\rho}\frac{dE}{dx} = \frac{2\pi n e^4}{\rho\, m_e \beta} \left\{ \ln\left(\frac{2\, m_e\, \beta^2\, W_{max}}{I^2\,(1-\beta^2)}\right) - 2\beta^2 - \delta - U \right\}$$

where E and β are the energy and velocity of the particle, ρ is the density of the material, n is the number density of the electrons in the material, e and m_e are the charge and mass of the electron, and W_{max} is the maximum energy which can be transferred to an electron in a single collision. The ionization potential I of hydrogen is 18.30 eV.[32] The density correction δ was calculated according to the formulae of Sternheimer.[33] The shell correction U was negligible, being important only when $\beta < \beta_e$ with β_e the velocity of the atomic electron.

The second correction p_{ang} to the momentum of the scattered pions allowed for the finite angular acceptance of the spectrometer and the finite emittance of the pion channel. The mean cosine of the scattering angle differed from the cosine of the mean scattering angle, for which p_{out} was calculated. Thus p_{out} was corrected by

$$p_{ang} = (\overline{\cos\theta} - \cos\theta_0) \frac{d\, p_{out}}{d \cos\theta} ,$$

where all quantities are in the laboratory frame.

Of the four corrections to the width of the scattered distribution, two were for variation in loss of energy and two for variation in scattering angle. The dominant correction for variation in loss of energy was from variation in path lengths in the target, and was given by

$$\sigma^2_{loss} = (\overline{S^2_{in}} - \overline{S_{in}}^2) \left(\frac{d\, p_{out}}{d\, p_{in}}\right)^2 \left(\frac{d\, p_{in}}{d\, x}\right)^2 + (\overline{S^2_{out}} - \overline{S_{out}}^2) \left(\frac{d\, p_{out}}{d\, x}\right)^2$$
$$+ 2(\overline{S_{in}\, S_{out}} - \overline{S_{in}}\ \overline{S_{out}}) \left(\frac{d\, p_{out}}{d\, x}\right) \left(\frac{d\, p_{out}}{d\, p_{in}}\right) \left(\frac{d\, p_{in}}{d\, x}\right) .$$

The random nature of the collisions also provided a variation to the energy lost to atomic electrons. The mean square contribution was

$$\sigma^2_{strag} = \overline{S_{out}}\ \frac{d}{dx} \overline{(p-\bar{p})^2} = \overline{S_{out}}\ \frac{2\pi\, e^4\, n\, (1+\gamma^2)}{1 + 2\gamma(m_e/m_\pi) + (m_e/m_\pi)^2}$$

where n is the number density of the electrons. The dominant correction for variation in angle was due to the geometry of the system, and was given by

$$\sigma^2_{ang} = (\overline{\cos^2\theta} - \overline{\cos\theta}^2) \left(\frac{d\, p_{out}}{d\, x}\right)^2 .$$

A correction for small angle scattering was also included. Its mean

square contribution was

$$\sigma^2_{coul} = \frac{\overline{S_{out}}\, E_s^2}{\chi_0\, p_{out}^2\, \beta^2} \left(\frac{d\, p_{out}}{d\, \theta}\right)^2$$

where χ_0 is the radiation length in liquid hydrogen, and $E_s = m_e\left(\frac{4\pi}{\alpha}\right)^{\frac{1}{2}}$.

APPENDIX C

e^+ VETO EFFICIENCY

The background for the investigated reaction $\pi^-p\rightarrow\pi^+\pi^-n$ included a spectrum of e^+. This background resulted from the sequence of single charge exchange in the target wall and hydrogen, π^0 decay, and pair production in the spectrometer with the e^+ transported to the surface barrier detectors. The ability to eliminate these events was crucial since they were largely associated with the liquid hydrogen, and hence not corrected by the subtraction of the target empty rate. These e^+ events were principally identified with the threshold Cerenkov detector described in Chapter II. This Appendix deals with the efficiency of that device.

The efficiency was found to be substantially less than 1.0 when the integrated cross section was remeasured at the lowest energy. Assuming an efficiency of 1.0, the present experiment determined $\sigma_R = 93 \pm 6$ μb at 229 MeV, while the remeasurement[3] yielded $\sigma_R = 60 \pm 3$ μb at 230 MeV. A careful reexamination of both experiments left no doubt that the electron efficiency of the Cerenkov detector in this experiment was at fault. The spectra of energetic pions and electrons detected by the Cerenkov detector of the remeasurement (which also used FC-88 as the medium, but provided more uniform trajectories) and the fraction of energetic pions detected by the Cerenkov detector in this experiment (available from the elastic scattering data) suggested an efficiency no greater than 88%.

The efficiency was determined from the π^+ production data taken at 229 MeV in this experiment and the remeasurement at 230 MeV in an iterative fashion. A guess was made for ε, the efficiency, and $\overline{|M|^2}$ was calculated from the data at 229 MeV, where $\overline{|M|^2}$ is the mean square modulus of the matrix element corrected for Coulomb enhancement. This value was required to agree with $\overline{|M_0|^2}$, the value of $\overline{|M|^2}$ determined from the remeasurement at 230 MeV. Values were tried for ε until this requirement was met to within one part in 600. Forming a χ^2

$$\chi^2 = \frac{\left(\overline{|M_0|^2} - \overline{|M(\varepsilon)|^2} \right)^2}{\Delta^2_{M_0} + \Delta^2_M}$$

where Δ_{M_0} is the statistical uncertainty in $\overline{|M_0|^2}$ and Δ_M is the statistical uncertainty in $\overline{|M(\varepsilon)|^2}$ for the optimum value of ε. The uncertainty in ε was taken to be the variation in ε which produced $\chi^2=1$. The resultant Cerenkov efficiency for electrons was $\varepsilon = 0.828 \pm 0.038$.

The above efficiency applied for nearly all of the data, but not for the bulk of the data at 292 MeV. This data was chronologically first, and for the most part was taken with the S_3 trigger scintillator near S_1 and S_2 instead of near the Cerenkov detector. The threshold level on the Cerenkov detector was also different in the early configuration. The electron efficiency of the Cerenkov detector ε_e for the early data was thus different from the efficiency for the rest of the data. Four of the data points at 292 MeV were measured with both trigger configurations and hence both efficiencies. These points provided a basis for determining ε_e. A χ^2 was defined

$$\chi^2 = \sum_{i=1}^{4} \frac{\{ \langle |M|^2 \rangle_i - \langle |M|^2 \rangle_{ei} \}^2}{\Delta^2_{Mi} + \Delta^2_{Mei}}$$

with the subscript e denoting the results from the early configuration. The $\langle|M|^2\rangle_i$ were calculated for the value of ε determined above, and χ^2 was calculated for seven values of ε_e near the optimum value. The values of χ^2 were well fitted by a parabola as a function of $x=(1-\varepsilon_e)/\varepsilon_e$. The optimum ε_e was associated with the minimum of the parabola, while its uncertainty was identified with the variation in ε_e which increased χ^2 by 1.0 over its minimum value. The resulting value was $\varepsilon_e = 0.653 \pm 0.28$.

REFERENCES

1. M. G. Olsson and Leaf Turner, Phys. Rev. 181, 2141 (1969). F or g_V/g_a = 1.253 the Goldberger-Treiman relation gives f_π = 86.9 MeV. Various determinations of the πN s-wave scattering lengths (see M. M. Nagels et al., Nucl. Phys. B147, 189 (1979)) give results between 82 MeV and 92 MeV.

2. Leaf Turner, Ph.D. dissertation, University of Wisconsin, 1969 (unpublished).

3. C. W. Bjork, S. E. Jones, T. R. King, D. M. Manley, A. T. Oyer, G. A. Rebka, Jr., J. B. Walter, R. Carawon, P. A. M. Gram, F. T. Shively, C. A. Bordner and E. L. Lomon, to be published.

4. P^3 User Group and P. A. M. Gram, "A Proposal for P^3, A Versatile High-Energy Pion Beam Facility", LASL Report # LA-4535-MS, 1970; H. H. Howard, B. Storms and S. P. Slatkin, LAMPF Users Handbook, (Los Alamos Scientific Laboratory, Medium Energy Physics Division, Los Alamos, NM, 1974).

5. The necessary magnetic fields were determined in a TRANSPORT simulation and converted to shunt voltages by SHUNT. K. L. Brown, "A First and Second Order Matrix Theory for the Design of Beam Transport Systems and Charged Particle Spectrometers," SLAC-75 (1967); R. Macek, private communication, 1973.

6. G. J. Krausse and P. A. M. Gram, Nucl. Instr. and Meth. 156, 365 (1978).

7. The target flask was positioned with the aid of a surveyor's transit. The precision obtained was about 0.5 mm after the target was subsequently cooled down to liquid hydrogen temperatures.

8. A. T. Oyer, Ph.D. dissertation, University of Wyoming, 1976. Published as LASL Report #LA-6599-T.

9. B. Grennberg and A. Rytz, Metrologia 7, 65 (1971); CRC Handbook of Chemistry and Physics, 59th ed. (CRC Press, Inc., West Palm Beach, Florida, 1979), p. B-353.

10. J. B. Walter and G. A. Rebka, Jr., "SCATPI, A Subroutine for Calculating πN Cross Sections and Polarizations for Incident Pion Kinetic Energies Between 90 and 300 MeV", LASL Report #LA-7731-MS, 1979.

11. J. R. Carter, D. V. Bugg and A. A. Carter, Nucl. Phys. B58, 378 (1973).

12. P. J. Bussey, J. R. Carter, D. R. Dance, D. V. Bugg, A. A. Carter and A. M. Smith, Nucl. Phys. B58, 363 (1973).

13. A. A. Carter, J. R. Williams, D. V. Bugg, P. J. Bussey and D. R. Dance, Nucl. Phys. B26, 445 (1971).

14. D. V. Bugg, P. J. Bussey, D. R. Dance, A. R. Smith, A. A. Carter and J. R. Williams, Nucl. Phys. B26, 588 (1971).

15. E. H. Rogers, O. Chamberlain, J. H. Foote, H. M. Steiner, C. Wiegand and T. Ypsilantis, Rev. Mod. Phys. 33, 356 (1961).

16. J. H. Foote, O. Chamberlain, E. H. Rogers, H. M. Steiner, C. Wiegand and T. Ypsilantis, Phys. Rev. 122, 948 (1961).

17. L. D. Roper, R. M. Wright and B. T. Feld, Phys. Rev. 138, B190 (1964).

18. P. R. Auvil, Phys. Rev. 168, 1568 (1968); D4, 240 (1971).

19. J. R. Taylor, Scattering Theory (Wiley & Sons, New York, 1972), p. 213-231.

20. J. D. Jackson, Nuovo Cimento 34, 1644 (1964).

21. V. Chaloupka et al., Phys. Lett. 50B, 10 (1974).

22. P. M. Ogden, D. E. Hagge, J. A. Helland, M. Banner, J. F. Detoeaf and J. Teiger, Phys. Rev. 137, B1115 (1965)

23. H. R. Rugge and O. T. Vik, Phys. Rev. 129, 2300 (1963).

24. B. C. Barish, R. J. Kurz, V. Perez-Mendez and J. Solomon, Phys. Rev. 135, B416 (1964).

25. Yu A. Batusov et al., Sov. J. Nucl. Phys. 1, 374 (1965).

26. T. Blokhintseva et al., Proc. of the 12th Annual International Conference on High Energy Physics, Dubna (1964).

27. J. A. Jones, W. W. M. Allison and D. H. Saxon, Nucl. Phys. B83, 93 (1974).

28. J. Kirz, J. Schwartz and R. D. Tripp, Phys. Rev. 130, 2481 (1963).

29. W. A. Perkins, III et al., Phys. Rev. 118, 1364 (1960).

30. D. H. Saxon, H. H. Mulvey and W. Chinowsky, Phys. Rev. D2, 1790 (1970).

31. W. Ochs, AIP Conf. Proc. #41, p. 326 (1978).

32. J. Jani, Air Force Weapons Laboratory TR-65-150.

33. R. M. Sternheimer, Phys. Rev. 103, 511 (1956).

☆ U.S. Government Printing Office: 1980 — 677 — 115/88

Printed in the United States of America. Available from
National Technical Information Service
US Department of Commerce
5285 Port Royal Road
Springfield, VA 22161

Microfiche $3.00

001-025	4.00	126-150	7.25	251-275	10.75	376-400	13.00	501-525	15.25
026-050	4.50	151-175	8.00	276-300	11.00	401-425	13.25	526-550	15.50
051-075	5.25	176-200	9.00	301-325	11.75	426-450	14.00	551-575	16.25
076-100	6.00	201-225	9.25	326-350	12.00	451-475	14.50	576-600	16.50
101-125	6.50	226-250	9.50	351-375	12.50	476-500	15.00	601-up	

Note: Add $2.50 for each additional 100-page increment from 601 pages up.